Simulation of pressure drop and coke deposition in the grid of a scrubber

by

Nirmalkumar Subudhi

B.E., R.E.C, Rourkela, India, 1996

A THESIS SUBMITTED IN PARTIAL FULFILLMENT
OF THE REQUIREMENTS FOR THE DEGREE OF
MASTER OF APPLIED SCIENCE

in

THE FACULTY OF GRADUATE STUDIES
(Chemical and Biological Engineering)

THE UNIVERSITY OF BRITISH COLUMBIA
April 2006

Abstract

Hot vapours from bitumen coking are contacted with bitumen fractions and gas oils in scrubber systems in order to cool the vapour and remove the heavy components. In fluid coking, the scrubber contains a grid of layers of structured packing as well as a section of sheds. The pressure drop in the scrubber grid increases over time due to the formation of coke on the grid surface. This build up eventually results in the shutdown of the fluid coker. The objective of this study is to understand the pressure drop change in the scrubber grid due to the formation of coke. HYSYS was used to calculate physical and thermodynamic properties in the system and to model the contact and separator processes. The Bravo-Rocha-Fair (BRF) model was used to calculate pressure drop for Koch-Glitsch Flexigrid #2 packing in counter-current flow. Liquid droplets of high molecular mass species from the coker are present in the vapour which enters the grid. Transport and attachment models for the droplets are used to calculate the total mass of droplets which stick to the surface per unit time. The +524°C heavy components in the droplets are assumed to undergo reactions to form volatiles and toluene insolubles (coke). The mass of carbonaceous solids formed per unit time is calculated using the available coking kinetics. As the coke layer grows, the voidage in the packing decreases, and the pressure drop increases. Therefore the pressure drop build-up calculation involves using HYSYS to calculate the contribution of droplets in the vapour and all fluid properties, the BRF model to calculate pressure drop in counter-current multiphase flow, a mass transfer model to evaluate transport of fine droplets to both dry and wetted portions of the grid, an attachment model to determine the quantity of droplets which adhere to the surface, and a coking kinetics model to calculate the solids build-up. The attachment coefficient was set for a base case to give an increase in pressure drop of 1" H_2O over a one year operating time. Two extreme cases were considered – a highly temperature sensitive (high activation energy) adhesion process, and a nearly temperature independent (low activation energy) adhesion process. Calculations were undertaken to illustrate the roles of wetting of the packing, droplet size, and wash oils flow and temperature on the deposit build-up with time. This model can, in principle, be extended to other scrubbers for multi-component hydrocarbon mixtures.

Table of Contents

List of Tables

List of Figures

Abbreviations

ASTM D1160	Standard Test Method for Distillation of Petroleum Products at Reduced Pressure
ASTM D2887	Standard Test Method for Boiling Range Distribution of Petroleum Fractions by Gas Chromatography
ASTM D86	Standard Test Method for Distillation of Petroleum Products at Atmospheric Pressure
ATB	Atmospheric Topped Bitumen
BRF	Bravo-Rocha-Fair pressure drop model
DRU	Diluent Recovery Unit
EOR	End of Run of the plant
GPDC	Generalized Pressure Drop Correlation
HGO	Heavy Gas Oil
LGO	Light Gas Oil
MCR	Micro Carbon Residue
SBF	Stichlmair-Bravo-Fair pressure drop model
SOR	Start of Run of the plant
TBP	True Boiling Point
VDU	Vacuum Distillation Unit
VTB	Vacuum Tower Bottom

Nomenclature :

a_p	Specific surface area of the packing, m^2/m^3
c	Concentration of the droplet, kg/m^3
C, C_1, C_2, C_3, C_4, C_5, C_6, α,	Constants for the structured packing
c_p	Specific heat capacity, $kJ/kg\ °C$
C_S	C-factor
D	Molecular diffusivity or Brownian diffusivity of droplets in suspension, m^2/s
d_d	Diameter of the droplet, m
d_{eq}	Packing equivalent diameter under clean condition, m, $d_{eq} = \frac{6(1-\varepsilon)}{a_p}$ for particle model and $d_{eq} = \frac{4\varepsilon}{a_p}$ for cylindrical model
E	Activation energy for attachment of the droplet in Eq.(2.43), *kcal/mol*
E_R	Activation energy for TI formation in Eq.(2.45), *kcal/mol*
f	Fanning friction factor for the vapour in the grid, $f = C_4 + \frac{C_5}{\mathrm{Re}_g}$
F_{lv}	Flow parameter, $F_{lv} = \frac{L}{G}\left(\frac{\rho_g}{\rho_l}\right)^{0.5}$
F_p	Packing factor of the packing
Fr_l	Froude number of the liquid, $Fr_l = u_l^2 \frac{a_p}{g\,\varepsilon^{4.65}}$ for particle model and $Fr_l = \frac{u_l^2}{d_{eq}\,g}$ for cylindrical model
F_s	Gas factor, $m/s\ (kg/m^3)^{0.5}$
G	Mass flowrate of gas, kg/s
g	Acceleration due to gravity = 9.81 m^2/s
h	Hold up in the grid

k''	Constant that includes Arrhenius pre exponential factor and residence time proportionality factor in Eq.(2.43), s^2/m
K	Equilibrium constant between the concentrations of droplet at the vapour-liquid interface.
k_a	Attachment coefficient of the droplet on the surface of the packing, *m/s*
k_B	Boltzmann constant = 1.38 x 10^{-23} *J/K*
k_d	Deposition coefficient, *m/s*
k_m	Mass coefficient of the droplet in the fluid, *m/s*
k_t	Transport coefficient of the droplet in the fluid, *m/s*
k_t^+	Non dimensionalized transport coefficient
k_w	Transport coefficient of droplet in fluid in liquid film on the surface, *m/s*
L	Mass flowrate of liquid, *kg/s*
m	Mass , *kg*
MCR	Micro carbon residue *(gm/gm of +524°C)*
$N_{Re,film}$	Reynolds Number of liquid film flowing along the flat plate, $N_{Re,film} = 4\Gamma/\mu_l$
$N_{Re,x}$	Reynolds number for vapour over flat plate of distance x, $N_{Re,x} = x\, u_{ge}\, \rho_g / \mu_g$
N_{Sc}	Schmidt Number for fluid over flat plate of distance x, $N_{Sc} = \mu / (\rho D)$
$N_{Sh,avg}$	Average Sherwood Number, $N_{Sh,avg} = k_m\, x / D$
R	Gas constant = 8.31447 kJ/mol K
Re_g	Reynolds Number of vapour in the grid, $\mathrm{Re}_g = \dfrac{u_g d_{eq} \rho_g}{\mu_g}$
T	Temperature, K
t	Heating time, min
t_d^+	Non-dimensionalized relaxation time for droplet, $t_d^+ = \rho_d\, d_d^2\, u^{*2} / (18\, \mu v)$
TI	Yield of toluene insoluble (coke), *gm TI / gm of +524°C*
TI_o	Initial toluene insoluble (coke) in pitch (+524°C). This may contain ash, metal traces etc. *gm / gm of +524°C*
u	Superficial velocity of the fluid in the grid, *m/s*
u^*	Friction velocity, *m/s*
V	Yield of volatiles, *gm V / gm of +524°C*

w	Width of the flat plate, m
x	Length of the flat plate, m

Greek symbols

μ	Dynamic viscosity of the fluid, $kg/m\ s$
ε	Voidage of the packing when there is no fouling deposit on the packing surface
ΔP	Pressure drop for irrigated packing with fouling deposit per unit height, $N/m^2\ m$
ΔP_{dry}	Pressure drop for dry packing per unit height, $N/m^2\ m$
ρ	Density of fluid, kg/m^3
ϕ_d	Mass deposition flux for droplets, $kg/m^2\ s$
τ_w	Wall shear stress for fluid flowing over flat plate, $kg/\ m\ s^2$
β	Angle of the inclination of the flat plate with respect to vertical, deg
Γ	Liquid loading over a flat plate, $kg\ /\ m\ s,\ \Gamma = \frac{L}{w}$
δ	Liquid film thickness on the inclined plate, $\delta = \left(\frac{3\Gamma \mu_l}{\rho_l^2\ g \cos\beta} \right)^{1/3}, m$
ν	Kinematic viscosity of the fluid, m^2/s
ς_0	Friction factor of a single particle under the clean condition of the grid, this is used in SBF pressure drop model

Subscripts

b	Bulk stream
c	Coke
d	Droplet
eq	Equivalent
f	Foulant
g	Gas
ge	Effective gas

i	Interface between gas/liquid
irr	Under irrigated and fouled condition
l	Liquid
s	Surface
T	Total
w	Wall

Acknowledgement

I would like to take this opportunity to express my profound gratitude to my supervisors, Dr. A. P. Watkinson and Dr. D. Posarac for their immense contributions, support and guidance throughout my masters' program.

Special thanks to Dr. Craig. A. McKnight, Syncrude Canada Ltd., for his assistance and valuable suggestions.

I would like to dedicate this thesis to my family and my close friends, for their great support and encouragement through out my difficult times.

Chapter 1: Introduction

The oil reserves in the oil sands of Northern Alberta are 174 billion barrels, which in world terms is second only to those of Saudi Arabia. Alberta's oil sands industry is the result of multi-billion-dollar investments in infrastructure and technology required to develop the non-conventional resource. In the last five years alone, industry has allocated $24.7 billion towards oil sands development. Annual oil sands production is growing steadily as the industry matures. Output of marketable oil sands production increased to 858,000 barrels per day (bbl/d) in 2003, up from 741,000 bbl/d the year before. It is anticipated that in 2005, Alberta's oil sands production may account for one-half of Canada's total crude output and 10 percent of North American production (Reynolds, 2005).

Development of Alberta's oil sands resources represents a triumph of technological innovation. Over the years, government and industry have worked together to find innovative and economic ways to extract and process the oil sands. Syncrude Canada Ltd., Suncor Inc. and Shell Canada Ltd. are major producers of synthetic crude oil from oil sands.

Oil sands deposits contain sand, bitumen, mineral-rich clays and water. The bitumen in the oil sand mined at the Athabasca site averages around 10.5 percent by weight and is made up of 50 to 60 percent oil, 30 to 35 percent resins and 15 to 25 percent asphaltenes. In its raw state, bitumen is a black asphalt-like oil – as thick as molasses. It requires upgrading to make it transportable by pipeline and useable by conventional refiners. The upgraded bitumen product is called synthetic crude oil, (Reynolds, 2005).

1.1 Production of synthetic crude from oil sands

There are numerous ways to recover oil from oil sands. A large amount of current production occurs by the process described below, Fig.1.1. The oil sands are mined and transported from the mining site to the crushing station as a huge chunks, which are then broken down to about 45 cm diameter and to 5 cm diameter by fine grinding. The oil sand enters tumblers (large horizontal rotating drums), where the oil sand is slurried by steam, hot water and caustic soda to condition it for bitumen separation. The oversize materials such as rocks, lumps of clays, and undigested oil

sand are rejected. The remaining slurry is diluted and pumped into primary separation vessels. In the primary separation vessels, bitumen floats to the surface as primary froth and is separated from water, and sand is removed from the bottom of the separation process.

During the upgrading process, bitumen is converted from a black viscous, tar-like oil to synthetic crude oil, which is low in sulphur. Upgrading consists of two areas: primary and secondary. In primary upgrading, the bitumen from the extraction process is fed into a Diluent Recovery Unit (DRU). This is an atmospheric distillation column and serves three purposes: it boils off diluent naphtha and returns it to the extraction process; it recovers Light Gas Oil (LGO) and sends it directly to the hydro-treater; and it produces hot bitumen known as Atmospheric Topped Bitumen (ATB) as feedstock for the fluid cokers and the LC-Finer. A part of this ATB feedstock is also fed to the Vacuum Distillation Unit (VDU).

The VDU removes light and heavy gas oil and produces Vacuum Tower Bottom (VTB) at the bottom. The light and heavy gas oil are then sent to the hydro-treater and the residual VTB is blended with the hot bitumen coming from DRU and is then sent to the LC-Finer and fluid coker for further processing. LC Fining is a catalytic process in which hydrogen is added to increase the low hydrogen-to-carbon ratio of bitumen to produce cracked LGO. The unreacted residue from the LC Finer is sent to a fluid coker for further cracking. ATB, VTB and LC-Finer residue are fed to the fluid coker.

In the fluid coker, a coking process takes place in which heavy hydrocarbons in bitumen are broken down to produce volatiles and solid coke. The volatiles from the fluid coker (scrubber overhead) and LC-Finer are combined together to become the feed to a fractionator (not shown). Naphtha, LGO and Heavy Gas Oil (HGO) are produced from the fractionator. These three streams go to secondary upgrading in the hydro-treater. The feed from primary upgrading to secondary upgrading is high in sulphur, nitrogen, metals and unsaturates. These three streams react with hydrogen in the hydro-treater at high pressure and temperature in the presence of a catalyst. The hydro-treater removes sulphur and nitrogen and stabilizes the oil streams which form synthetic crude oil. The sulphur is converted to elemental sulphur. Nitrogen is removed as ammonia and burned in the CO boiler in the Utilities plant. Fuel gas produced in hydro-treating is sent to amine units for hydrogen sulphide removal. The resulting sweet gas is used in the plant.

The product streams of naphtha and gas oils from the hydro-treaters are blended to make a high grade synthetic crude oil. This is then pipelined to refineries for production of gasoline and diesel.

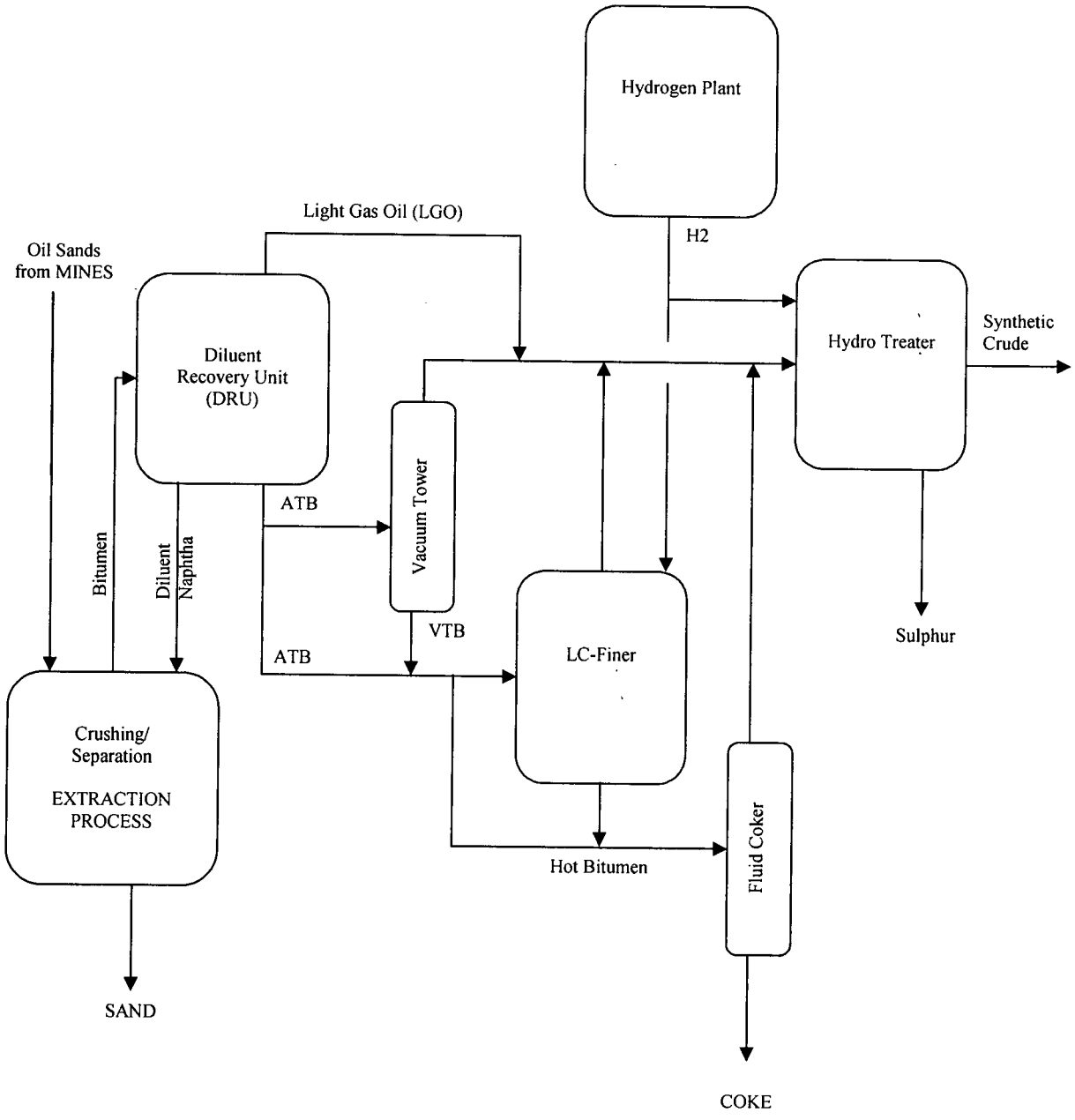

Figure 1.1 Description of Oil Sands Process

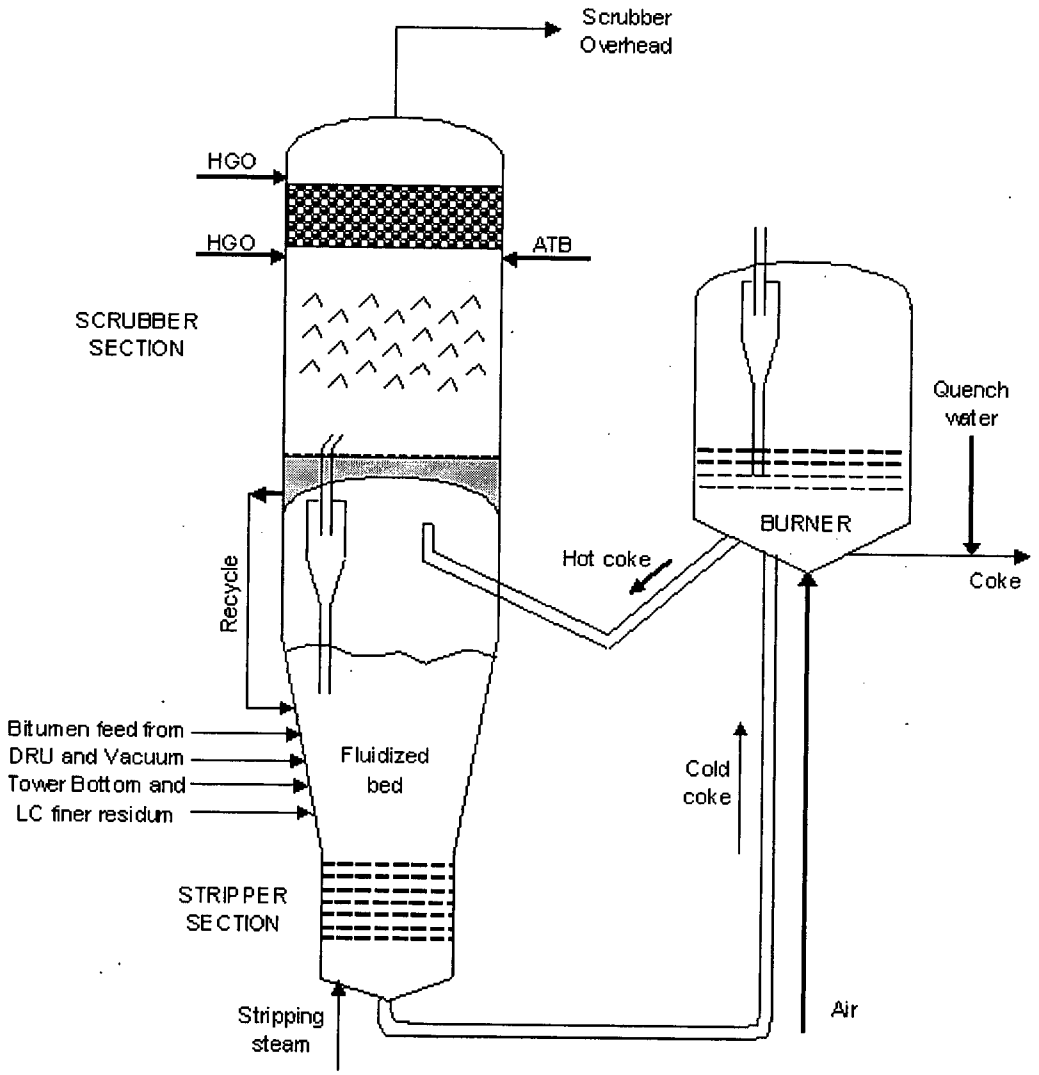

Figure 1.2 Schematic diagram for fluid coker

1.2 Fluid coker

The residuum, with atmospheric equivalent boiling points over 525°C, as well as feeds from the DRU, vacuum tower and LC Finer are sprayed in the reactor section of the fluid coker. Fig.1.2 is a schematic diagram of the fluid coker. Here the residua are thermally cracked at high temperature and near atmospheric pressure to give lighter products. The coking reaction occurs on the surface of the particles at temperatures of 510 – 530°C. Liquid that remains on the coke is

stripped off by the steam in the stripper section, located at the bottom of the reactor. The light fraction then moves towards the scrubber section of the fluid coker through the cyclone. In the cyclone the coke particulates and some liquid droplets are removed. The coke is sent to the burner where it is partially burned and recycled back to the fluid coker to supply heat for the coking reaction. From the burner, coke is removed as a by-product.

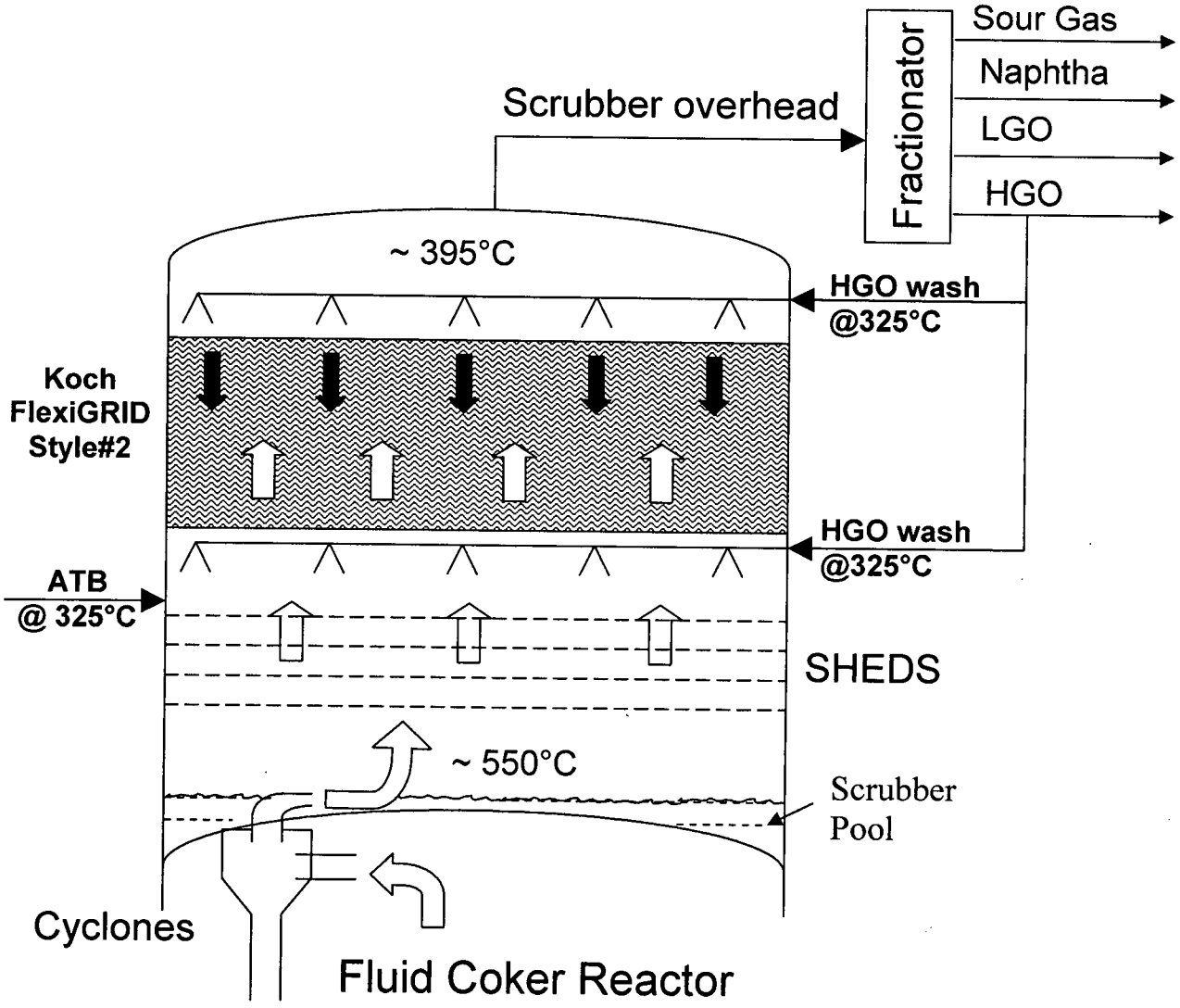

Figure 1. 3 Schematic diagram of scrubber in fluid coker

The scrubber section of the fluid coker, as shown in Fig.1.3, has three main parts – the scrubber pool at the bottom, six sets of sheds in the middle and the Koch-Grid at the top. The Koch-Grid considered in this work is FlexiGrid Style#2 structured packing with ten layers. In each layer

there are two sections of grid packing of 70 mm height. Each section has 93.3 elements of grid. Fig.1.4 shows an element of Flexigrid#2. An element contains 8 blades and each blade has 20 segments. The vertical parallel blades of the elements are held in a fixed position with welded cross members, as can be seen in Fig.1.4. During installation in the scrubber section, each successive section of the grid is rotated 45° to the previous section to achieve improved efficiency and enhance bed integrity. The blades are bent out an angle from the vertical to induce turbulent contact between the rising vapour and descending wash oil. There are no horizontal surfaces on the blade so that the wash oil can drain freely.

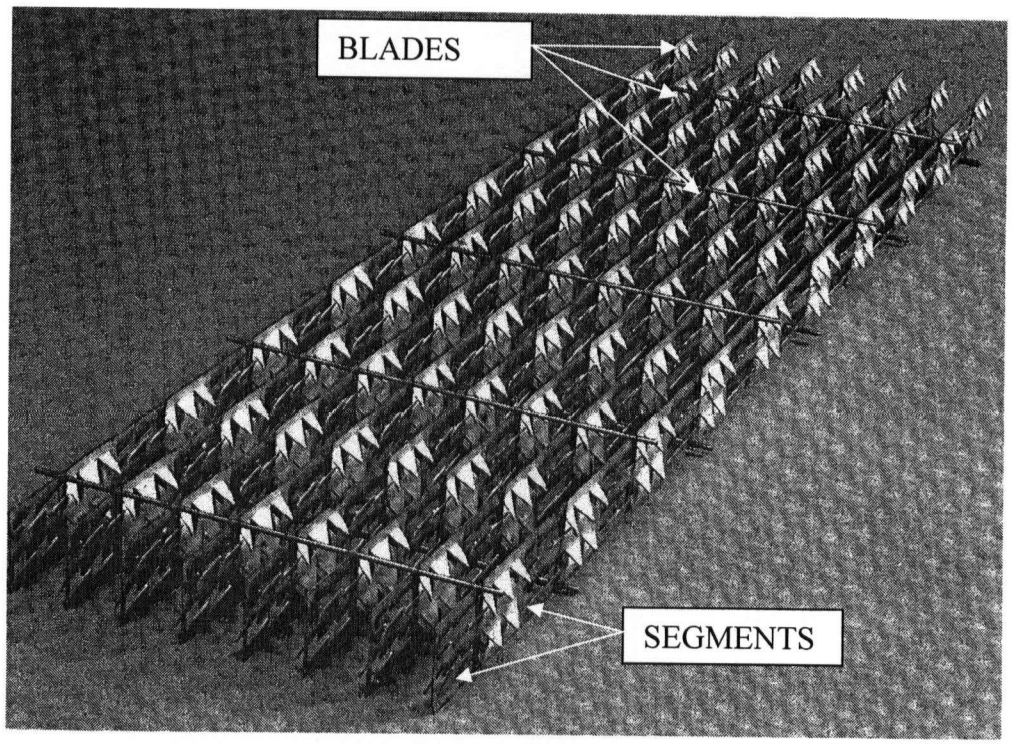

Figure 1.4 An element of Flexigrid #2, Kister (1992)

The main function of the scrubber is to scrub heavy components from the hot vapour rising from the fluid coker cyclones, by contacting with lower temperature falling HGO wash oil and ATB. Jankovic (2005) simulated the scrubber section of Syncrude Canada Ltd.'s fluid coker using HYSYS. Her simulation had many case-studies in which the process variables in the scrubber were changed. One of the aims of her work was to identify operating conditions which could

minimize the temperature of the grid section in order to reduce the tendency towards fouling and coking in this section of the scrubber.

1.3 Project objectives

In this project, Jankovic's work (2005) is extended to simulate the fouling process in the grid packing of the scrubber section in fluid coker. This can improve understanding of the rate of change of pressure drop across the grid section. The fouling process in the grid packed bed is assumed to occur as follows. In the shed vapour there are fine droplets of hydrocarbons, which enter the scrubber with the cyclone vapours. Some of these droplets are transported from the bulk vapour stream towards the surface and stick on the grid packing. In a droplet there are light and heavy fractions of hydrocarbons. The +524°C heavy fraction (known as pitch) in the droplet undergoes reactions to produce coke (toluene insoluble) and volatiles. Once the coke is formed, it sticks on to the surface of the grid packing. Due to the build up of solid coke, the voidage of the grid packing is reduced and the specific surface area of the packing increases. A decrease in the voidage of the grid packing increases the vapour velocity in the packing at a given throughput. Thus, the counter-current two-phase, vapour/liquid, pressure drop across the bed also increases. An understanding of these mechanisms can be developed through a mathematical model for vapour/liquid counter-current pressure drop across the grid packing, the transport and sticking of these droplets on the surface of the packing and the coking kinetics of the +524°C heavy fraction in the droplets.

Chapter 2: Mathematical model for pressure drop change due to coke deposition in the grid

The mathematical model for fouling in the structured packing of the scrubber grid is divided into three parts namely:

a) Calculation of pressure drop across the grid for counter-current vapour/liquid flow.
b) Calculation of deposition of droplets carried in the vapour and their attachment on the surface of the packing
c) Calculation of coke formation from the +524°C heavy fraction present in the droplet

2.1. Mathematical model for pressure drop across the grid

Packed columns for gas-liquid contacting are used extensively for absorption, stripping and distillation operations. The columns can be filled with either random packing or structured packing. In a packed column, the two phases usually flow in counter-current directions. The pressure drop across the packing is one of the key issues in deciding the design of the packed column. The first generalized correlation of packed column pressure drop was given by Sherwood et al. (1938) on the basis of laboratory measurements primarily on the air-water system. Later work with air and liquids other than water led to modification of the Sherwood correlation, first by Leva (1954) and later in a series of papers by Eckert. The generalized flooding-pressure drop chart by Eckert was modified and simplified by Stigle (1994). It includes pressure drop curves, as introduced by Leva (1954) and is often called the generalized pressure drop correlation (GPDC). This gives the pressure drop in the packed bed for all regimes namely pre-loading, loading and flooding; as well it gives the flooding point. The pressure drop can be understood in terms of the packed bed hydraulics. Fig. 2.1 gives the pressure drop for any packed bed flow regime. At low liquid flow rates (region A-B) the open cross-sectional area of the packing is about the same as in a dry bed. The pressure drop arises entirely by frictional losses through a series of openings, and therefore is proportional to the square of the gas flow rate. In structured packings, the openings are regular and of uniform size and pressure drop is due to

changes in gas flow direction.As liquid flow rates are raised, the liquid occupies some of the cross-sectional area, making the openings for gas flow smaller. The pressure drop curve will parallel A-B but will be displaced somewhat above it. At high liquid flow rates, the packing voids are filled up with liquid. A portion of the energy of the gas is used to support the liquid in the column and the pressure drop becomes proportional to the gas rate raised to a power different (usually lower) than 2 (region A'-B'). Most packed bed towers are designed to operate in this region.

For all liquid flow rates, as gas flow rate is raised, a point is reached when the gas velocity begins to interfere with the free drainage of liquid. Liquid will start to accumulate or "load" the bed, giving this region the name "the loading zone". The accumulation of liquid reduces the cross-sectional area available for gas flow, and therefore accelerates the pressure drop rise. In this region (B-C and B'-C') the slope of the curve increases to a power distinctly above 2. Liquid replaces vapour as the continuous phase as a column changes from normal to flooded operation. Some instability may occur at higher rates in this region. Upon further increases in gas flow rate, more liquid accumulates, until the liquid surface becomes continuous across the top of the packing. The slope of the curve increases, until it becomes very steep. When this occurs (points C and C') the column is flooded. This region is characterized by instability, entrainment and poor efficiency, and is therefore avoided.

A mathematical equation for the pressure drop in the pre-loading regime is given by the Robbins' equation, Kister (1992). The idea was extended from Leva (1954), who used a method of correcting dry pressure drop in the presence of water. That is for gas flow through dry packing, pressure drop may also be estimated by use of an orifice equation. For irrigated packing pressure drop increases because of the presence of liquid, which effectively decreases the available cross-section for gas flow. Robbins' equation, Kister (1992), used a packing factor to calculate the pressure drop, but this is not common practice.

Spiegel et al. (1992) calculated the pressure drop for structured packing for pre-loading. First the dry pressure drop was calculated and then the liquid hold-up was used to calculate the irrigated pressure drop. This model was tested with success for structured packings such as Mellapak 125X, 250X, 250Y and 500Y. Mellapak structured packings are used widely in industry for gas-

liquid absorption, scrubbing, etc., particularly where the chances of the packing getting fouled are less. The Spiegel et al. (1992) pressure drop model did not include the voidage of the packing. So, with this equation, the pressure drop change with voidage can not be evaluated. Mathematical models that included the voidage of the packing were given by Bravo et al. (1986) and Stichlmair et al. (1984). The latter model, referred to as Stichlmair–Bravo–Fair (SBR) model, was derived from a particle model, assuming that the packing is made up of particles distributed uniformly in a packed bed. Here the gas is assumed to flow around a particle packing which has a characteristic dimension and the liquid acts to increase this dimension by its adherence to the particle surface. The SBR model works better for random packings, but a few structured packings were also used to validate it. It can be used to calculate pressure drop in the pre–loading regime and also in the loading regime. But, a proper liquid hold-up equation for a specific system has to be specified for the use of this model. The model given by Bravo et al. (1986), Bravo–Rocha–Fair (BRF) equation, was derived from a cylindrical model where the gas is assumed to be flowing upward inside numerous small cylindrical channels having some characteristic dimension. As liquid flows down the walls of the same channels, it reduces the available cross-sectional area for the gas flow, thus increasing the pressure drop for a given gas flow rate.

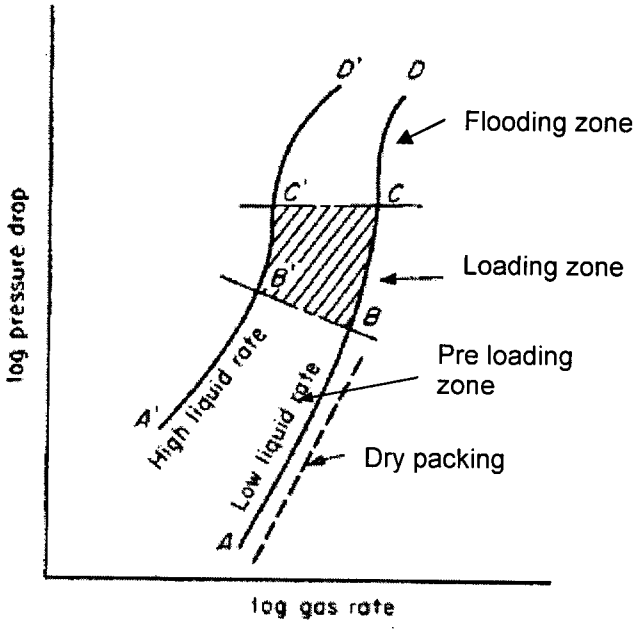

Figure 2.1 Packed bed flow regimes. Perry (1997)

The BRF model for pressure drop is for the pre-loading regime only and works well for structured packing. The pressure drop caused by the flow resistance of the bed depends significantly on the porosity of the bed. The higher the porosity the lower is the pressure drop.

Pressure drop prediction for gas/liquid counter-current flow can be done by various methods. The interpolation of pressure drop data may be more accurate and reliable than prediction by correlation. However it requires that an interpolation chart be available. This may be difficult to computerize.

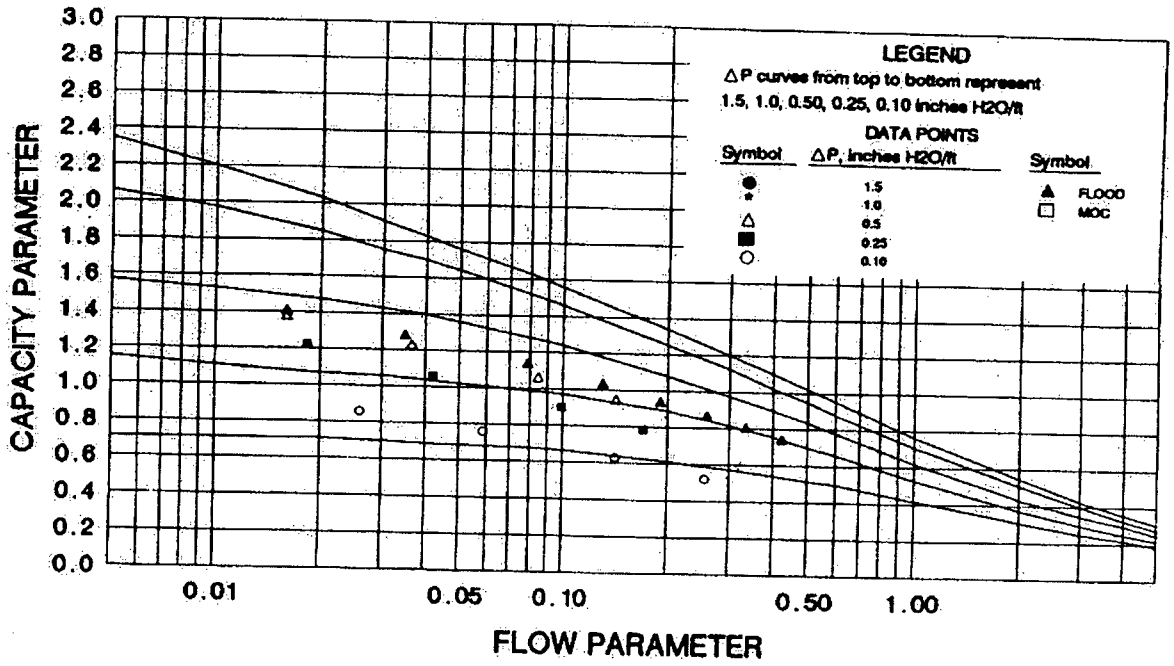

Figure 2.2 GPDC chart for Koch FlexiGrid #2, Kister (1992)

Superimposing experimental data points for the packing on the curves of Generalized Pressure Drop Correlation interpolation chart converts the GPDC chart into an interpolation chart for the packing. Pressure drops are calculated by interpolating the plotted pressure drop data. Fig. 2.2 shows the GPDC chart for Koch Flexigrid #2 and pressure drop in this chart is calculated in inches of water column per foot of packed bed height. In this chart, the abscissa of the correlation is the dimensionless flow parameter, given by

$$F_{lv} = \frac{L}{G}\left(\frac{\rho_g}{\rho_l}\right)^{0.5} \tag{2.1}$$

and the ordinate is the capacity parameter, given by

$$Capacity\ Parameter = C_S\ F_P^{0.5}\ \nu^{0.05} \tag{2.2}$$

ν is the kinematic viscosity of the liquid and C_S is the C-factor, i.e., the superficial gas velocity corrected for vapour and liquid densities, given by

$$C_S = u_g \sqrt{\frac{\rho_g}{\rho_l - \rho_g}} \tag{2.3}$$

F_p is the packing factor, which is an empirical factor characteristic of the packing size and shape. F_p for Koch Flexigrid #2 packing is 4, Kister (1992).

Another method to predict pressure drop is by the Stichlmair-Bravo-Fair (SBF) model. SBF assumes that packings are spherical in shape and are distributed uniformly in the packed bed, Fig.2.3. To use this model, first the dry pressure drop is evaluated and then the irrigated pressure drop is calculated.

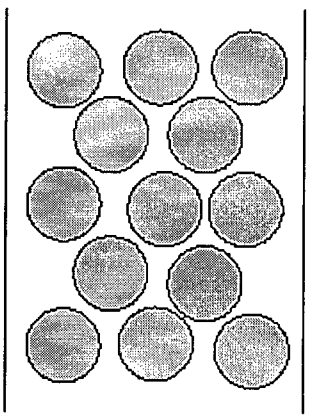

Figure 2.3 Packing in the packed bed represented by particle model

The dry pressure drop per unit height in the packed bed, with no liquid loading, is given as

$$\frac{\Delta P_{dry}}{H} = \frac{3}{4}\varsigma_0 \frac{1-\varepsilon}{\varepsilon^{4.65}} \rho_g u_g^2 \frac{1}{d_{eq}} \tag{2.4}$$

Here, ς_0 denotes the friction factor of a single particle and not the whole bed and can be calculated from the equation,

$$\varsigma_0 = \frac{C_1}{\mathrm{Re}_g} + \frac{C_2}{\mathrm{Re}_g^{1/2}} + C_3 \tag{2.5}$$

where C_1, C_2 and C_3 are constants that depend on the type of packing. For structured packing the constants, $C_1 = 18$, $C_2 = 4$ and $C_3 = 0.2$, Stichlmair (1998), and the Reynolds Number is given as

$$\mathrm{Re}_g = \frac{u_g d_{eq} \rho_g}{\mu_g}$$

The case for an irrigated bed developed by Stichlmair (1984) is extended here to account for a deposit on the packing. For the irrigated pressure drop, the clean packing voidage, ε , will change from the dry case. The voidage for an irrigated bed is:

$$\varepsilon_{irr} = \varepsilon - h_T, \quad \text{or} \quad \varepsilon_{irr} = \varepsilon\left(1 - h_T/\varepsilon\right) \tag{2.6}$$

For the clean condition, $h_T = h_l$, where h_l is the liquid holdup. In the presence of fouling h_f is the solid deposit holdup in the grid and $h_T = h_l + h_f$.

The liquid holdup below the loading point is given by $h_l = 0.555\, Fr_l^{1/3}$, where the Froude number, $Fr_l = u_l^2 \frac{a_p}{g\,\varepsilon^{4.65}}$, (Stichlmair, 1984). This is a generalized form for liquid holdup that is valid for both random and structured packings. The correlation does not take into account any properties of the liquid, and has been validated for the air/water system only.

The change in packing particle diameter for an irrigated bed with fouling is described by

$$\frac{1-\varepsilon_{irr}}{d_{eqirr}^3}=\frac{1-\varepsilon}{d_{eq}^3}, \quad \text{or} \quad d_{eqirr}=d_{eq}\left[\frac{1-\varepsilon\left(1-h_T/\varepsilon\right)}{1-\varepsilon}\right]^{1/3} \tag{2.7}$$

where

$$d_{eq}=\frac{6\left(1-\varepsilon\right)}{a_p} \tag{2.8}$$

The friction factor of an irrigated particle is given as

$$\varsigma_{0irr}=\varsigma_0\left(\frac{d_{eq,irr}}{d_{eq}}\right)^C \tag{2.9}$$

and C is given by

$$C=\frac{-\frac{C_1}{\mathrm{Re}_g}-\frac{C_2}{2\,\mathrm{Re}_g^{1/2}}}{\varsigma_0} \tag{2.10}$$

Finally the friction factor of an irrigated particle is given as

$$\varsigma_{0irr}=\varsigma_0\left\{\frac{1-\varepsilon\left(1-h_T/\varepsilon\right)}{1-\varepsilon}\right\}^{C/3} \tag{2.11}$$

In the particle model, the pressure drop of the dry and the irrigated packing is described by the same Eq. (2.4). Hence, the pressure drop per unit height of an irrigated packing is:

$$\Delta P=\frac{3}{4}\varsigma_{0irr}\frac{1-\varepsilon_{irr}}{\varepsilon_{irr}^{4.65}}\rho_g\,u_g^2\,\frac{1}{d_{eqirr}}, \tag{2.12}$$

Substituting ς_{0irr} , ε_{irr} *and* d_{eqirr} from Eqs.(2.11), (2.6) and (2.7), respectively, into Eq. (2.12), the final form of the equation for irrigated pressure drop is:

$$\frac{\Delta P}{H}=\frac{3}{4}\varsigma_0\left\{\frac{1-\varepsilon\left(1-h_T/\varepsilon\right)}{1-\varepsilon}\right\}^{C/3}\frac{1-\varepsilon\left(1-h_T/\varepsilon\right)}{\left\{\varepsilon\left(1-h_T/\varepsilon\right)\right\}^{4.65}}\rho_g\,u_g^2\,\frac{1}{d_{eq}\left\{\dfrac{1-\varepsilon\left(1-h_T/\varepsilon\right)}{1-\varepsilon}\right\}^{1/3}} \qquad (2.13)$$

The pressure drop of an irrigated packing is related to the pressure drop of a dry packing by combining Eq.(2.4) and Eq.(2.13) which yields:

$$\frac{\Delta P}{\Delta P_{dry}}=\left(\frac{1-\varepsilon\left(1-\left(h_T/\varepsilon\right)\right)}{1-\varepsilon}\right)^{(2+C)/3}\left(1-\left(h_T/\varepsilon\right)\right)^{-4.65} \qquad (2.14)$$

A third method for pressure drop prediction is via the Bravo-Rocha-Fair (BRF) model. BFR assumes that the packed bed has cylindrical channels, which can be seen in Fig.2.4. Here the gas and liquid flow counter-currently.

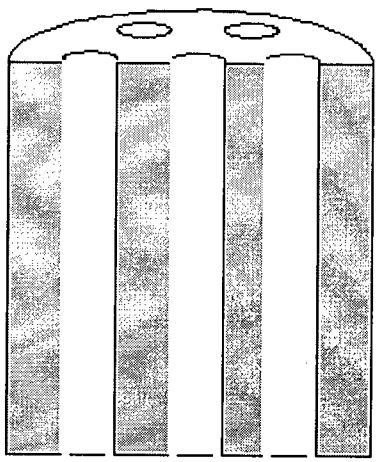

Figure 2.4 Packing in the packed bed represented by cylindrical model

For this channel model, the equivalent diameter of the channel is defined as

$$d_{eq} = \frac{4 \cdot \varepsilon}{a_p} \tag{2.15}$$

The dry pressure drop per unit height caused by the frictional resistance of gas flow is related by Fanning or Darcy type relationships:

$$\Delta P_{dry} = \frac{f \ \rho_g \ u_{ge}^2}{d_{eq}} \tag{2.16}$$

and

$$u_{ge} = \frac{u_g}{\varepsilon} \tag{2.17}$$

The voidage, ε , is the same as defined in Eq.(2.6).

Random-type packing friction factors can be correlated by the general relationship:

$$f = C_4 + \frac{C_5}{\mathrm{Re}_g} \tag{2.18}$$

This correlation for friction factor is also valid for structured packing, Bravo et al. (1986), and hence is used here. The Reynolds number is defined as $\mathrm{Re}_g = \frac{d_{eq} \ u_{ge} \ \rho_g}{\mu_g}$. This friction factor, f, is applicable to gas flow only, and incorporates both turbulent and laminar flows.

When the packing is irrigated, the influence of the presence of liquid may be related to the fractional liquid holdup h_l. Bemer and Kalis (1978) gave a simple form for h_l ,

$$h_l = A \ Fr_l^{\alpha} \tag{2.19}$$

where A, α = constants for the packing type, and the Froude number is given by $Fr_l = \frac{u_l^2}{d_{eq} \ g}$.

It should be noted that Eq.(2.19) is applicable only below the loading point, where the holdup is not influenced by the gas velocity.

Pressure drops through beds of irrigated structured packings have been successfully correlated by Bemer and Kalis (1978) in terms of the dry pressure drop using

$$\frac{\Delta P}{H} = \frac{\Delta P_{dry}}{H}\left[1/\left(1 - K' h_l\right)\right]^5 \tag{2.20}$$

where K' is a constant characteristic of the packing type and size. Eq.(2.19) can be combined with Eq.(2.20) to give

$$\frac{\Delta P}{H} = \frac{\Delta P_{dry}}{H}\left[1/\left(1 - C_6\, Fr^{\alpha}\right)\right]^5 \tag{2.21}$$

A final correlating equation results from combining Eqs. (2.16), (2.18) and (2.21) :

$$\frac{\Delta P}{H} = \left[C_4 + \frac{C_5}{\mathrm{Re}_g}\right]\left[\frac{\rho_g\, u_{ge}^2}{d_{eq}}\right]\left[1/\left(1 - C_6\, Fr_l^{\alpha}\right)\right]^5 \tag{2.22}$$

The validations of the BRF and SBF models are done using data for the air-water system. The properties of air and water are given in Table.2.1.

Table 2.1 Properties of air and water @ 1 atm., 20°C, Dean (1998)

	Air	**Water**
Density, kg/m^3	1.205	998.2
Viscosity, cP	0.0182	1.002
Surface Tension, dynes/cm	...	72.88

The Koch-Glitsch technical brochure (2004) gives the pressure drop chart for Koch FlexiGrid #2 which is shown in Fig.2.5.

In the BRF model, Eq.(2.16) with Eq.(2.17) is a general equation used for calculating the dry pressure drop for various structured packings (Gempak, Sulzer, Flexipac) with C_4 and C_5

constants as 0.171 and 92.7 respectively, (Bravo et al., 1986). Constants C_4 and C_5 were fitted for the Koch Flexigrid #2 structured packing and are found to give good agreement between calculated and graphical dry pressure drops, Fig.2.6, within $\pm 4\%$. The respective values for C_4 and C_5 are 0.26 and 92.7.

Eq.(2.21) can be written as

$$100\left[1-\frac{\Delta P_{dry}}{\Delta P}\right]^{0.2} = C_6\, 100 Fr_l^{\alpha} \tag{2.23}$$

For various values of the liquid loading and gas flow rates, the constant α was adjusted such as to get Eq.(2.23) as a straight line ($R^2 = 0.9983$). This is shown by Fig.2.7. The values of C_6 and α were found to be 3 and 0.357 respectively.

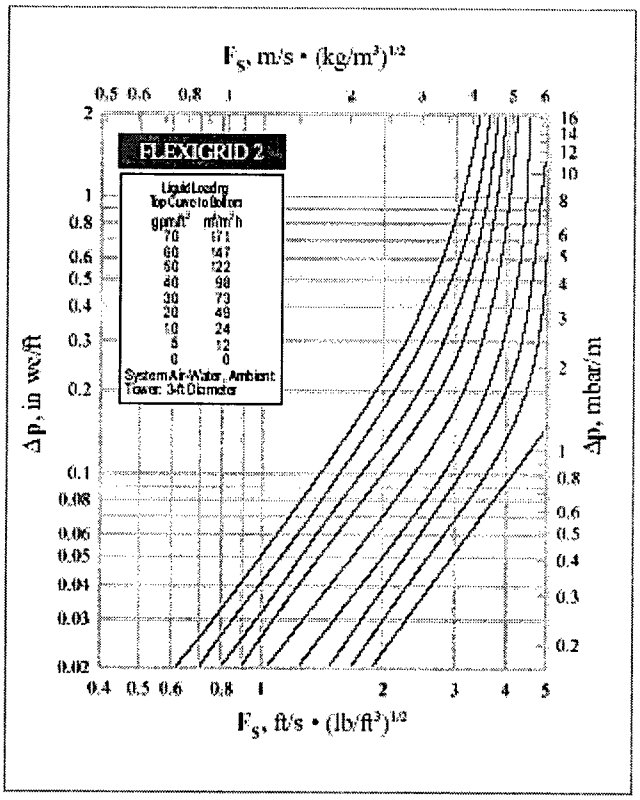

Figure 2.5 Pressure drop chart for Flexigrid #2 for air-water system Koch-Glitsch technical brochure (2004)

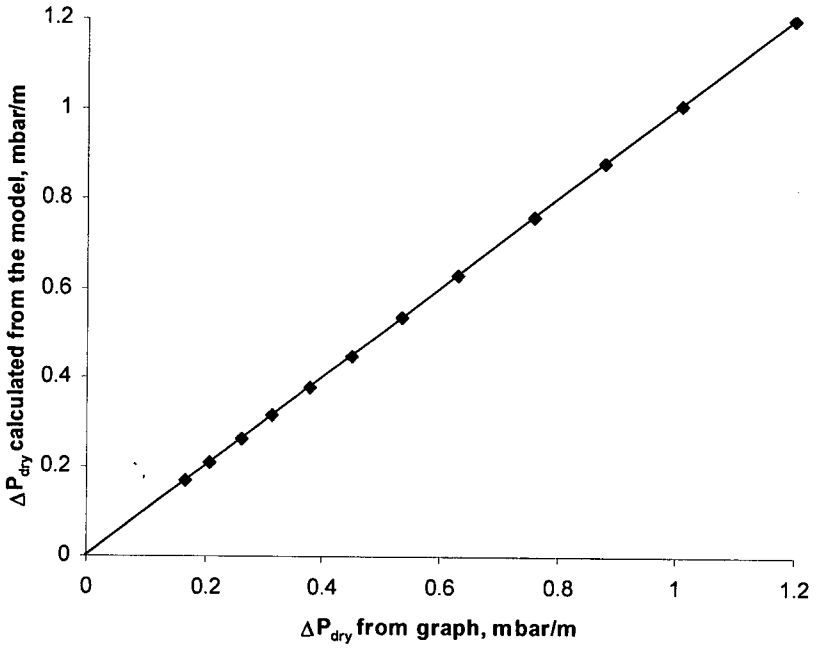

Figure 2.6 The pressure drop calculated from Bravo-Rocha-Fair model and pressure drop from the chart, Fig.2.5, for dry conditions

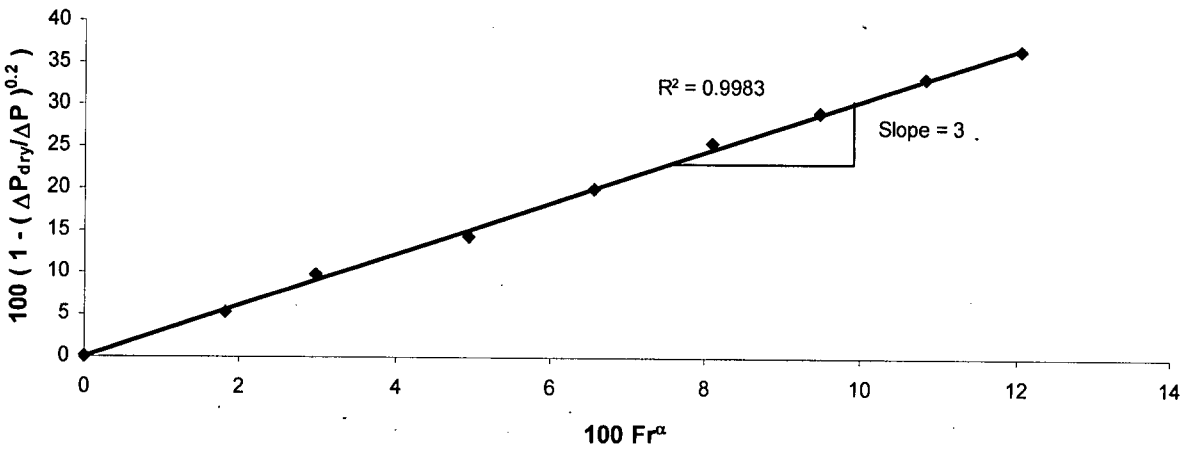

Figure 2.7 Constants for liquid holdup, Eq.(2.22), are determined using several gas and liquid rates

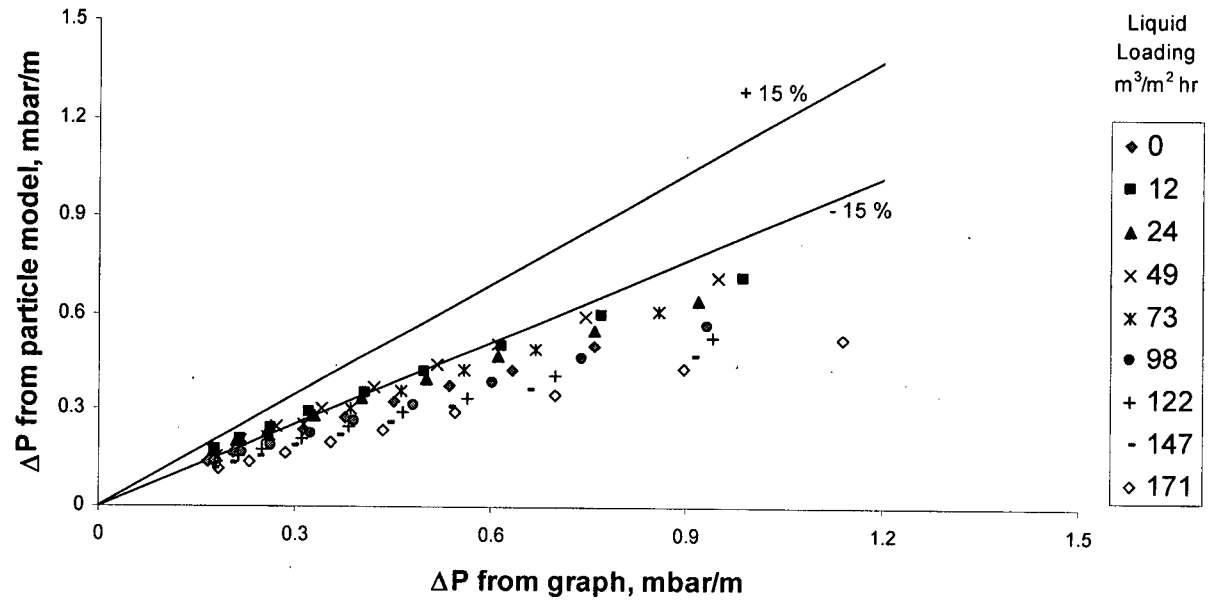

Figure 2.8 Pressure drop calculated from SBF model and graphical pressure drop given in Koch-Glitsch technical brochure (2004) for different liquid loadings.

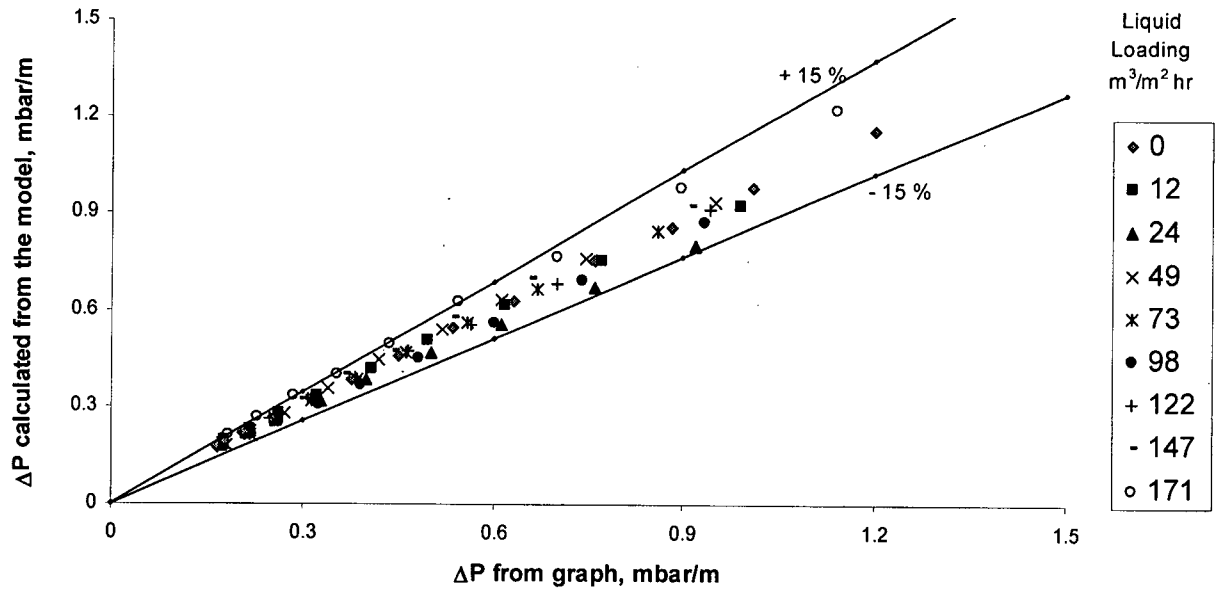

Figure 2.9 Pressure drop calculated from BRF model and graphical pressure drop as given in Koch-Glitsch technical brochure (2004) for different liquid loadings.

Fig. 2.8 compares the calculated pressure drop from the SBF model and the graphical pressure drop from the Koch-Glitsch technical brochure (2004). Most of the data points for pressure drop

of the SBF model fall outside ±15% of the pressure drop from the graph. The validity of the model is more specific to a range of gas factor, F_s, to the liquid loading in the tower. Table 2.2 gives the validity of the model for the liquid loading for a specific range of F_s. It has to be noted that above the liquid loading 73 m^3/m^2 h, the model fails for any value of F_s.

Fig.2.9 shows a good agreement between pressure drop calculated by the BRF model and the graphical pressure drop given in the Koch-Glitsch technical brochure (2004). The results were within ±15%.

Since the BRF model showed good agreement with the graphical data in the Koch-Glitsch technical brochure (2004), this model is selected for calculation of pressure drop across the grid.

Table 2.2 Conditions of validity of the SBF model for different gas and liquid loads within ±15% .

Liquid loading m^3/m^2 h	**Vapour flow F factor, F_s, $m/s*(kg/m^3)^{1/2}$**
0	<1.8
3	< 2.5
6	<3.3
9	<3.3
12	<3.1
15	<2.8
18	<2.6
21	<2.6
24	<2.4
30	<2.3
37	<2.3
42	<2.3
49	<2.3
55	<2.0
73	<1.2

2.2 Mathematical model for transport and attachment of droplet on the grid

The transport of droplets from a turbulent flow stream to an adjacent surface under isothermal condition is considered here. Many hydrodynamic theories of particle deposition have been formulated on the assumption of perfect stickability, (Papavergos and Hedley, 1984). Starting with sub-micron particles, three transport mechanisms progressively predominate in turbulent flow as the particle size increases. The three regimes for particle deposition are diffusion, inertia and impaction. Here the droplets are assumed to be fine particles, carried by the shed vapour. They are assumed to be uniformly distributed in the vapour space. Droplet transport is considered to be isothermal as the temperatures of the bulk fluid and the packing surface are equal. The transport mass flux of the droplets to the deposition surface, ϕ_d , in kg/m^2s, can be written as,

$$\phi_d = k_t (c_b - c_s) = k_d c_b \qquad (2.24)$$

where c_b = bulk concentration of the droplets in vapour, c_s = concentration of droplets near the surface. When the deposition surface is clean (no adhering particles) $c_s = c_w$, where c_w = concentration of the droplets on the packing surface. If it is assumed that all droplets that arrive at the surface adhere to it, $c_s = 0$ and the transport coefficient, k_t becomes identical to the deposition coefficient, k_d, (Epstein, 1997).

Fig.2.10 shows a schematic diagram of the liquid layer on the wet packing surface, with droplets distributed uniformly in the vapour. The droplets are heavy hydrocarbons whereas the wetted layer is of lighter hydrocarbons. The droplets are assumed to retain their identity as a second phase in the liquid film over the time it takes to reach the solid surface. The deposition on the wall surface is thereby treated as a process of mass transfer in vapour and liquid layers followed by droplet attachment. The steady state mass deposition flux, ϕ_d , kg/m^2s, is given as,

$$\phi_d = k_{tg}(c_b - c_{i,g}) = k_{tl}(c_{i,l} - c_{b,l}) = k_w(c_{b,l} - c_w) = k_a c_w \qquad (2.25)$$

Eq.(2.25) can be written as,

$$\frac{\phi_d}{k_{tg}} = \left(c_b - c_{i,g}\right) \tag{2.26}$$

$$\frac{\phi_d}{k_{tl}} = \left(c_{i,l} - c_{b,l}\right) \tag{2.27}$$

$$\frac{\phi_d}{k_w} = \left(c_{b,l} - c_w\right) \tag{2.28}$$

$$\frac{\phi_d}{k_a} = c_w \tag{2.29}$$

where $c_{i,g}$ and $c_{i,l}$ are the concentration of the droplets at the vapour-liquid interface, and, k_{tg}, k_{tl}, k_w and k_a are the transport coefficients of the droplet in the vapour, liquid and near the wall, and the attachment coefficient respectively. Eq.(2.29) is the equation for particle attachment on the surface and is assumed to follow first-order kinetics.

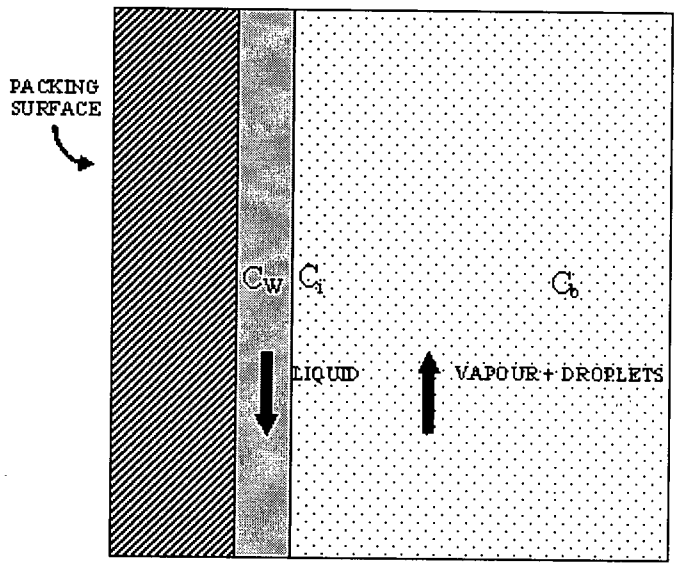

Figure 2.10 Wet surface of the grid

Hence, the deposition flux of droplets to the wet surface can be written as

$$\phi_d = \frac{c_b}{\frac{1}{k_{tg}} + \frac{1}{k_{tl}k} + \frac{1}{k_w k} + \frac{1}{k_a k}} \tag{2.30}$$

Fig. 2.11 shows a dry packing surface with droplets in the vapour stream. Here the deposition flux for droplets to the dry surface can be written as,

$$\phi_d = \frac{c_b}{\frac{1}{k_{tg}} + \frac{1}{k_a}} \tag{2.31}$$

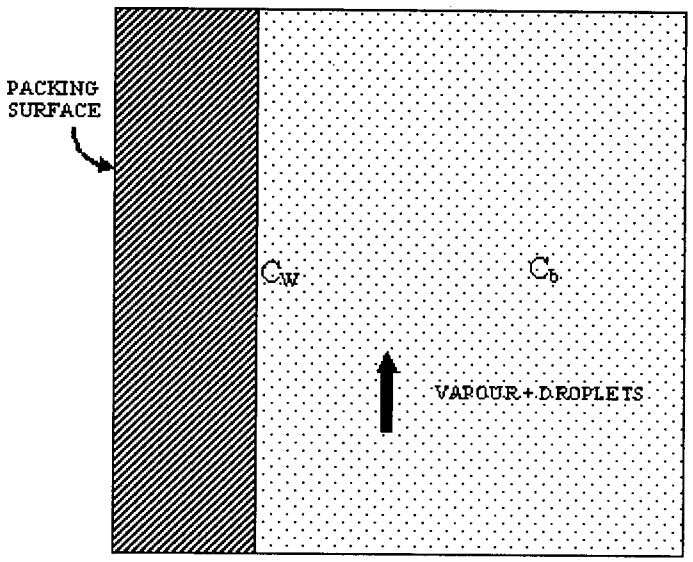

Figure 2.11 Dry surface of the grid

Equilibrium is assumed to exist at the vapour-liquid interface and the concentration of droplet in liquid at the interface is related to the concentration of droplet in the vapour and equilibrium relation is given as $c_{i,l} = K * c_{i,g}$. In the present work, the resistance of the liquid film at the grid surface is considered negligible. Also, the droplet concentrations $c_{i,g}$ and $c_{i,l}$ are considered to be equal. The transport coefficient k_{tg} and k_{tl} can be calculated based on the droplet's transfer to the packing surface. As stated previously, the droplet transfer regime may be defined as diffusion, inertia or impaction.

In the diffusion regime, the droplets are so small that they can be assumed to be the size of large molecules. They move with the fluid and are carried to the wall by the Brownian motion of the fluid molecules, through the viscous sub-layer in a turbulent flow. So k_t becomes equivalent to the conventional mass transfer coefficient, k_m, which can be obtained from empirical correlations

or theoretical equations. To use these relations requires knowledge of the Brownian diffusivity, which for a dilute suspension of small spheres, is given by the Stokes-Einstein equation, (Bird et al., 2001),

$$D = \frac{k_B T}{3\pi \mu d_d} \tag{2.32}$$

For the present application, the surface of the packing is divided into many short rectangular parts as seen in Fig.3.4. Some of these rectangular parts are taken to be wet by the wash oil and some are dry. The mass transfer coefficient of the droplet in vapour, k_{mg}, on the flat rectangular surface is given by the theoretical equation (Skelland, 1974), for fully-developed flow over a plate of length x.

$$N_{Sh,avg} = \frac{k_{mg} x}{D} = 0.664 \left(N_{\mathrm{Re},x}\right)^{1/2} \left(N_{Sc,g}\right)^{1/3} \tag{2.33}$$

Eq. (2.33) is valid in the range of $N_{Sc} > 0.6$ and $N_{Re,x} < 3\text{x}10^5$ (for laminar flow), where, $N_{Sh,avg}$ is the average Sherwood number and the local Reynolds number and Schmidt number are defined as,

$$N_{\mathrm{Re},x} = \frac{x u_g \rho_g}{\mu_g} \quad \text{and} \quad N_{Sc,g} = \frac{\mu_g}{\rho_g D} \tag{2.34}$$

The mass transfer coefficient in the liquid film on the surface of the packing, k_{ml}, on the flat surface is given by the theoretical equation for fully developed flow in a liquid film (Skelland, 1974),

$$N_{Sh,avg} = \frac{k_{ml} x}{D} = 0.783 \left(N_{\mathrm{Re},film}\right)^{1/9} \left(N_{Sc,l}\right)^{1/3} \left(\frac{x^3 \rho_l^2 g \cos\beta}{\mu_l^2} \right)^{2/9} \tag{2.35}$$

This equation will apply for a film of Newtonian liquid and the film is in laminar flow. Eq.(2.35) is valid for $N_{Re,film} < 2000$, where, $N_{Sh,avg}$, $N_{Re,film}$ and $N_{Sc,l}$ are the average Sherwood number,

Reynolds number and Schmidt number for the liquid over the rectangular plate respectively. Here x is the length of the rectangular plate over which the liquid flows, g is the gravitational constant and β is the inclination angle of the flat plate with respect to vertical. $N_{Re,film}$ and $N_{Sc,l}$ are defined as

$$N_{\mathrm{Re},film} = \frac{4\Gamma}{\mu_l} \; and \; N_{Sc,l} = \frac{\mu_l}{\rho_l D} \tag{2.36}$$

where liquid loading $\Gamma = \frac{L}{w}$, *kg/m s*, L is the flowrate of the liquid over the flat plate and w the width of the rectangular plate.

The wall shear stress when a liquid is flowing on an inclined flat plate is given as

$$\tau_{wl} = \rho_l \, g \, \delta \, \cos\beta \tag{2.37}$$

and the liquid film thickness, δ ,is given as (Bird et al., 2001)

$$\delta = \left(\frac{3\Gamma \mu_l}{\rho_l^2 \, g \cos\beta} \right)^{1/3} \tag{2.38}$$

In this work the minimum and maximum droplet diameters are taken as 0.1 (assumed) and 11 μm respectively. In Fig.1.3, the cyclones are below the scrubber section of the fluid coker. The vapour coming from the fluid coker reactor has droplets and coke particles. In this study it is assumed that only droplets are present in the cyclone vapour. Based on the cyclone dimensions, the cut-point diameter for the droplets was 11 μm, Jankovic (2005). The HGO flow rate range considered was 44 kg/s (24 kbpd) to 73 kg/s (40 kbpd). For the above mentioned HGO wash flow rates and with a wetted fraction of packing as 0.9, the thickness of liquid film on the packing is between 230 to 300 μm.

Vapour is flowing over the flat plate and the flow near the wall is laminar. The wall shear stress for the laminar region when the vapour is flowing on a flat plate of length x is given by (Schlichting, 1968),

$$\tau_{wg} = 0.332\sqrt{\frac{u_g^3 \mu_g \rho_g}{x}} \tag{2.39}$$

In the inertia regime, the droplets are large enough that turbulent eddies give them a free flight velocity that is not completely dissipated in the viscous sub-layer of the vapour. They have sufficient momentum to reach the surface of the packing. Friedlander and Johnstone (1957) were among the first to develop the concept of particle deposition in the inertia regime using the stopping distance of the particle. Papavergos and Hedley (1984) summarized many theories of particle deposition in their review paper. These authors divided the theories into two groups namely those based on the classical concept of turbulence and eddy diffusion and those based on probabilistic approaches such as random walk, (Hutchinson et al., 1971) and turbulent bursts, (Cleaver and Yates, 1975). The results are commonly presented in terms of the dimensionless transport coefficient, $k_t^+ = k_t / u^*$ and dimensionless particle relaxation time, t_d^+, which is defined as follows.

$$t_d^+ = \frac{\rho_d d_d^2}{18\mu} \cdot \frac{(u^*)^2}{\nu} \tag{2.40}$$

where u^* is the friction velocity, and is defined as

$$u^* = \sqrt{\frac{\tau_w}{\rho}} \tag{2.41}$$

The wall shear stress, τ_w, is given by Eq.(2.37) and Eq.(2.39), respectively, for vapour and liquid fluids on the surface.

Papavergos and Hadley (1984) recommended an empirical equation for k_t^+ for different ranges of t_d^+. If t_d^+ is in the range of $0.2 < t_d^+ < 20$, the droplet is considered to be in the inertial regime and the corresponding k_t^+ is given by the empirical equation,

$$k_t^+ \cong 0.00035\left(t_d^+\right)^2 \qquad (2.42)$$

If $t_d^+<0.2$, the droplet is in the diffusion regime and for $t_d^+ > 20$, the droplet is in the impaction regime. k_t^+ for the impaction regime is approximated as $k_t^+ \cong 0.18$ by Papavergos and Hadley (1984). Papavergos and Hadley (1984) successfully validated the empirical relationships for the non-dimensionalized transport coefficient (k_t^+) for the inertia regime and impaction regime defined above by fitting them with experimental data from Liu et al. (1974) on liquid aerosol droplet deposition from the gas phase for fully developed flow in a tube and from Forney et al. (1974) on ragweed pollen and polystyrene sphere deposition from the gas phase in fully-developed turbulent flow in a tube. In the vapour phase, the droplets which are in the inertia and impaction regimes lose their momentum when they pass through the liquid film to reach the surface. Due to this, some of these droplets in the liquid film might diffuse to the surface. The droplet transport regime depends on the dimensionless particle relaxation time, t_d^+, which is given by Eq.(2.40). The viscosity term in this equation is high for a liquid. So t_d^+ will be lower for droplets having the same diameter in the liquid than in vapour.

The probability that the droplet will stick on the surface depends on the attachment rate coefficient, k_a, as given in the Eq.(2.28). Epstein (1997), wrote the attachment rate constant, k_a, at the surface as the product of an Arrhenius term and the fluid residence time near the surface, based on the concept that the greater the residence time, the greater the opportunity for chemical reaction to promote attachment. This idea had also been explored by Paterson and Fryer (1988). The reaction plus attachment rate constant (k_a) is defined as

$$k_a = \frac{e^{-E/RT}\nu}{k'' u^{*2}} \qquad (2.43)$$

where the constant k'' includes both the Arrhenius pre-exponential factor and the residence time proportionality factor and E is the activation energy for the reaction plus attachment for a droplet on the surface. Epstein (1997) successfully implemented this concept by validating the experimental data from Crittenden et al. (1987) on polystyrene deposition from the liquid phase

polymerization of styrene in established turbulent flow through a tube. It was also shown to fit dilute aqueous suspensions of silica and polystyrene spheres flowing in isothermal turbulent flow through a rectangular channel by Vasak et al. (1995). Rose et al. (2000) again implemented this concept for initial chemical reaction fouling using a dilute protein solution on a heated surface. Fahiminia et al. (2003) verified the model experimentally for calcium sulphate scaling under non-boiling, fully-turbulent flow conditions. The temperature dependence of the reaction plus attachment for the droplet on the surface is assumed to be weak for a physical phenomenon if the activation energy, E, is low. By contrast if the attachment of the droplet to the surface takes place by a chemical reaction, i.e. is temperature sensitive, the value of the activation energy, E, will be higher. As stated by Watkinson (1992), an activation energy, E, of the order of 20 kJ/mol (~ 5 kcal/mol) may represent a physical process, or combined effect of several chemical reactions. Values above 40 kJ/mol (~10 kcal/mol) are assumed to represent a chemical reaction. In the present work, since the nature of the adhesion step was unknown, both extremes were represented by choosing activation energies of 5 and 75 kcal/mol.

The above equations, (Eqs.(2.29), (2.31) and (2.43)), permit the calculation of the mass of the droplets which adhere to the surface over time.

The basis of this work is that the pressure drop across the grid to reach 1" H_2O in one year. If the resistance due to liquid film at the grid surface is not considered as negligible then k'' given by Eq.(2.43) will decrease. When the droplet concentrations $c_{i,g}$ and $c_{i,l}$ are not equal, i.e., the equilibrium constant, $K<1$, then k'' will increase.

2.3 Coking kinetics

The temperature range of the structured packing grid is 370 – 400°C, which can be seen in Figs. 4.1, 4.7 and 4.9. At these temperatures there is a tendency for coke formation from heavy hydrocarbons. The fractional amount of coke formed may be small but, over time, the coke forming on the packing surface will significantly affect the overall pressure drop in the grid. Yue et al. (2004) have done a study of Athabasca pitch (+524°C), heavy gas oils, and their mixtures forming toluene insolubles (coke) in isothermal batch reactors at atmospheric pressure and temperatures ranging from 360 to 420°C. Their results for an open reactor where volatiles were

free to escape from the reactor can represent conditions in the grid. The model which they suggested is given below.

The pitch (+524°C fraction) decomposition produces volatiles, coke precursors (asphaltenes) and coke. The volatile yield for the pitch with a simple first-order empirical decomposition reaction model is given by

$$dV/dt = k(V^* - V) \qquad (2.44)$$

where V^* is the maximum potential volatile forming species in the oil. The Microcarbon Residue (MCR) is the coke yield in an experimental test used in the oil industry to measure the coke-formation tendency of oil. Yue et al. (2004) set,

$$V^* = 1 - MCR$$

where, MCR = micro carbon residue(gm/gm of +524°C).With the temperature dependence of the rate constant,

$$k = k_0 \exp(-E_R/RT),$$

where E_R = 197.5 kJ/mol and $k_0 = 1.2334 \times 10^{13}$ min^{-1}

Table 2.3 Characteristics of Athabasca Pitch, Yue et al.(2004)

Initial Boiling Point (IBP), °C		524
Ash (*wt%*)		1.5
MCR (*wt%*)		27.1
Solvent fractions	Asphaltenes (*wt%*)	32
	Saturates (*wt%*)	8
	Aromatics (*wt%*)	32
	Resins (*wt%*)	28

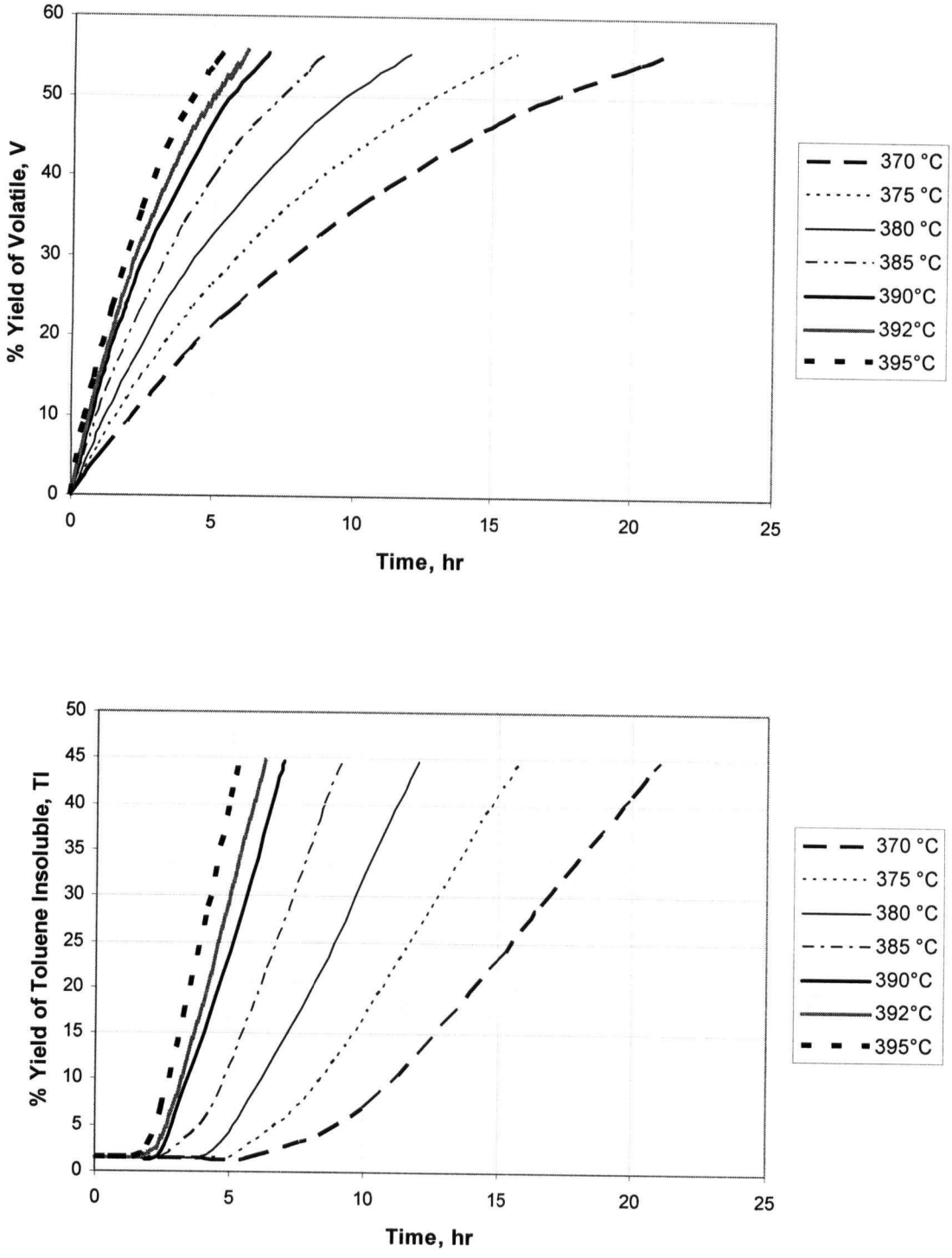

Figure 2.12 Yield of volatiles and toluene insolubles with time for Athabasca pitch at different temperatures (Yue et al. 2004)

The volatile yield (gm volatile / gm of +524°C), V, calculated as a function of temperature and time is given as

$$V = V^* \{ 1 - exp[- k_0 exp(- E_R/RT) t] \} \quad (2.45)$$

The toluene insoluble yields (gm toluene insoluble / gm of +524°C), TI, for various reaction times and temperatures were reported to depend only on the volatile yield and were correlated by

$$TI = TI_0 - 0.1768 (V - 0.23) + 4.682 (V - 0.23)^2 \quad (2.46)$$

TI_0 represents the ash and coke present in the feed. In the above equation, once the volatile yield exceeds 23% for 100% of +524°C (pitch) as reactant, the toluene insoluble starts to form. This can be seen in the Fig.2.12, which gives the experimental results for Athabasca pitch carried out at different temperatures.

The characteristics of Athabasca pitch are given in Table 2.3. The MCR for this pitch is given as 27.1 *wt%*. Using this value volatile yield and toluene insoluble yield are evaluated.

The empirical model given by Yue et al.(2004) does not describe any reaction steps. A six constant kinetic model for coking kinetics was given by Wiehe (1993). This phase-separation kinetic model for coke formation, is described below.

For complex high boiling point hydrocarbons it is not possible to separate species by distillation (since species decompose at temperature below their boiling point). Hence such fluids are separated into pseudo-components by solvent fractionation. The fractions here are heptane solubles, toluene solubles, etc. Pitch is divided into heptane soluble and heptane insoluble. Coke (toluene insoluble) formation during the thermolysis of pitch occurs by a mechanism that involves the liquid – liquid phase separation of reacted asphaltenes from heptane solubles, and has many common features, Fig.2.13, which are stated below:

a) The figure shows the formation of coke as a function of reaction time for two reactants – heptane solubles and asphaltenes. There is an induction period which can be seen in the figure when no coke forms, after which it forms at a slow rate. This induction period is

the first common feature of pitch thermal conversion kinetics. It demonstrates that heptane solubles inhibit the formation of coke by the asphaltenes.

b) It can be seen that the asphaltene concentration increases from the initial concentration in the pitch to a maximum and then decreases. This maximum occurs at the same reaction time as the end of the coke-induction period. This maximum is the second common feature of pitch thermal conversion kinetics. It is a result of heptane solubles reacting to form asphaltenes which in turn react to form coke.

c) During the period coke is formed; the ratio of the asphaltene concentration to the concentration of heptane solubles approaches a constant. This approach to a constant ratio is common feature of pitch thermal conversion kinetics. It is suggested that this ratio is the solubility limit of the converted asphaltenes in the heptane solubles.

d) The fourth common feature of pitch thermal conversion kinetics is that the unconverted asphaltenes are actually the most thermally reactive fraction of the pitch but with the least extent of reaction.

A kinetic model by Wiehe describes these four features of pitch thermal conversion kinetics. It represents the conversion of asphaltenes over the entire conversion range and heptane solubles in the coke-induction period as first-order reactions. The coke formation is triggered by the phase separation of converted asphaltenes. The maximum solubility of these product asphaltenes is proportional to the total heptane solubles, and the decrease in asphaltenes parallels the decrease in heptane solubles. Finally, there is conversion of the insoluble product asphaltenes into toluene-insoluble coke. An infinite reaction rate for this coke formation reaction is used to show that this reaction rate is phase equilibrium controlled.

Thus, the coking of asphaltenes and whole pitch in the open reactor using the **series** model of Wiehe based on mass rather than moles is given as:

$$H^{+} \xrightarrow{k_H} b\,A^{+} + (1-b)V \tag{2.47}$$

$$A^{+} \xrightarrow{k_A} a\,A^{*} + d\,H^{*} + (1-a-d)V \tag{2.48}$$

$$A^{*}_{\max} = S_L\left(H^{+} + H^{*}\right) \tag{2.49}$$

$$A^*_{ex} = A^* - A^*_{\max} \tag{2.50}$$

$$A^*_{ex} \xrightarrow{\infty} TI \tag{2.51}$$

where a,b,d are stoichiometric coefficients; A^+, reactant asphaltenes; A^*, asphaltene cores; A^*_{max}, maximum asphaltene cores that can be held in solution; A^*_{ex}, excess asphaltene cores beyond what can be held in solution; H^+, reactant nonvolatile heptane solubles; H^*, product, nonvolatile heptane solubles; k_A, first-order reaction rate constant for reactant asphaltene thermolysis (min^{-1}); k_H, first-order reaction rate constant for the thermolysis of reactant heptane solubles (min^{-1}); S_L, solubility limit ($wt\%/wt\%$); TI, toluene-insoluble coke; and V, volatiles.

The derivation of the Wiehe kinetic model is given in Appendix III. From Fig.2.13, the points are the experimental data from Yue et al. (2004) and the solid line curves are fitted by using the yield of volatile, toluene insoluble, heptane soluble and asphaltene calculated from Eqs.(AIII.32), (AIII.37), (AIII-30) and (AIII-31), respectively. The kinetic model parameters for Athabasca pitch are given in Table 2.4.

The toluene insoluble yield by the experimental data, (Yue et al., 2004), as in Fig.2.14 is in agreement with Wiehe series model for 390°C but not for 400°C. The reason is that the parameters b, a, d and S_L will vary with temperature and they are not available for different temperatures.

So the simple coke formation model from +524°C fractions (pitch), given by Yue et al. (2004), Eqs.(2.44 - 2.46), is used in this work as the more complex Wiehe series model does not fit the toluene insoluble (coke) yield experimental results of Yue et al. (2004) for higher temperatures above 390°C.

The coke formation rate, m_c, in kg/s can therefore be calculated from the deposition flux of Eq.(2.25) as,

$$m_c = \phi_d * (\textit{area of the surface for deposit}) * TI * (\textit{mass of} + 524°C \textit{ in droplet}) \tag{2.52}$$

where the coke yield, TI is given by Eq.(2.46).

Table 2.4 Parameters of kinetic model for Athabasca Pitch at T = 390°C, Yue et.al. (2004):

k_A , rate constant for asphaltene, min^{-1}	0.0044
E_A , activation energy for asphaltene, *kcal/mol*	39
k_H , rate constant for heptane soluble, min^{-1}	0.0252
E_H , activation energy for heptane soluble, *kcal/mol*	54.6
b	0.925
a	0.277
d	0.077
S_L	1.658

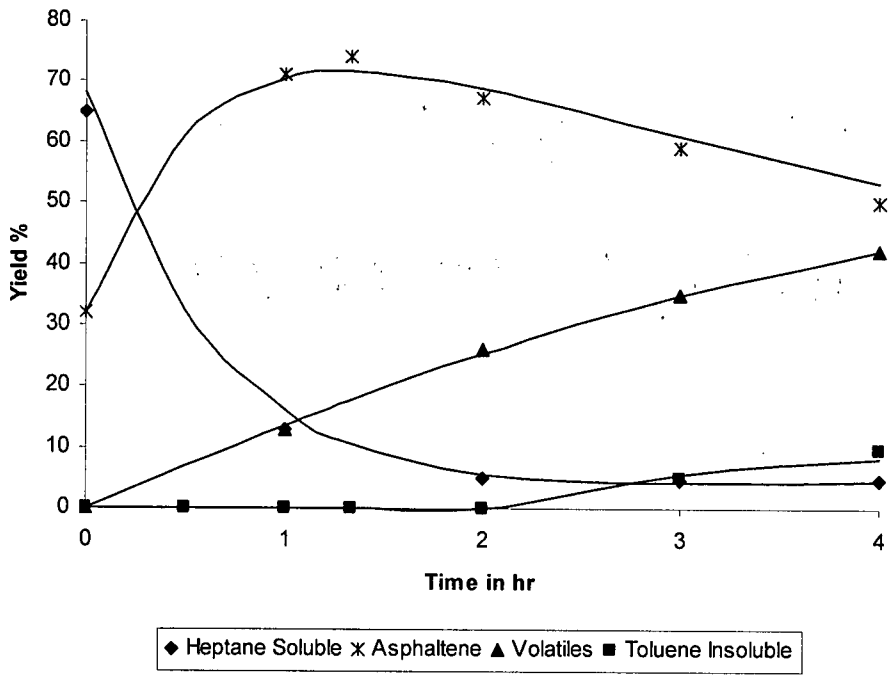

Figure 2.13 Yield (*gm/gm of +524°C*) % vs Time,hr @ 390°C of pitch (+524°C), Yue et al. (2004)

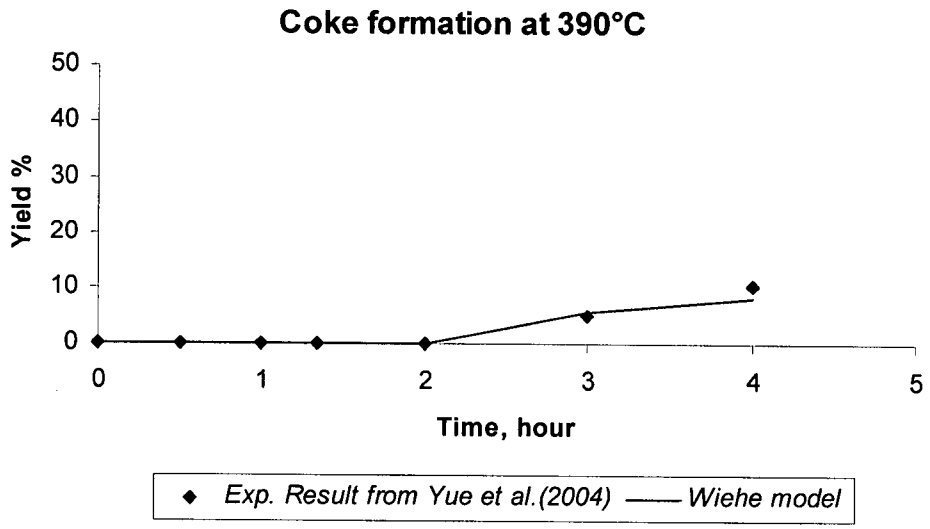

(a)

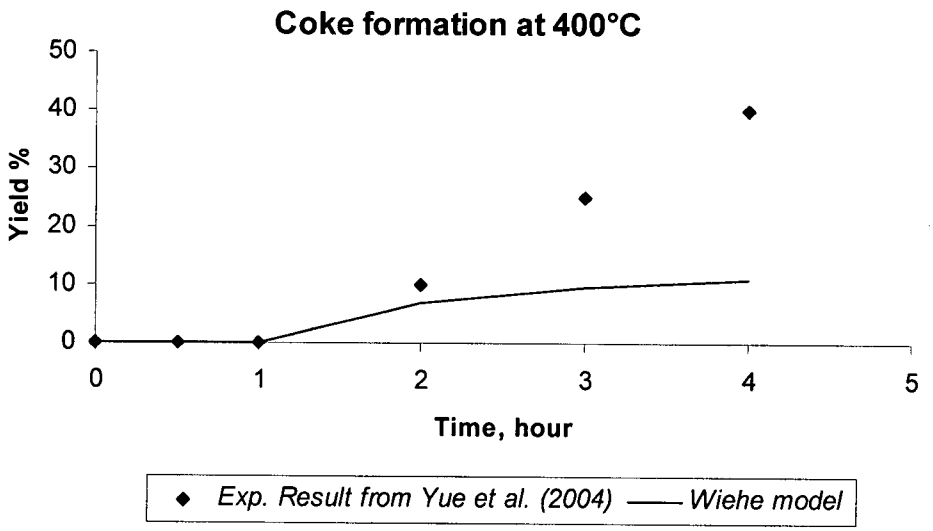

(b)

Figure 2.14 Toluene Insoluble yield for pitch at 390°C and 400°C

Chapter 3 : Base case simulation setup

3.1 Simulation setup for the base case

The base case for flow through the grid section in the scrubber was taken from the Jankovic (2005) base case. To simulate the change in pressure drop across the grid, the HYSYS 3.2 process simulator was used. Initially the lighter components were defined and then the property package to be used in the simulation. Hydrocarbon streams were installed and were characterized by the laboratory data. Then the unit operations used in the simulation were defined. These steps for setting up the simulation are described below.

3.2 Defining the lighter components and property package

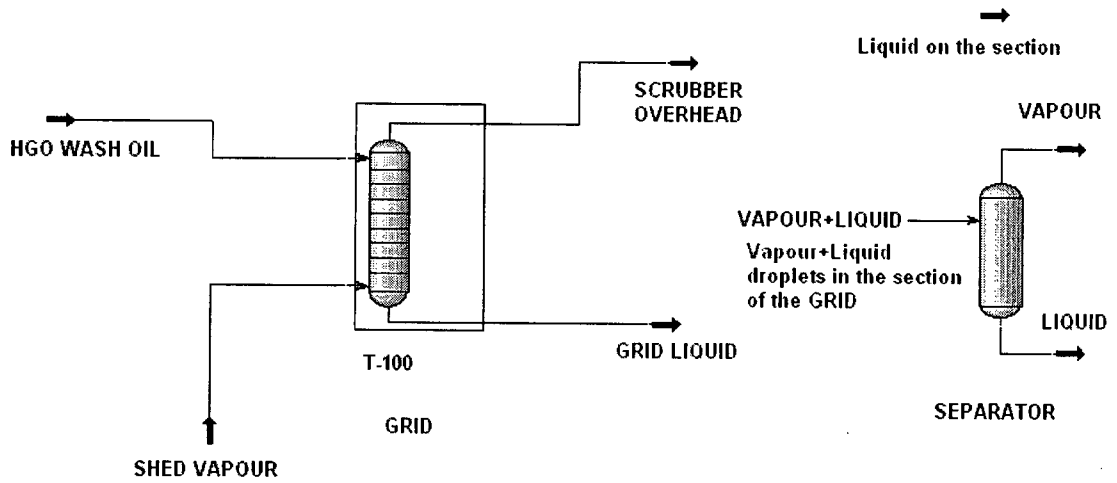

Figure 3.1 Simulation setup in HYSYS 3.2

Before the simulation is set up, components that have to be used in the simulation are defined. For this simulation only the light components, C1 to C4 and steam were selected. HGO wash oil and shed vapour are hydrocarbon streams which contain heavy fractions along with light fractions.

These heavy fractions were characterized based on laboratory assays (boiling curves, densities and viscosities), as done by Jankovic (2005).

The hydrocarbons are complex mixtures of huge numbers of components. It is impossible to know the composition of these mixtures since not all compounds are identified. Molecules can contain from 1 to more than 130 carbon atoms. So the heavy fractions are characterized using laboratory data. HYSYS accepts five types of standard laboratory data – true boiling point curve (TBP), ASTM D86 and ASTM D1160 distillation, ASTM D2887 simulated distillation, equilibrium flash vapourization (EFV) and chromatographic analysis. Appendix II gives the distillation curve for HGO wash oil and shed vapour. Data for HGO wash oil is ASTM D2887 distillation data provided by Syncrude Canada Ltd., and for shed vapour is ASTM D2887 distillation data generated by Jankovic (2005). Based on this input, HYSYS creates working curves for TBP, molecular weight, density and viscosity for the various fractions. The property package selected was the Peng-Robinson equation of state for vapour-liquid equilibrium calculations, as this equation of state is good for hydrocarbon systems.

3.3 Defining streams in simulation

In the scrubber, HGO wash oil is sprayed on the top of the grid and shed vapour enters the grid packing from the bottom. These streams are characterized in HYSYS 3.2 using the data given in Appendix II, which gives the laboratory distillation data for HGO wash oil and shed vapour. After these two streams were characterized, they were installed in the simulation environment shown in Fig.3.1. Other details for HGO wash oil and shed vapour flowrate, temperature and pressure are inputted in HYSYS from Table 3.1.

Other streams, scrubber overhead and grid liquid, were defined as empty streams in the flowsheet. These streams are connected to the grid packed bed tower, T-100, which is defined in the next section. They can be seen in Fig.3.1. HYSYS calculates the properties for the scrubber overhead and the grid liquid.

Table 3.1 Data for HGO wash oil and shed vapour from Jankovic (2005)

	HGO wash oil	Shed vapour
Flowrate , kg/s	44 (24kbpd)	242
Temperature, °C	325	404.9
Pressure, kPa	1480	218.6
Vapour fraction (wt. fraction)	0	0.97

3.4 Defining simulation blocks

In order to simulate the grid, a packed absorption column, T-100, in HYSYS was selected with a 1.4 m height and a 9.144 m diameter. A height of 1.4 m is selected as there are 20 sections of Koch-Glitsch FlexiGrid style#2 packing, each having a height of 70mm (Appendix I), in the industrial unit.

The bottom pressure to the column, which is the shed vapour pressure, and the number of sections were specified as 218.6 kPa and 20, respectively. After this step, the section efficiency of the column was specified. In HYSYS it is possible to select individual component efficiencies on each section of the column. As a default, the component efficiency of 100% is selected by HYSYS. In the base case considered by Jankovic (2005), the component efficiency for the +524°C components was 10^{-10}%, which is essentially zero. This was done in order to match the +524°C content of the scrubber overhead with industry data. This suggests that the heavy components are not getting scrubbed from the vapour by the wash oil. Hence, for this simulation the +524°C component efficiency in each section of the column was selected as 10^{-10}% and component efficiency for components having boiling points below 524°C was selected as 100%. It can be seen in Fig.3.2 that as the section efficiency of the +524°C hydrocarbons in the grid is decreased from 100% to 10^{-10}%, the temperature profile in the grid changes. As the +524°C hydrocarbon section efficiency in the grid decreases, the +524°C hydrocarbons wt% in the scrubber overhead increases, as can be seen in Table 3.1. To reach above 15% of +524°C in the overhead, the section efficiency must be below 0.001%.

Table 3.2 Weight percentage of +524°C hydrocarbons in the scrubber overhead for different grid section efficiencies for +524°C hydrocarbons

Grid section efficiency (%) for +524°C hydrocarbons	+524°C hydrocarbons (wt%) in the scrubber overhead
10^{-10}	15.563
10^{-5}	15.56
10^{-3}	15.34
1	13.55
10	6.735
50	3.173
100	2.568

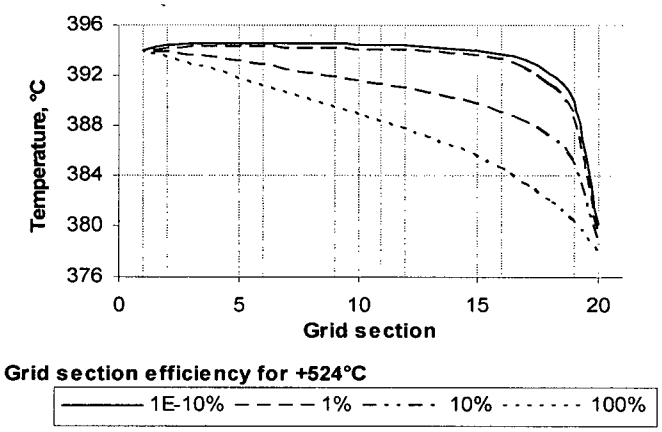

Figure 3.2 Temperature profile in the grid for different grid section efficiency for +524°C hydrocarbons

3.5 Defining the separator unit in the simulation

The shed vapour entering the grid packing and vapour streams in each of the grid sections of the packing contain some liquid phase. HYSYS does not provide information about how much liquid phase there is in the vapour stream coming from each section of the grid packing. To know how much liquid phase is present in the vapour stream, a separate unit block called SEPARATOR

was defined in the simulation (Fig.3.1). Here the VAPOUR+LIQUID stream is the inlet stream to the SEPARATOR and VAPOUR and LIQUID are the outlet streams from the SEPARATOR. When the simulation runs, it takes the properties of the vapour stream from each section of the column and copies them into the stream VAPOUR+LIQUID. SEPARATOR separates vapour from liquid and their respective properties were taken for further calculation of coke deposition on the packing.

Table 3.3 Details of grid section in the scrubber[a]

Type of the packing	**Koch-Glitsch FlexiGrid style#2**
Number of sections	20
Height	1.4 m (4.6 ft)
Diameter	9.144 m (30 ft)
Shed vapour inlet pressure, SOR	218.6 kPa (17 psig)

Note a: Data given by Syncrude.

3.6 Defining the spreadsheet in the simulation

As coke deposits on the surface of the packing, the pressure drop in each section of the grid increases at a fixed throughput. A spreadsheet was used to incorporate the change in pressure in the section due to the increase in pressure drop. A spreadsheet is a tool in HYSYS that has cells arranged in a matrix. Arithmetic calculations can be done in these cells which can be connected to the variables in the streams, unit blocks, etc. defined in the simulation environment. Fig 3.2 shows the spreadsheet used in this simulation. Column A and rows from 2 to 21 in the spreadsheet give the number of sections in the grid, T-100, column B and rows from 2 to 21 show the pressure drop in each section having units as mbar, and column C and rows from 2 to 21 give pressure in the section of column T-100 in units of kPa. The pressures shown in column C, rows 2 to 21, are copied into column D, rows 2 to 21. Each cell in column D, rows 2 to 21 of the spreadsheet, is linked to the pressure in each section of the column, T-100. Fig 3.2 shows the pressure profile of the column, T-100, where the cells from the spreadsheet are linked. The linking of the spreadsheet is done so as to incorporate the change in pressure in each section of the grid, T-100, for every unit time defined in the simulation. This is because the accumulation

of coke on the surface increases the pressure drop across each section of the column, T-100. So this linking of the spreadsheet changes the pressure in each section of the column T-100 *quickly*. As the pressure changes in the section, the properties of the vapour stream coming from the section are recalculated by HYSYS.

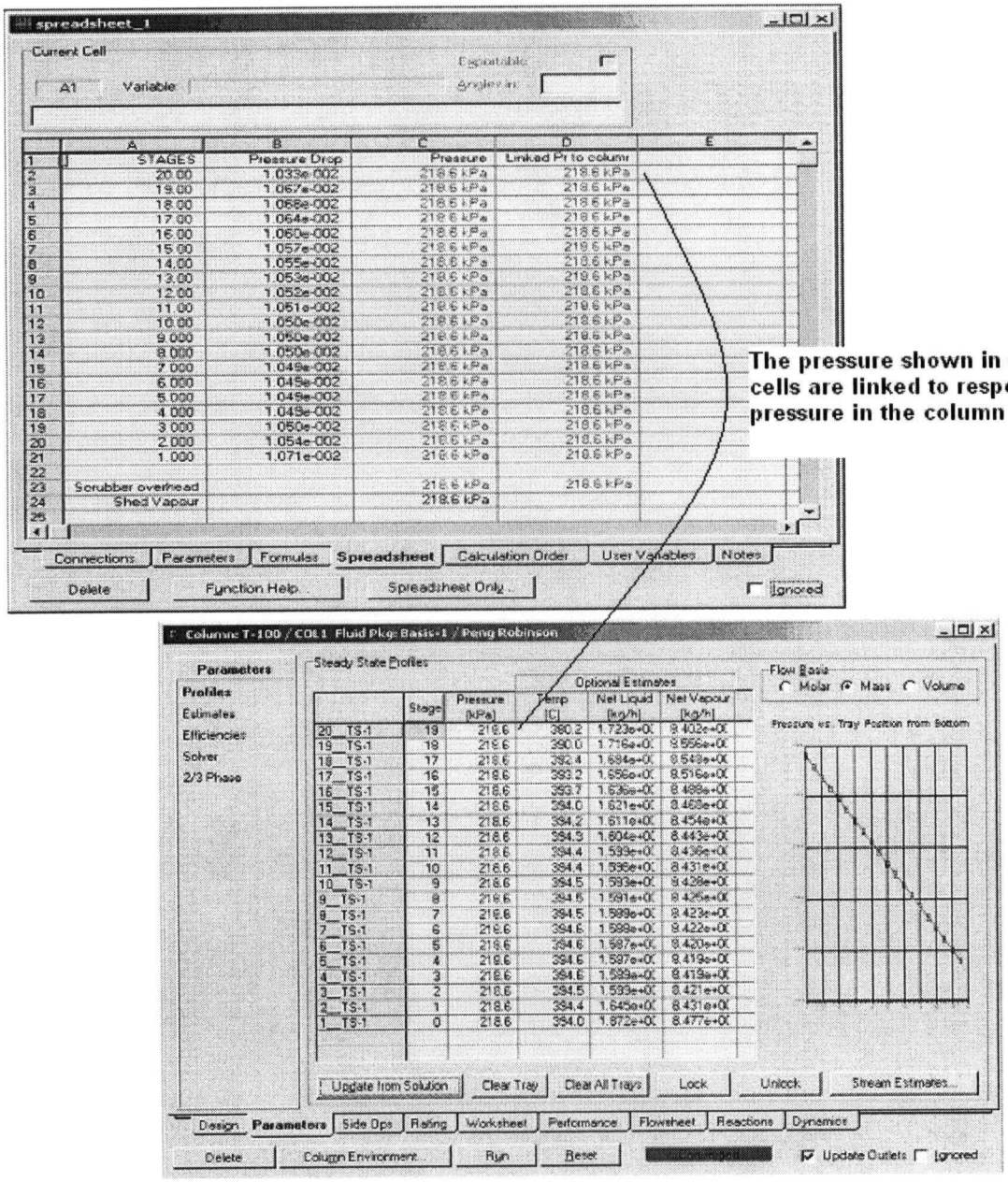

Figure 3.3 The spreadsheet defined in HYSYS shows the connectivity with pressure in column, T-100

3.7 Base case

It is assumed that the liquid phase in the vapour stream coming from each section is in the form of droplets. Liquid droplets get transported to the surface of the packing by the mechanisms of diffusion and inertia. Some of these droplets stick on the surface of the packing and undergo reactions to form coke. As discussed previously, the heavy component, +524°C, in the liquid droplets takes part in the coking reaction. The pressure drop across the grid after a year of operation is around 1" H_2O (Syncrude Canada Ltd.). Based on this pressure drop of 1" H_2O across the grid, the total amount of coke deposited in the grid is around 33,800 kg.

3.8 Assumptions for the base case

1) Liquid droplets in the vapour stream are spherical in shape and are uniformly distributed in the vapour phase.
2) The droplet sizes considered were 0.1, 0.2, 0.5, 1, 3, 5, 8 and 11 μm with equal weight fraction.
3) Shed vapour is uniformly distributed radially before entering the grid.
4) HGO wash oil is uniformly distributed radially at the top of the grid.
5) Vapour and liquid are assumed to be mixed before entering each section of the grid packing.
6) The temperature is uniform in each section of the grid packed bed.
7) The packing surface temperature is the same as the temperature of the grid section.
8) Density of coke is 1400 kg/m^3.
9) The inlet pressure to the grid packed bed is constant at 218.6 kPa (17 psig).
10) The droplets do not dissolve and lose their characteristics in the wash oil.
11) The droplets do not get washed away by the wash oil.
12) The wetability fraction of packing is 0.9 which means that the packing is 90% wetted by HGO wash oil and 10 % of the packing is dry.

3.9 Algorithm for simulating the fouling process in the grid.

The grid has a complex geometry, as explained in Chapter 1. For simulating the fouling process in the grid, a part of the blade which is symmetric has to be considered. The part of the blade shown in Fig.3.4 was considered for the calculation of the coke deposit. The part shown in Fig.3.4 was divided into three sub-parts. One of the sub-parts is rectangular and the other two are not rectangular. So the other two sub-parts were considered to be composed of 50 small flat rectangular plates, as can be seen in the Fig.3.4.

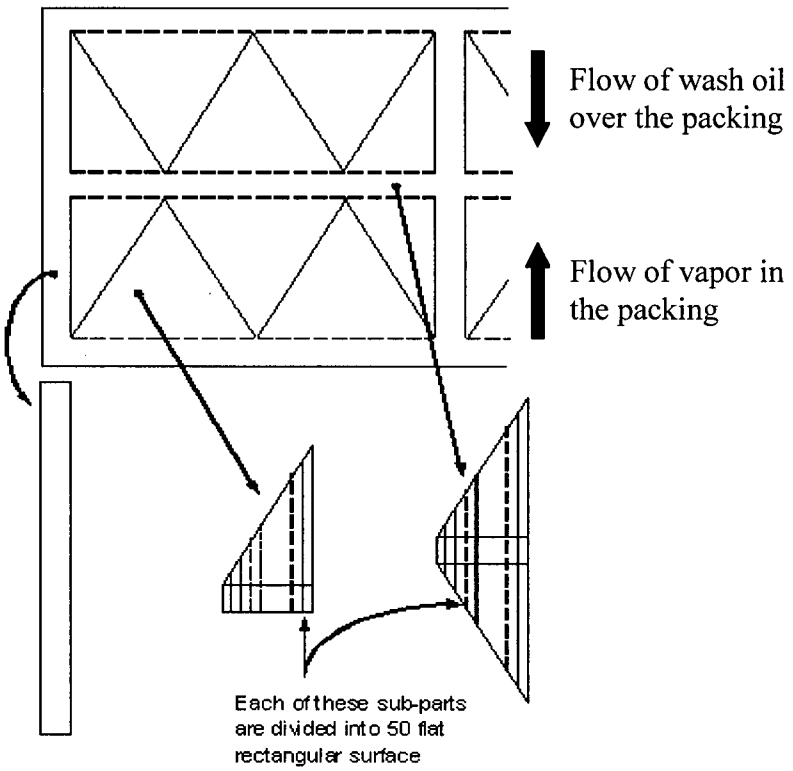

Figure 3.4 Sub-parts of a blade are divided into many flat rectangular plates

As the simulation starts, the properties of the vapour and liquid phases are calculated by HYSYS. The mass of coke was calculated, based on the models given in Chapter 2, on each of these flat rectangular plates. Summing up the total coke formed in these flat rectangular plates, the total

mass of coke in a given time period was calculated in a blade of an element and then in the entire section. Then the change in voidage and specific surface area of the grid section were calculated based on the procedure described in Appendix I. The coke thickness was calculated by knowing the mass of coke in the grid section, Fig.3.5. As the coke deposit thickness increases the voidage of the packing decreases and specific surface area of the packing increases. So after calculating the coke thickness, the voidage, Fig.3.6, and the specific surface area, Fig.3.7, of the grid section were calculated. As a result the pressure drop across the section increased. Fig.3.8 shows how the calculations were done for the entire grid.

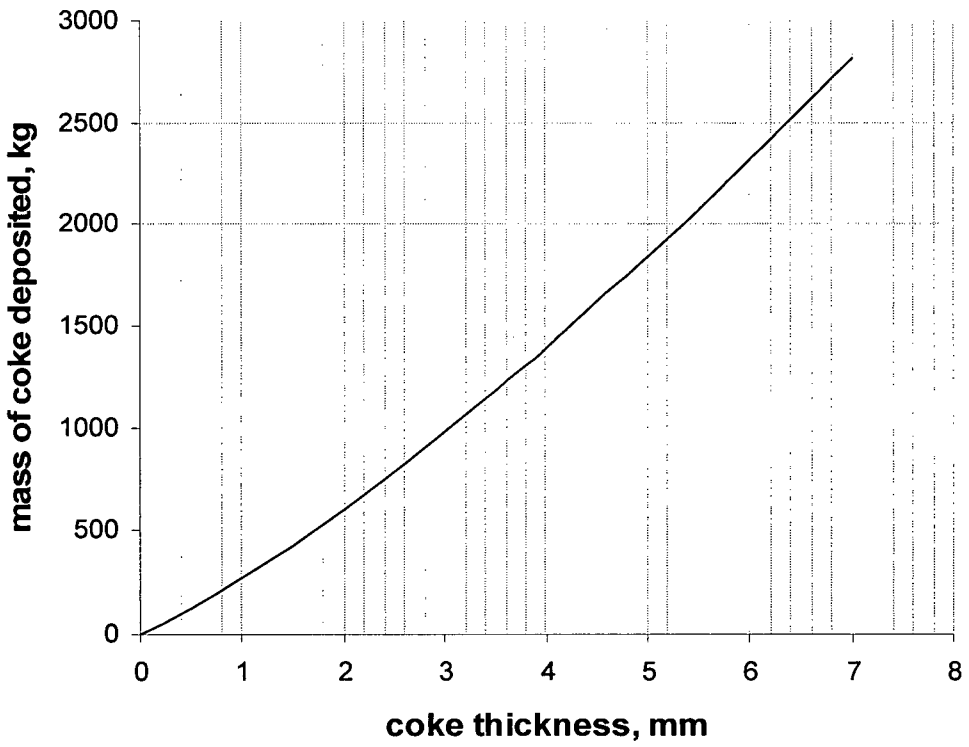

Figure 3.5 Mass of coke deposited in a single section for different coke thicknesses

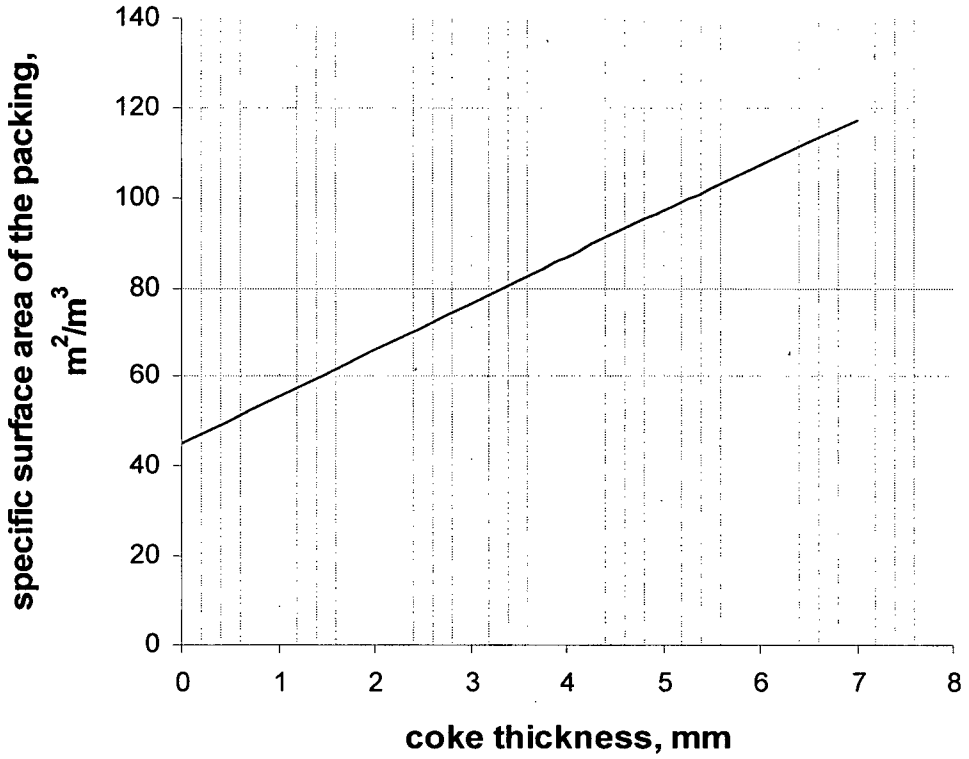

Figure 3.6 Specific surface area of the grid in a single section for different coke thicknesses

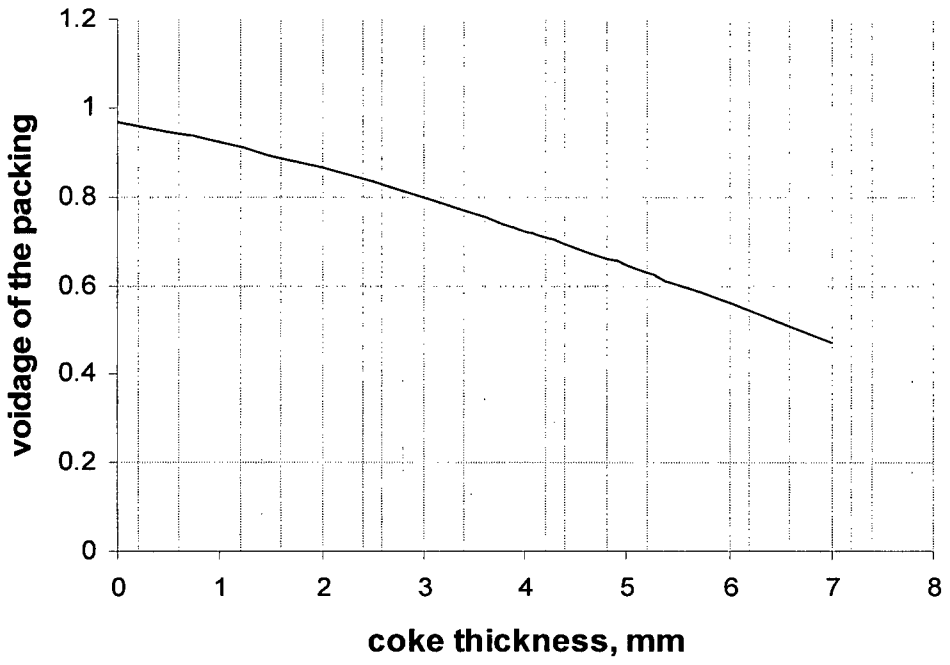

Figure 3.7 Voidage of the packing in a single section for different coke thicknesses

Properties of vapour and liquid on each section of the grid determined from HYSYS

E and k" defined from the user

Calculate the clean pressure drop in each section of the grid using BRF model, ***Eq.(2.22)***

For ***time*** *from 0 to 8640 hr* // *duration of one year (8640 hr) operation*

For ***section*** *from 1 to 20* // *total sections in the grid is 20*

For ***droplet_size*** *= { 0.1, 0.2, 0.5, 1, 3, 5, 8, 11 microns}*

Estimate the properties of the vapour and liquid in vapour stream in grid section using SEPARATOR ***(Fig.3.1)***

For ***sub_parts*** *from 1 to 50*

Calculate the amount of liquid droplets transported and adhered on the surface of the packing using ***Eqs.(2.32) - (2.43)*** *separately for sub_parts 1, 2 and 3* ***(Fig.3.4)***

End For loop for ***sub_parts***

End For loop for ***droplet_size***

Calculate the amount of the +524°C components from the droplets adhered on the surface separately for all the three sub_parts 1, 2 and 3 ***(Fig.3.4).***

Calculate the amount of coke produced from +524°C components in the droplets by ***Eq. (2.46)*** *for droplets in sub_part 1, 2 and 3* ***(Fig.3.4).***

Calculate the change in voidage ***(Fig.3.6)*** *and specific surface area* ***(Fig.3.7)*** *of the grid section due to coke deposit on the grid surface.*

Calculate the pressure drop in the section using BRF model using ***Eq.(2.22)*** *.*

End For loop for ***section***

Update the pressure of each section in HYSYS spread sheet, which updates the section pressure in the grid.

time = time + 10 hr

End For loop for ***time***

Print Results*: Profiles of : Mass of coke, voidage, specific surface area of grid, thickness of coke on the and pressure drop in the grid for every month*

Figure 3.8 Algorithm for fouling process simulation

Chapter 4: Base case and case studies -- Results and discussions

Case studies were done to compare the coke deposit build-up and pressure drop increase across the grid for the base case, with changes in wetted fraction of the grid packing, droplet diameter in the grid vapour, and temperature and flow rate of HGO wash oil. Other process variables were kept constant. Initially, the profiles of coke deposition and pressure drop across the grid for the base case condition were studied.

4.1 Base case

The pressure drop profile in the grid is governed by the flowrates and properties of the grid vapour and wash oil and also the mass of coke deposited in the grid. The mass of the coke deposit depends on the mass of droplets stuck on the grid surface. The droplets contain +524°C hydrocarbons which are the precursors of the coke deposit, as explained in Chapter 2. The mass deposition flux, ϕ_d, is the product of the deposition coefficient, k_d, and the bulk concentration of the droplets, c_b, Eq.(2.24). It is calculated for the dry surfaces via Eq.(2.31), $\phi_d = c_b / (1 / k_{tg} + 1 / k_a)$ and for the wet surfaces via Eq.(2.30), $\phi_d = c_b / (1 / k_{tg} + 1 / k_{tl} + 1 / k_a)$. The resistance due to liquid film on the grid surface is considered as negligible and equilibrium constant, K, is taken as unity in this work. The attachment coefficient, k_a, is affected by the temperature in the grid, Eq.(2.43).

Fig.4.1(a) shows the temperature profile of the grid. The temperature remains uniform throughout most of the grid at around 394°C, but drops by 14°C at the top of the grid (20^{th} section) because of the cooling effect of the HGO wash oil which is sprayed onto the grid at 325°C. Fig.4.1(b) shows the pressure drop profile of the grid at the clean (SOR) condition. The flowrates and properties of the vapour (including droplets) and liquid which are shown in Fig.4.1(h)-(m) are used to calculate the pressure drop in each section. Their profiles are dependent on the grid temperature profile. Based on the temperatures, the profiles of flowrate and the properties of the vapour+droplet stream and the wash oil can be explained. In Table 4.1,

the flowrate of vapour+droplet is shown to be almost constant along the grid at around 234 kg/s. But, the droplet flowrate at the top at 57 kg/s is higher by around 6% when compared with the value at the mid-section of the grid (54 kg/s). The vapour flowrate is lower by around 2.5% at the top than in the mid-sections of the grid. It is seen that as the temperature of the grid decreases the vapour flowrate decreases and the droplet flowrate increases and vice versa. As temperature decreases, some vapour components condense so the vapour flowrate decreases and the droplet flowrate in the vapour increases. As HGO wash oil enters the grid from the top, the wash oil flowrate decreases by 2.6 kg/s at the 15^{th} section from 44 kg/s at the top and then remains constant at 40 kg/s to the bottom of the grid. As the grid temperature increases the wash oil flowrate in the grid decreases and vice versa. This is because some of the wash oil vapourizes when temperature increases. The density of vapour in grid remains constant at around 3.14 kg/m^3 and increases by about 2% at the top of the grid when compared with that of the mid-sections of the grid. The density of wash oil remains almost constant at 702 kg/m^3 in the grid but increases by 2% at the top of the grid, due largely to temperature effects. Here the density of the vapour+droplet and the wash oil increases when the temperature decreases and vice versa. The viscosity of the grid vapour remains constant at 0.024 cP but decreases by 4% at the top of the grid. The viscosity of the grid vapour decreases as the temperature in the grid decreases and vice versa. The viscosity of the wash oil remains constant at about 0.86 cP and increases by 25% at the top of the grid. The viscosity of the wash oil decreases as the temperature of the grid increases and vice versa. Based on the flowrates and properties of the grid vapour and wash oil in the grid section, the pressure drop in the grid section is evaluated at the start of run (SOR) and is given in Table 4.1.

At the end of run (EOR) condition the temperature profile in the grid is essentially the same as that of the start of run (SOR) condition, and the difference for each grid section is between $\pm 0.013°C$. The flowrates and properties of the grid vapour and wash oil are dependent on the grid temperature. So at the EOR condition there is hardly any change in grid vapour and wash oil properties and flowrates, but there is a slight change in grid vapour density, which is about 0.01% lower than that of the SOR condition. This is due to a decrease in the grid section pressure at the EOR condition. The decrease in the pressure in the grid section was due to increase in pressure drop in the section with time. Therefore the changes in pressure drop from SOR to EOR

due to flowrates and properties of the grid vapour and wash oil are negligible. The change in pressure drop in the grid is due to the coke deposit in the grid.

One of the governing factors for the mass of coke deposited in the grid is the bulk concentration of the droplets in the grid vapour, c_b. Fig. 4.1 (c) shows c_b in the vapour within the grid section for the SOR condition. Here c_b is greater at both the top and bottom of the grid as compared to its value at the mid-sections of the grid. At the top of the grid (20^{th} section), c_b is 0.776 kg/m^3, then c_b decreases to 0.716 kg/m^3 at the 3^{rd} section and then increases to 0.741 kg/m^3 at the bottom of the grid, Table 4.1. Under isothermal conditions, c_b would decrease from the bottom to the top of the grid. We see that c_b is higher where the grid temperature is lower, so more grid vapour is being condensed, and more droplets are formed in the vapour, particularly at the top.

As discussed in Chapter 3, based on the temperature profile of the grid, there are +524°C hydrocarbons in the droplets in the grid vapour. The higher the mass flowrate of +524°C hydrocarbons in the droplets, the higher is the coke yield at any specific condition. Fig.4.1(d) gives the mass flowrate of the +524°C hydrocarbons present in droplets which are in vapour from each grid section at SOR. These data were generated by HYSYS. It can be seen that the mass flowrate of +524°C hydrocarbons in the droplets is greater at the top and bottom of the grid than at the mid-sections of the grid. The mass flowrate of +524°C hydrocarbons in the droplets at the top of the grid (20^{th} section) is 10% higher than that of mid-sections of the grid (around 27.6 kg/s).

At the EOR the change in bulk concentration of the droplets in the vapour, c_b, is small when compared with the SOR condition. The difference in c_b at the SOR condition for each grid section is between ± 1.2% when compared with EOR condition. Similarly, the mass flowrate of +524°C hydrocarbons in the droplets is nearly the same for both the SOR and EOR conditions, Fig.4.1(c)-(d). This slight difference in c_b from SOR to EOR has a negligible effect on increase of the mass deposition flux for the droplets, ϕ_d, at the EOR condition.

The pressure drop across the grid is around 2.5 mbar (1" H_2O) after the EOR, 12 months of operation, (data given by Syncrude). At this condition the adjustable parameters E and k'' in the attachment coefficient, k_a, as defined in Eq.(2.43), were evaluated. As described in Chapter 2,

two different conditions were considered for deposition of droplets on the surface: one for a weakly (lower value of E) and other for a strongly (higher value of E) temperature-dependent adhesion rate. The calculations were done for these two extremes, i.e. E = 5 and 75 kcal/mol. The values of k'' calculated were 2.8 x 10^{-2} s^2/m for E = 5 kcal/mol and 3.05 x 10^{-25} s^2/m for E = 75 kcal/mol, respectively. As seen earlier, the temperature profile in the grid is not uniform, thus for the two values of E, two different profiles of coke build-up within the grid are evident. The pressure drop increase was the same, however, for each case.

Table 4.1 Profile in the grid at SOR condition

	Grid section			
	1st	3rd	15th	20th
Temperature, °C	394	394.4	394.2	380.1
Flowrate, kg/s				
Grid vapour (Vapour+droplet)	235 (180 + 54)	234 (180.2 + 53.6)	234.5 (180 + 54.4)	233 (176.3 +57)
Wash oil	41.5	39.9	41.3	43.9
Density, kg/m^3				
Grid vapour	3.14	3.12	3.14	3.2
Wash oil	702	702	702	715.4
Viscosity, cP				
Grid vapour	0.02377	0.02379	0.02377	0.02289
Wash oil	0.87	0.87	0.83	1.08
Pressure drop, mbar	$9.53x10^{-3}$	$9.43x10^{-3}$	$9.52x10^{-3}$	$9.72x10^{-3}$
Bulk concentration, c_b, kg/m^3	0.741	0.716	0.727	0.776
+524°C hydrocarbons in the droplets, kg/s	27.9	27.6	27.7	30.3

At the EOR the change in bulk concentration of the droplets in the vapour, c_b, is small when compared with the SOR condition. The difference in c_b at the SOR condition for each grid section is between ± 1.2% when compared with the EOR condition. Similarly, the mass flowrate of +524°C hydrocarbons in the droplets is nearly the same for both the SOR and EOR conditions, Fig.4.1(c)-(d). This slight difference in c_b from SOR to EOR has a negligible effect on increase of the mass deposition flux for the droplets, ϕ_d, at the EOR condition.

In this study, eight different droplet sizes were considered with 0.1 μm as the smallest and 11 μm as the largest (based on the cyclone cut point). Some of these droplets fall in the diffusion transport regime and others fall in the inertia transport regime. In Eq.(2.40), the dimensionless droplet relaxation time, t_d^+, dictates the regime of droplet transport to the surface of the packing. When $t_d^+ < 0.2$, the droplet is in the diffusion transport regime. It can be seen in Table 4.2 that all droplets in the wash oil film fall in diffusion transport regime. But with a dry surface, droplets with diameters 0.1 to 5 μm are in the diffusion and 8 to 11 μm are in the inertia transport regimes. When droplets with diameters 8 to 11 μm move to the surface from the vapour via the wash oil liquid film, their transport is by diffusion towards the surface. This is because the viscosity of the wash oil is higher than that of vapour. As the wash oil flowrate remains constant at both the SOR and EOR conditions, t_d^+ for droplets in the wash oil is constant. But, t_d^+ for droplets in the grid vapour is higher in the EOR than in the SOR condition, since the grid vapour velocity is higher at EOR than at SOR. It can be seen from Table 4.2 that for 0.1 to 0.5 μm droplet diameters, the mass transfer coefficient of the droplet in the wash oil, k_{ml}, is lower by a factor of 6 when compared with the mass transfer coefficient of droplet in the vapour, k_{mg}. For the 8 μm droplet diameter, k_{ml} is less by a factor of 60 when compared with the transport coefficient of the droplet in vapour, k_{tg}. For the 11 μm droplet diameter, k_{ml} is lower by 3 orders of magnitude when compared with k_{tg}. So the mass transfer deposition of the droplet on the wetted surface will be lower than that of the dry surface.

For E = 5 kcal/mol (a temperature insensitive adhesion rate), the mass of the coke deposited in each grid section is nearly constant at 1700 kg, but is slightly higher at the top of the grid, i.e. 1770 kg, as can be seen in Fig.4.1(e). The mass of coke deposited on the surface is calculated from the mass of droplets stuck on the surface. In the grid, the packing surface is assumed to be 90% wetted by the wash oil. As said before, the droplets in the wash oil film are transported to the surface via diffusion. Table 4.2(a) shows the mass transfer coefficient of the droplets in the film, k_{ml}, throughout the grid, and Table 4.2(b) shows the attachment coefficient, k_a, for the droplets on the wetted and on the dry surface. As we proceed from SOR to EOR, the change in mass transfer coefficient of the droplets in the film, k_{ml}, and the attachment coefficient, k_a, for the droplet on wetted surface is negligible. So ϕ_d for the droplets on the wetted surface remains almost constant from SOR to EOR. But, the velocity of vapour in the grid increases, due to the decrease in grid voidage from 0.97 (under clean conditions) caused by the coke deposit.

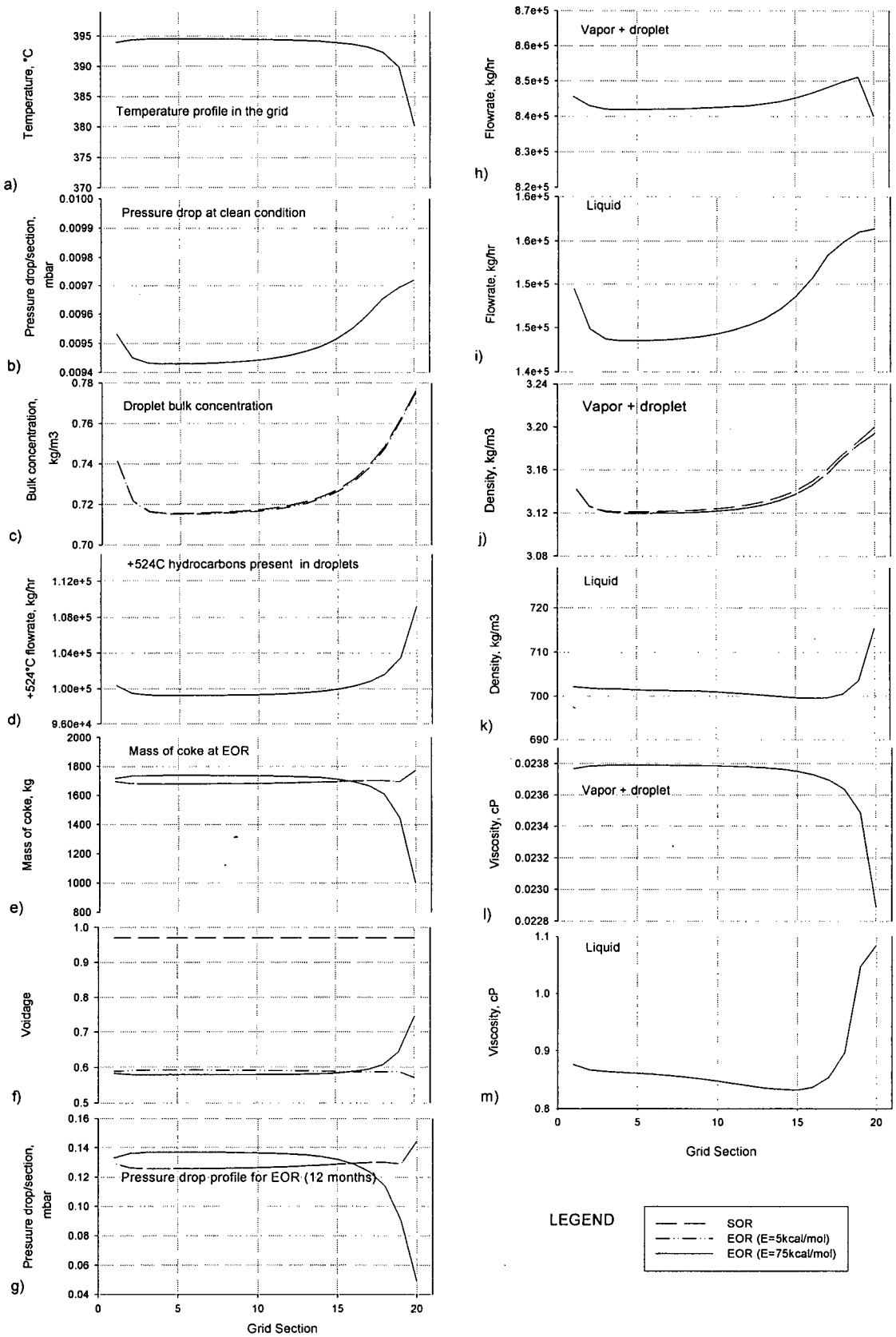

Figure 4.1 Profile of grid for base case

Table 4.2(a) and (b) Mass transfer, transport and attachment coefficients of droplets at SOR and EOR conditions

(a)

d_d, μm	t_d^+ in wash oil	k_{ml}, m/s	t_d^+, in grid vapour at **SOR**	k_{mg} (0.1 – 5μm), k_t (8-11μm), m/s at **SOR**	t_d^+, in grid vapour at **EOR**	k_{mg} (0.1 – 5μm), k_t (8-11μm), m/s at **EOR**
0.1	$7x10^{-7}$	$1.5x10^{-6}$	$1.4x10^{-5}$	$9.3x10^{-6}$	$3.3x10^{-5}$	$1x10^{-5}$
0.2	$2.8x10^{-6}$	$9x10^{-7}$	$5.7x10^{-5}$	$6.2x10^{-6}$	$1.3x10^{-4}$	$6.5x10^{-6}$
0.5	$1.7x10^{-5}$	$5x10^{-7}$	$3.6x10^{-4}$	$3.4x10^{-6}$	$8.3x10^{-4}$	$3.6x10^{-6}$
1	$7x10^{-5}$	$3x10^{-7}$	$1.43x10^{-3}$	$2.1x10^{-6}$	$3.3x10^{-3}$	$2.2x10^{-6}$
3	$6.5x10^{-3}$	$1.5x10^{-7}$	$1.3x10^{-2}$	$9.5x10^{-7}$	$3x10^{-2}$	$1x10^{-6}$
5	$1.8x10^{-3}$	$1x10^{-7}$	$4.9x10^{-2}$	$7.1x10^{-7}$	$9.4x10^{-2}$	$7.5x10^{-7}$
8	$4.6x10^{-3}$	$8x10^{-8}$	0.21	$5x10^{-6}$	0.3	$6x10^{-6}$
11	$9x10^{-3}$	$6x10^{-8}$	0.43	$1.8x10^{-5}$	0.61	$2.2x10^{-5}$

(b)

	k_a, m/s		
	Wetted surface	**Dry surface**	
	Same for both SOR and EOR	**SOR**	**EOR**
20^{th} section (top of the grid)	0.00018	0.0002	0.0001
1^{st} – 15^{th} sections	~ 0.0005	~ 0.0009	~ 0.0004

So both the mass transfer coefficient of the droplets in vapour, k_{mg}, and the transport coefficient, k_{tg}, increase (because the friction velocity u^* increases on the dry surface and k_{tg} is proportional to $(u^*)^5$, Eq.(2.42)).

It should be noted that the increase in mass transfer coefficient for the droplet in the vapour, k_{mg}, from the SOR to EOR condition is around 7%. But the transport coefficient of the droplets, k_{tg}, increases around 20%, Table 4.2(a). In the grid, the decrease in the attachment coefficient, k_a, for the droplet on the dry surface from the SOR to the EOR condition is around 56%, Table 4.2(b). The droplet attachment coefficient, k_a, on the dry surface reduces at the EOR condition as k_a is inversely proportional to u^*, Eq:(2.43). So from SOR to EOR, ϕ_d is increasing on the dry surface. The mass transfer coefficients, k_{mg} and k_{ml}, and transport coefficient, k_{tg}, are controlling the increase of ϕ_d, rather than the attachment coefficient, k_a, because k_a is very large when

compared to k_{mg} and k_{ml}, Table 4.2. Based on these mass transfer, transport and attachment coefficients as well as the bulk concentration of droplets in the grid section, the total mass deposition flux of the droplets depositing on the surface, ϕ_d, is calculated. From Table 4.1 and Table 4.3 it can be seen that when temperature decreases in the grid section, the bulk concentration of the droplets increases and also the mass deposition flux for droplets increases. So for weakly temperature dependent adhesion of droplets, E = 5 kcal/mol, the mass deposition flux of droplets on the surface is more dependent on the bulk concentration of the droplets in the grid vapour. The higher the mass deposition flux of the droplets, the higher is the mass of coke deposit. Hence at the top of the grid the mass of the coke is higher than at the mid-sections of the grid, Table 4.3.

Table 4.3 Mass deposition flux and mass of coke deposited in the grid at both E = 5 and 75 kcal/mol

	Grid section			
	1st	**3rd**	**15th**	**20th**
Temperature in the grid, °C	394	394.4	394.2	380.1
E = 5 kcal/mol				
ϕ_d, SOR, kg/m^2 s	2.3×10^{-6}	2.3×10^{-6}	2.31×10^{-6}	2.42×10^{-6}
ϕ_d, EOR, kg/m^2 s	2.66×10^{-6}	2.63×10^{-6}	2.66×10^{-6}	2.81×10^{-6}
Mass of coke, kg	1697	1678	1695	1772
E = 75 kcal/mol				
ϕ_d, SOR, kg/m^2 s	2.31×10^{-6}	2.34×10^{-6}	2.3×10^{-6}	1.42×10^{-6}
ϕ_d, EOR, kg/m^2 s	2.69×10^{-6}	2.73×10^{-6}	2.68×10^{-6}	1.59×10^{-6}
Mass of coke, kg	1718	1736	1712	999

In contrast to the case for E = 5 kcal/mol, at E = 75 kcal/mol (a highly temperature sensitive adhesion rate) the mass of coke deposited in the grid is nearly constant at around 1740 kg in the mid-sections of the grid and drops markedly to 999 kg at the top of the grid (20th section), as can be seen in Fig.4.1(e). In Table 4.3, it can be seen that ϕ_d at the EOR is also higher than at the SOR condition. It is also seen that as the temperature increases the total mass deposition flux for droplets, ϕ_d, increases and vice versa (Table 4.3). The attachment coefficient, k_a, also decreases with temperature. For the wetted surface, k_a is 0.00018 m/s at the top of the grid and 0.0005 m/s

at the mid-sections of the grid where temperature is higher. For the dry surface, k_a is 0.0001 m/s at the top of the grid where the temperature is lowest and 0.0004 m/s at the mid-sections of the grid. At the top of the grid, the overall deposition coefficient, k_d, decreases, as the attachment coefficient of the droplet, k_a, to the surface decreases (the mass transfer coefficient of the droplet is nearly constant through out the grid). But, the bulk concentration of droplets, c_b, is higher at the top of the grid section than in the mid-sections of the grid, Table 4.1. It is seen that the mass deposition flux of the droplets at the top of the grid is lower than that of the mid-sections of the grid by 40%, Table 4.3, i.e. the deposition flux decreases at the top in spite of the increased value of c_b. Here for higher values of E, k_a is the controlling factor for total mass deposition flux for droplets, ϕ_d, whereas for lower values of E, the bulk concentration of droplets, c_b, is the dominant factor.

As the coke deposits on the grid, the voidage of the grid decreases. At the EOR condition for E = 5 kcal/mol, the voidage in the grid is uniform axially and is approximately 0.66. For E = 75 kcal/mol the voidage of the grid section in the 1st, 3rd and 15th sections is approximately 0.65 and for 20th section the voidage is 0.81 because the mass of coke deposited is less at the top of the grid. The voidage in the grid at the EOR condition can be seen in Fig.4.1(f).

Similarly, the pressure drop in the grid section at the EOR is evaluated at both E = 5 and 75 kcal/mol, Fig.4.1(g). For E = 5 kcal/mol, the pressure drop in the 1st, 3rd and 15th section is approximately 0.125 mbar and on 20th section the pressure drop is 0.14 mbar, due to slightly more coke deposit at the top of the grid. For E = 75 kcal/mol the pressure drop in the 1st, 3rd and 15th section is approximately 0.135 mbar but at 20th section the pressure drop is 0.05 mbar, due to less coke deposit.

Though for both weak and strong temperature dependent adhesion of droplets on the surface the mass of coke deposited in each section is different, the total mass of coke deposited in the grid and the total pressure drop across the grid at the EOR are identical as explained previously. The time dependence of the total coke deposited and the pressure drop increase in the grid are shown in Fig.4.2(a) and (b).

In Fig.4.2(a) the mass of coke deposited appears to be linear with time; however this is not so because of the slight increase in total mass deposition flux for droplets with time. It was shown previously that the mass deposition flux for droplets, ϕ_d, is greater at the EOR than at the SOR conditions. The pressure drop (Fig.4.2(b)) is highly non-linear (because the pressure drop per unit height of grid is proportional to ε^{-3} and a_p of the grid), with a much more rapid increase after the first six months.

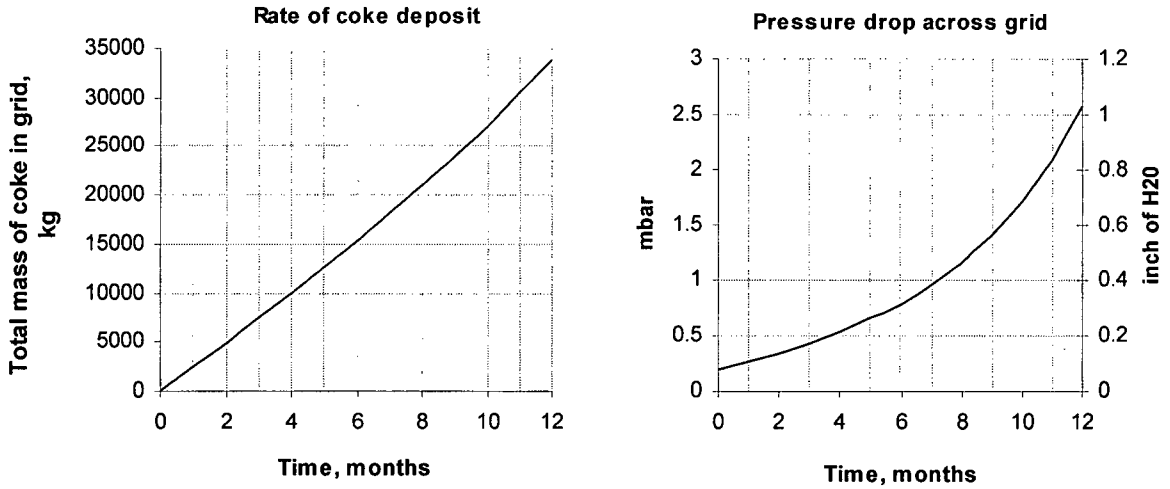

(a) (b)

Figure 4.2 (a) and (b) Rates of mass of coke deposited and pressure drop change in grid at EOR condition.

4.2 Effect of wettability of grid

As stated in the previous section, when a surface is wetted there is an extra resistance to mass transfer. Hence, the wettability fraction will influence the build-up of coke on the surface. Wetting of the surface of the grid is a function of contact angle, flowrate of the wash oil, the diameter of the grid among other factors, (Fair et al., 1987). Lacking information about the contact angle of the wash oil with the grid surface, the wetted fraction of the grid was assumed to be 0.9. The wetted fraction of the grid packing was changed from its base case assumed value of 0.9, to 1.0 and 0.8 while all other process variables were kept identical to that of the base case, in order to assess the effects on deposit build-up.

It was seen that the mass of coke deposit in the grid was markedly higher at the EOR when the wettability of the packing was reduced and is shown in Fig.4.3 (a) and (b) for both weakly (E = 5 kcal/mol) and highly (E = 75 kcal/mol) temperature dependent adhesion of droplets on the surface. A decrease of 20% in wetted area (from 1.0 to 0.8) resulted in an order of magnitude increase in calculated coke build-up.

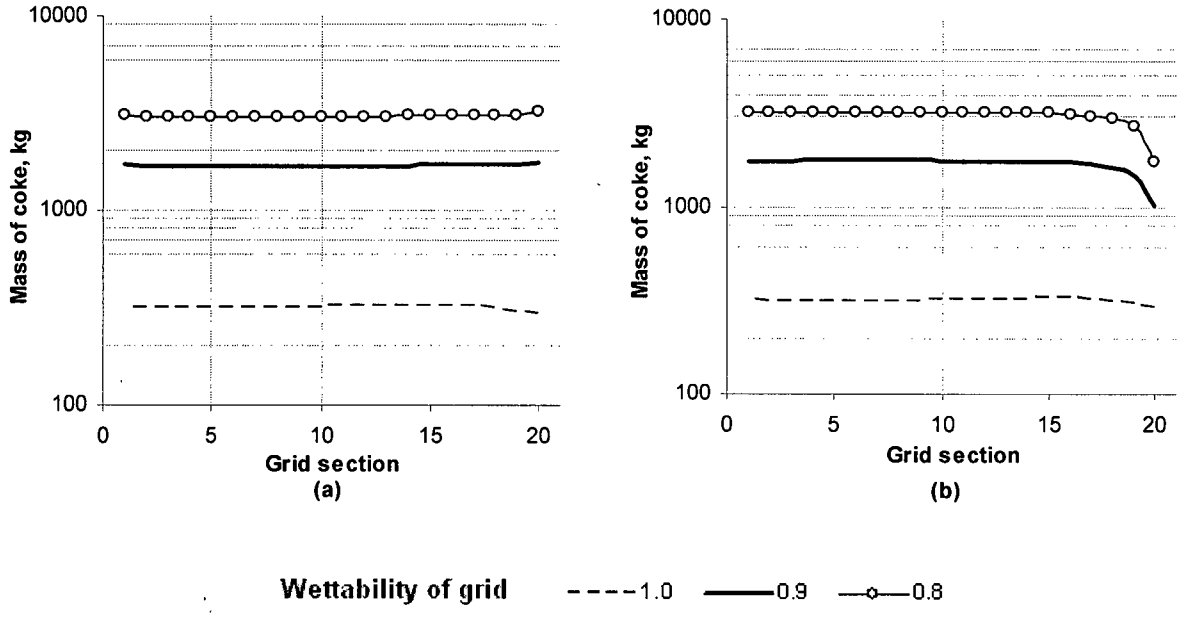

Figure 4.3 Mass of coke deposited in the grid for different wettability of the packing at (a) E = 5 kcal/mol and (b) E = 75 kcal/mol

For both E = 5 and 75 kcal/mol, the mass of coke deposited in the grid for wetted fraction of 1.0 is decreased by roughly a factor of five (from ~ 33800 kg to ~ 6500 kg) when compared with that of wetted fraction of 0.9. When the wetted fraction was changed to 0.8 from 0.9, the mass of coke deposited in the grid was doubled as seen in Fig.4.4(a). In Table 4.4, for E = 5 kcal/mol (i.e less temperature dependent adhesion step), the mass of coke deposited at the EOR for a grid wettability of 1.0 is around 324 kg in each grid section. For a wettability fraction of 0.8, the mass of coke in the mid-sections of the grid is around 3050 kg and increases by a factor of 1.06 at the top of the grid. For E = 75 kcal/mol (i.e highly temperature dependent adhesion step), the mass of coke deposited at the EOR for a grid wettability of 1.0 is around 330 kg in the mid-sections of the grid and then decreases by 11% (from 330 kg to 295 kg) at the top of the grid. For a wetted

fraction of 0.8, the mass of coke in the mid-sections of the grid is around 3150 kg and decreases sharply to 54% (from 3150 kg to 1720 kg) at the top of the grid. The trend of the mass of coke deposit profile for the base case was discussed previously for both E = 5 and 75 kcal/mol.

As the wettability of the grid is reduced, the dry surface in the grid is increased. The total mass deposition flux of droplets depends on the mass transfer, transport and attachment coefficients, as well as the bulk concentration of droplets in the vapour. It can be seen from Table 4.2 that k_{mg} is higher than k_{ml} because of the extra resistance to diffusion for the wetted surface. More droplets will deposit on a unit dry surface area than on a unit wet surface area. So the quantity of droplets deposited in the grid with a wetted fraction of 1.0 is less than for a wetted fraction of 0.9. Similarly for a wetted fraction of 0.8, the mass of droplets deposited will be greater. With more droplets deposited on the surface, more coke will form on the surface.

Table 4.4 Ratio of mass of coke deposited at EOR for grid wettability of 1.0 and 0.8 to 0.9 for both weakly and highly temperature dependent adhesion of droplets on the surface.

	Grid section			
	1st	3rd	15th	20th
E = 5 kcal/mol (temperature insensitive adhesion step)				
Mass of coke deposited (base case), kg	1697	1678	1695	1772
Mass of coke deposited for grid wettability of 1.0	326	320	324	329
Mass of coke deposited for grid wettability of 0.8	3055	3020	3050	3243
E = 75 kcal/mol (temperature sensitive adhesion step)				
Mass of coke deposited (base case), kg	1718	1736	1712	999
Mass of coke deposited for grid wettability of 1.0	332	339	330	295
Mass of coke deposited for grid wettability of 0.8	3145	3176	3134	1720

The amount of coke deposited affects the pressure drop in the grid. In Fig.4.4(b), for wetted fraction of 1.0, the total pressure drop across the grid is lower by a factor of 8 when compared with the base case condition, i.e. 2.5 mbar (1" H_2O) and when the wetted fraction of the grid is changed to 0.8 from 0.9, the pressure drop across the grid is increased by a factor of 6.2. It is seen that the pressure drop across the grid increases sharply when the wetted fraction of the grid is decreased from 0.9 to 0.8. The grid will have a voidage close to zero (grid is filled with coke)

in 4 months from the SOR condition, for a grid which remains completely dry i.e. the wetted fraction of the grid is zero.

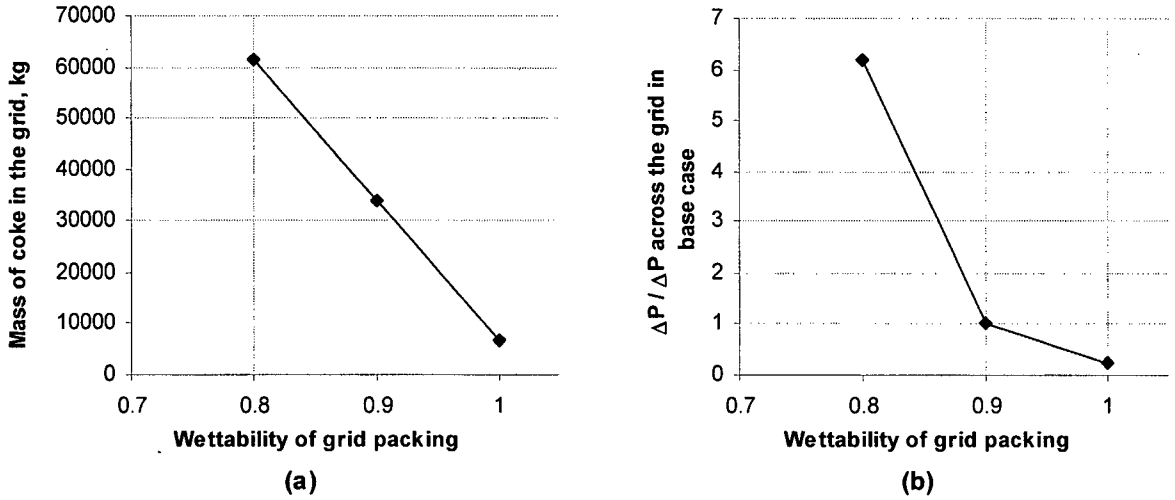

Figure 4.4 (a) Mass of coke in the grid and (b) ratio of pressure drop across the grid at different wettability of packing to the base case.

4.3 Effect of droplet diameter in the grid vapour

In the base case, droplets of different sizes were considered with equal weight fraction, i.e. droplets have a uniform mass distribution. This distribution was considered arbitrarily as the particle size distribution is not known. In the calculation below, each droplet size among the droplet sizes considered in the base case, was studied separately. In all cases the droplets were uniformly distributed in the grid vapour. Droplet diameters between 0.1 and 11 μm were considered. As discussed previously the transport of droplets depends strongly on droplet diameters and hence the mass of coke deposited will also depend on droplet diameter.

From Table 4.2, it can be seen that all droplets are transported to the surface through the wash oil and to the dry surface by diffusion, except for droplet diameters 8 and 11 μm, which move to the dry surface by inertia. Droplet diameters of 0.1, 1 and 11 μm were considered to compare the mass of coke deposited in the grid with that of the base case for both E = 5 and 75 kcal/mol. In Table 4.5, it can be seen that for E = 5 kcal/mol, the mass of coke deposited at the EOR in the

grid sections for individual droplet diameters of 0.1, 1 and 11 μm is approximately 3800, 800 and 3550 kg respectively. Whereas, in the base case with the uniform distribution of droplet sizes, the mass of coke in the grid sections is approximately 1700 kg. For E = 75 kcal/mol, the mass of coke deposited at EOR in most of the grid sections for droplet diameters of 0.1, 1 and 11 μm is approximately 3800, 800 and 3650 kg respectively. But at the top of the grid section the mass of coke deposited for droplet diameters of 0.1, 1 and 11 μm is 3190, 750 and 1360 kg respectively. In the base case the mass of coke deposited at the top of the grid section is approximately 999 kg.

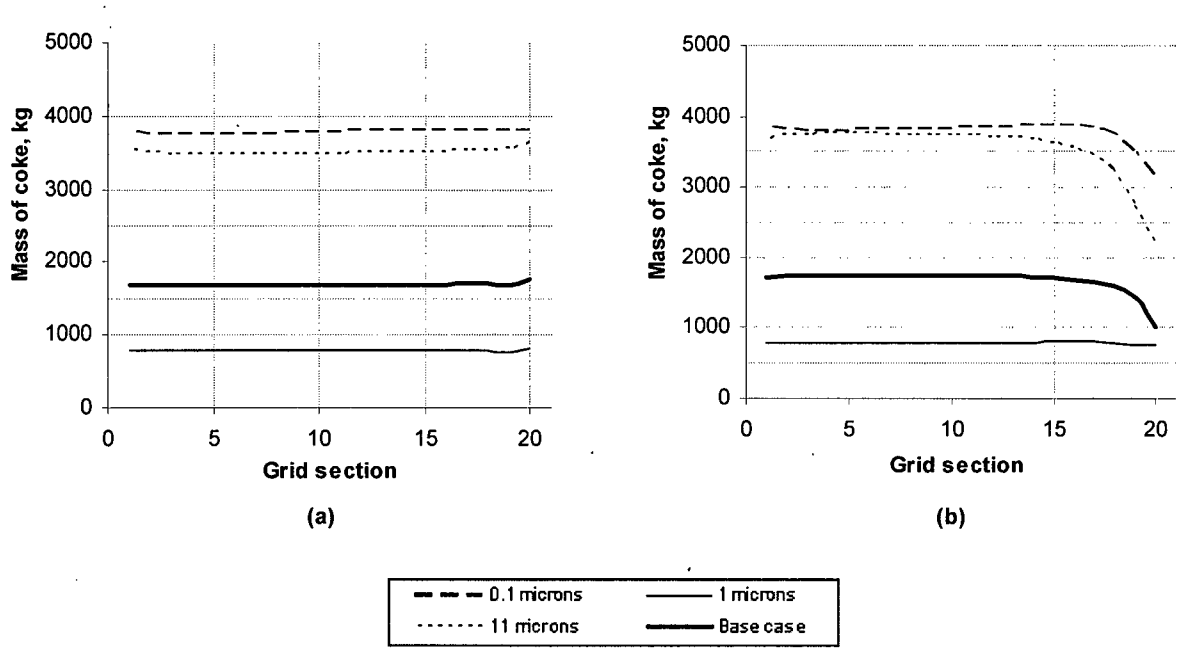

Figure 4.5 Mass of coke deposited in grid at EOR for different droplet diameter at (a) E = 5kcal/mol and (b) E = 75 kcal/mol.

The mass of coke deposited in the grid for 0.1 and 11 μm droplet diameters is higher by a factor of 2.2 and 2 when compared with the base case and is lower by a factor of 2.1 for 1 μm droplet diameter.

For E = 5 kcal/mol (a temperature insensitive adhesion step), the mass of coke deposited in the grid with the 0.1 μm droplets is higher when compared with 1 μm droplets. It was shown previously that 0.1 and 1 μm droplets diffuse to the surface. In Table 4.2(a), mass transfer

coefficients, k_{mg} and k_{ml}, for 0.1 μm droplet is higher than 1 μm droplet by a factor of 4.5, and the attachment coefficient, k_a, is comparatively higher than k_{mg} and k_{ml} for both wet and dry surfaces, Table 4.2(b). So the total mass deposition flux for droplets, ϕ_d, is mass transfer controlled. Droplets with diameter 11 μm diffuse in the wash oil to the surface but they move by inertia from the grid vapour to the dry surface. The liquid phase mass transfer, k_{ml}, for 11 μm droplets is $6x10^{-8}$ m/s, which is roughly 25 and 5 times lower when compared with that of 0.1 and 1 μm, respectively. But the gas phase transport coefficient, k_{tg}, of 11 μm to the dry surface is $2.2x10^{-5}$ m/s (EOR), roughly 0.5 and 0.1 times k_{mg} for 0.1 and 1 μm respectively. Therefore the 11 μm droplet will deposit less on a wetted surface and more on a dry surface when compared with 0.1 and 1 μm droplets. Here it is shown that the mass of coke deposited in the grid by 11 μm droplets is greater than with 1 μm droplets and less than with 0.1 μm droplets. Similarly for E = 75 kcal/mol (a temperature sensitive adhesion step), the mass of coke accumulated on the grid is higher for 11 μm droplets when compared with 1 μm, and lower when compared with 0.1 μm droplets.

Table 4.5 Mass of coke deposited in the grid at EOR for both weakly (E = 5 kcal/mol) and strongly (E = 75 kcal/mol) temperature dependent adhesion of droplet to the surface

	Grid section			
	1st	3rd	15th	20th
E = 5 kcal/mol				
Base case, kg	1697	1678	1695	1772
Droplet diameter is 0.1μm	3824	3770	3837	3831
Droplet diameter is 1μm	792	781	798	809
Droplet diameter is 11μm	3550	3515	3530	3676
E = 75 kcal/mol				
Base case, kg	1718	1736	1712	999
Droplet diameter is 0.1μm	3867	3831	3900	3190
Droplet diameter is 1μm	796	786	802	750
Droplet diameter is 11μm	3680	3778	3653	2248

It can be seen in Fig.4.5(a) and (b) that for both E = 5 and 75 kcal/mol, the mass of coke deposited in the grid in the base case is higher than 1 μm and lower than 11 μm droplet. In

Fig.4.6(a), the total mass of coke in the grid is approximately 76200 kg for a droplet diameter of 0.1 μm, and reduces sharply to approximately 5400 kg when the droplet diameter is 5 μm. It then increases to 70800 kg for 11 μm droplets. The mass mean diameter for the type of droplet size distribution considered as the base case in our study is 3.6 μm. For this diameter of the droplet the total mass of coke deposited in the grid is around 6000 kg (which is around 18% of the base case condition). In Fig.4.6(b), it is seen that the ratio of pressure drop across the grid to the base case decreases from 13.2 to 0.13, when the droplet diameter in the grid vapour increases from 0.1 to 5 μm. And the ratio of pressure drop across the grid to the base case increases from 0.13 to 13.2, when the droplet diameter in the vapour increases from 5 to 11 μm. As given previously, the pressure drop across the grid at EOR condition in the base case is 2.5 mbar (1" H_2O). For the droplet diameter of 3.6 μm (i.e. the mass mean diameter for the type of droplet size distribution considered in the base case), the pressure drop due to mass of coke deposit in the grid will be around 0.35 mbar (which is around 14% of the base case condition). These calculations illustrate the importance of knowing the size distribution of the droplets involved.

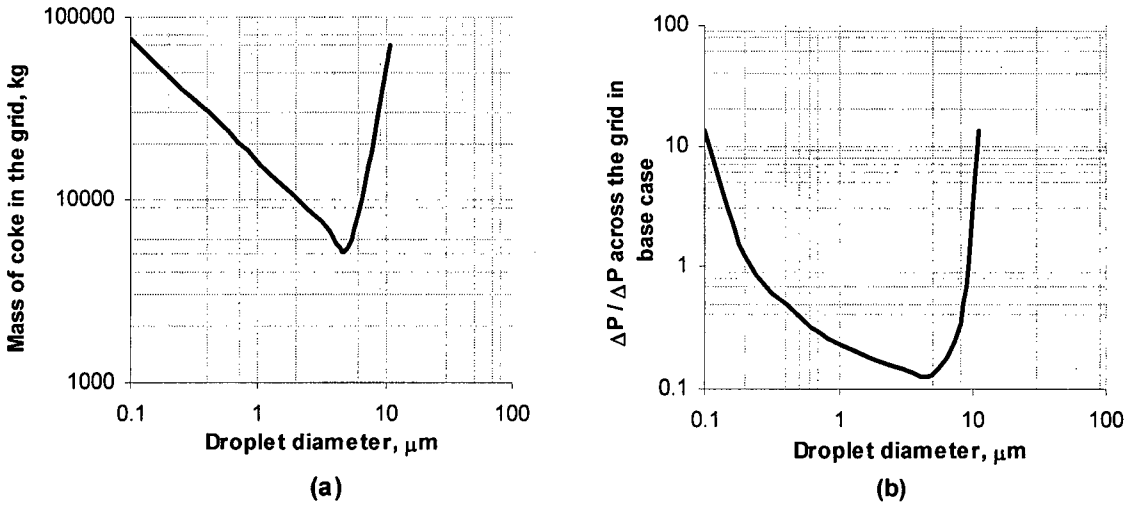

Figure 4.6 (a) Mass of coke in the grid and (b) ratio of pressure drop across the grid at EOR for different droplet diameters in grid vapour compared to the base case.

4.4 Effect of HGO wash oil temperature

Wash oil temperature is an operating variable which could be readily changed in the plant. Hence the temperature of the HGO wash oil was varied from 325 to 300 and 350°C and all other process variables are kept identical to those of the base case.

When the temperature of the HGO wash oil is changed to 300°C from 325°C (base case), the temperature in the grid is reduced by around 1% when compared with that of the base case. When the temperature of the HGO wash oil is increased from 325 to 350°C, the temperature throughout the grid also increases by about the same magnitude, Table 4.6. Temperature changes of this magnitude are not expected to have a great effect on the pressure drop across the grid. The temperature profiles in the grid when HGO wash oil temperature is 300 and 350°C are shown in Fig.4.7(a).

The grid temperature change is relatively small when the HGO wash oil temperature is changed from 325 to 300°C because the change in $m_{vap} * c_{p,vap}$ in the grid is only around 2% (i.e. for base case it is ~ 2.39×10^6 kJ/°C h and at the HGO wash oil temperature of 300°C it is ~2.34×10^6 kJ/°C h) which $m_{wash} * c_{p,wash}$ in the grid is around 3% (i.e. for base case it is ~ 5×10^5 kJ/°C h and at the HGO wash oil temperature of 300°C it is ~5.16×10^5 kJ/°C h). Similarly, when the wash oil temperature is changed from 325 to 350°C, the changes in $m_{vap} * c_{p,vap}$ and $m_{wash} * c_{p,wash}$ are of similar magnitude. Due to the small change in the grid temperature, the change in the bulk concentration of the droplets, c_b, and the mass flowrate of +524°C hydrocarbons is expected to be less in the droplets. When the HGO wash oil temperature is decreased from 325 to 300°C, the bulk concentration of droplets, c_b, in the grid vapour is slightly increased. The increase of c_b in the grid section is 1.3% at the bottom and rises gradually towards the top of the grid where it is around 3.5% when compared with the base case, Table 4.6. When the HGO wash oil temperature is increased from 325 to 350°C, the bulk concentration of droplets in the grid vapour is decreased. The decrease of c_b in the grid section is of the same magnitude. Similarly, the mass flowrate of +524°C hydrocarbons in the droplets which are in grid vapour also increases when the bulk concentration of droplets in the grid vapour increases and vice versa. The change in the mass flowrate of +524°C is around 1%. This can be seen in Fig. 4.7(d).

For the lower value of E = 5 kcal/mol (a temperature insensitive adhesion rate), the mass of coke deposited in the grid is greater when the temperature of the HGO wash oil is reduced, and less when the temperature of HGO wash oil is increased from the base case temperature, i.e. 325°C. When the HGO wash oil temperature is changed from 325°C (base case) to 300°C, the increase in mass of coke in grid section is 8.7 kg, i.e. around 0.5%, at the bottom of the grid and increases

towards the top of the grid where the extra mass of coke is 19.7 kg, i.e. around 1.1% (Fig.4.7(d) and Table 4.6). This increase at the top is due to the fact that c_b is higher at the top than at the bottom of the grid. When the HGO wash oil temperature is changed to 350°C from that of the base case, the decrease in mass of the coke in the grid section is 7.57 kg (around 0.5%) at the bottom of the grid and decreases towards the top of the grid where the decrease in mass of the coke is 25.2 kg (around 1.4%).

Table 4.6 Effect of change in HGO wash oil temperature

	Grid section			
	1st	3rd	15th	20th
Base case				
Temperature of the grid, °C	394	394.4	394.2	380.1
Bulk concentration, c_b, kg/m^3	0.741	0.716	0.727	0.776
Mass of coke (for E = 5 kcal/mol, EOR), kg	1697	1678	1695	1772
Mass deposition flux (for E = 5 kcal/mol), ϕ_d, kg/m^2 s	2.66×10^{-6}	2.63×10^{-6}	2.66×10^{-6}	2.81×10^{-6}
Mass of coke (for E = 75 kcal/mol, EOR), kg	1718	1736	1712	999
Mass deposition flux (for E = 75 kcal/mol), ϕ_d, kg/m^2 s	2.69×10^{-6}	2.73×10^{-6}	2.68×10^{-6}	1.59×10^{-6}
HGO wash oil temperature changed from 325 (base case) to 300 °C				
Temperature of the grid, °C	393.8	394.2	392.4	376.4
Bulk concentration, c_b, kg/m^3	0.751	0.734	0.765	0.802
Mass of coke (for E = 5 kcal/mol, EOR), kg	1705	1696	1738	1792
Mass deposition flux (for E = 5 kcal/mol), ϕ_d, kg/m^2 s	2.67×10^{-6}	2.66×10^{-6}	2.72×10^{-6}	2.85×10^{-6}
Mass of coke (for E = 75 kcal/mol, EOR), kg	1727	1741	1677	864
Mass deposition flux (for E = 75 kcal/mol), ϕ_d, kg/m^2 s	2.7×10^{-6}	2.73×10^{-6}	2.63×10^{-6}	1.37×10^{-6}
HGO wash oil temperature changed from 325 (base case) to 350 °C				
Temperature of the grid, °C	394.2	394.8	394.8	384.2
Bulk concentration, c_b, kg/m^3	0.731	0.697	0.698	0.746
Mass of coke (for E = 5 kcal/mol, EOR), kg	1689	1664	1668	1747
Mass deposition flux (for E = 5 kcal/mol), ϕ_d, kg/m^2 s	2.65×10^{-6}	2.61×10^{-6}	2.61×10^{-6}	2.77×10^{-6}
Mass of coke (for E = 75 kcal/mol, EOR), kg	1740	1767	1761	1169
Mass deposition flux (for E = 75 kcal/mol), ϕ_d, kg/m^2 s	2.73×10^{-6}	2.77×10^{-6}	2.76×10^{-6}	1.86×10^{-6}

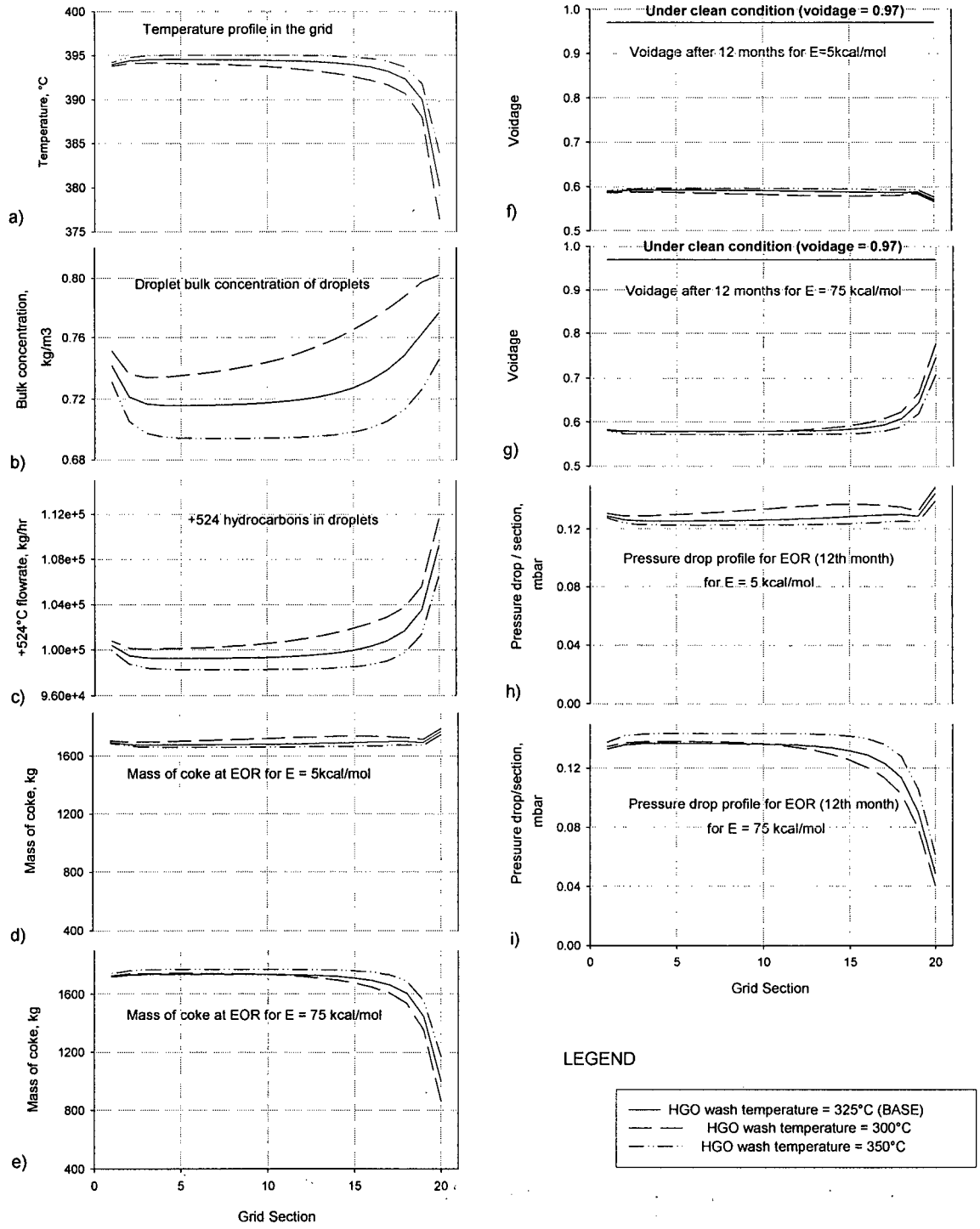

Figure 4.7 Profiles for grid when HGO wash oil temperature was changed.

The mass deposition flux for droplets, ϕ_d, depends not only on the bulk concentration of the droplets in the grid vapour but also the deposition coefficient of the droplets, k_d. As we have seen earlier, all droplets fall in the diffusion transport regime, both for wet and dry surfaces, except

for droplet diameters 8 and 11 μm which are in the inertia transport regime for the dry surface. The dry surface of the packing is just 10% of the packing. The major contribution to the droplet deposition on the packing surface is by diffusion of the droplets. It was discussed in a previous section of this chapter that when the temperature is reduced, the attachment coefficient of droplets, k_a, also is reduced, but the bulk concentration of the droplets increases. The increase in bulk concentration of the droplets in vapour for E = 5 kcal/mol is controlling because of which the mass deposition flux for droplets increases and vice versa. At the SOR condition when the HGO wash oil temperature is 300°C, the mass deposition flux for droplets, ϕ_d, in each grid section is higher when compared with that of the base case. And also when the HGO wash oil temperature is 350°C, the mass deposition flux for droplets, ϕ_d, at the SOR condition in each grid section is lower when compared with that of the base case and can be seen in Table 4.6.

For the higher value of E = 75 kcal/mol (a temperature sensitive adhesion rate), the mass of the coke deposited in the grid is less when the temperature of the HGO wash oil is reduced and more when the temperature of HGO wash oil is increased from the base case temperature i.e. 325°C. This result is expected, i.e., cooling the grid would reduce fouling. When HGO wash oil temperature is changed from 325°C (base case) to 300°C, the decrease in mass of coke in the grid section is 8.6 kg (around 0.5%) at the bottom and decrease towards the top of the grid by 135 kg (around 14%) when compared with the base case (Table 4.6). When HGO wash oil is changed to 350°C from the base case, the increase in mass of the coke in the grid section is 22.4 kg (around 1.3%) at the bottom and increase towards the top of the grid by 169 kg (around 17%) when compared with the base case. This decrease at the top is due to the lower temperature at the top than in the mid-sections of the grid. It was also shown before that the temperature change in the grid sections increases from bottom to the top section of the grid. It was seen in a previous section of this chapter that when temperature is reduced the attachment coefficient, k_a, of the droplet is reduced for higher values of E. So when E is higher (i.e. high temperature dependent adhesion of the droplet to the surface), k_a becomes a controlling factor apart from other transfer coefficients and bulk concentration of droplets in vapour, for change in mass deposition flux for droplets at different temperatures. At the SOR condition when the HGO wash oil temperature is 300°C, the mass deposition flux for droplets, ϕ_d, in the grid section is lower than for the base case. For the HGO wash oil temperature of 350°C, the mass deposition flux for droplets, ϕ_d, in the grid section is higher than in the base case.

As the coke deposit increases on the grid due to droplet deposition on the surface, the voidage of the grid decreases. Fig.4.7(f) and (g) gives the voidage of the grid section for E = 5 and 75 kcal/mol at the EOR condition. Similarly the pressure drop in the grid section at the EOR condition is evaluated at both E = 5 and 75 kcal/mol, and can be seen in Fig.4.7(h) and (i).

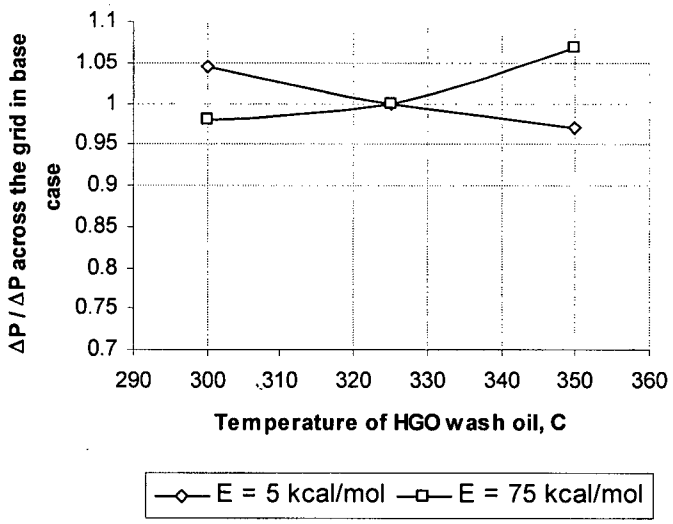

Figure 4. 8 Pressure drop across the grid at different temperatures of HGO wash oil compared with base case.

For E = 5 kcal/mol, when the temperature of the HGO wash oil is decreased from 325 to 300°C, the pressure drop across the grid is increased above the base case, 2.5 mbar (1" H_2O), by a factor of 1.05 and when the HGO wash oil temperature is increased from 325 to 350°C, the pressure drop across the grid is decreased by 3% (from 2.5 mbar to 2.43mbar). These changes are negligible.

For E = 75 kcal/mol, when the temperature of the HGO wash oil is decreased from 325 to 300°C, the pressure drop across the grid is decreased by 2% (from 2.5 mbar to 2.45 mbar). When the HGO wash oil temperature is increased from 325 to 350°C, the pressure drop across the grid is increased by a factor of 1.07, and can be seen in Fig.4.8.

4.5 Effect of HGO wash oil flowrate

Wash oil flowrate is another operating variable which could influence coke build-up, and could be readily changed in the plant operation. The flowrate of HGO wash oil was varied from 44 kg/s (24 kbpd) to 55 kg/s (30 kbpd) and 73 kg/s (40 kbpd) while all other process variables were kept the same as those of base case. By increasing the HGO flowrate, the wetted fraction of the grid might be affected, but in this calculation the wettability of the grid was held constant at 0.9. Studies of the wettability of structured packings were done by Meier et al. (1977) and Billet (1987), for the air-water system using Mellapak 250Y, Gempak 2A and Montz B1-300. They studied the wettability of the packing with varying flowrates of water in the packing for two different diameters of the packed bed. Billet (1987) observed that for smaller packed bed diameter of 0.22 m, when the $N_{Re,film}$ (as defined by Eq.(2.36)) was increased by a factor of 2 from 10 to 20, the wetted fraction in the packing increased by a factor of 1.1. For their study the $N_{Re,film}$ was in the range from 10 to 200. For the packed bed diameter of 1 m, Meier et al. (1977) showed that when $N_{Re,film}$ was increased by a factor of 2 from 100 to 200, the wetted fraction in the packing increased by a factor of 1.03. Billet (1987) concluded that, as the diameter of packed bed was increased, the wetted fraction increase with water flowrate was reduced. Data for pressure drop in the air-water system for Flexigrid#2 is available in the Koch-Glitsch technical brochure (2004) and Kister (1992), but data on the wettability of the grid packing is not available. In the present work, the diameter of the grid bed is 9.1m. For HGO wash oil flowrate of 24 (base case), 30 and 40 kbpd, the $N_{Re,film}$ in the grid is around 120, 160 and 190, respectively. As we have seen previously that the $N_{Re,film}$ range of 100 to 200 the wetted fraction is increased by a factor of 1.03 for 1m packed bed diameter, for this study it was assumed that the wetted fraction of the grid will not change.

It should be recalled that a basic assumption in the work is that the wash oil does not remove droplets which reach the surface, although the adhesion coefficient, k_a, will be reduced as higher liquid velocities occur on the surface of the grid. When the flowrate of HGO wash oil is changed from 24 to 30 kbpd, the temperature in the grid is reduced by 0.7% when compared with that of the base case. When the flowrate of HGO wash oil is increased from 24 to 40 kbpd, the temperature in the grid reduces by around 1.5% when compared with that of the base case,

(Table 4.7). The temperature profiles of the grid for different HGO wash flowrates are shown in Fig.4.9(a).

Table 4.7 Effect of change in HGO wash oil flowrate

	Grid section			
	1st	3rd	15th	20th
Base case				
Temperature of the grid, °C	394	394.4	394.2	380
Bulk concentration, c_b, kg/m^3	0.741	0.716	0.727	0.776
Mass of coke (for E = 5 kcal/mol, EOR), kg	1697	1678	1695	1772
Mass deposition flux (for E = 5 kcal/mol), ϕ_d, kg/m^2 s	2.66×10^{-6}	2.63×10^{-6}	2.66×10^{-6}	2.81×10^{-6}
Mass of coke (for E = 75 kcal/mol, EOR), kg	1718	1736	1712	999
Mass deposition flux (for E = 75 kcal/mol), ϕ_d, kg/m^2 s	2.69×10^{-6}	2.73×10^{-6}	2.68×10^{-6}	1.59×10^{-6}
HGO wash oil flowrate changed from 24 (base case) to 30kbpd				
Temperature of the grid, °C	394	394.1	391.1	376.4
Bulk concentration, c_b, kg/m^3	0.742	0.725	0.78	0.793
Mass of coke (for E = 5 kcal/mol, EOR), kg	1715	1702	1710	1786
Mass deposition flux (for E = 5 kcal/mol), ϕ_d, kg/m^2 s	2.66×10^{-6}	2.67×10^{-6}	2.72×10^{-6}	2.88×10^{-6}
Mass of coke (for E = 75 kcal/mol, EOR), kg	1695	1708	1563	821
Mass deposition flux (for E = 75 kcal/mol), ϕ_d, kg/m^2 s	2.73×10^{-6}	2.64×10^{-6}	2.45×10^{-6}	1.3×10^{-6}
HGO wash oil flowrate changed from 24 (base case) to 40kbpd				
Temperature of the grid, °C	393.2	392	391	371
Bulk concentration, c_b, kg/m^3	0.0103	0.0103	0.0105	0.0105
Mass of coke (for E = 5 kcal/mol, EOR), kg	0.748	0.762	0.787	0.798
Mass deposition flux (for E = 5 kcal/mol), ϕ_d, kg/m^2 s	1730	1723	1724	1811
Mass of coke (for E = 75 kcal/mol, EOR), kg	2.66×10^{-6}	2.68×10^{-6}	2.75×10^{-6}	2.91×10^{-6}
Mass deposition flux (for E = 75 kcal/mol), ϕ_d, kg/m^2 s	1637	1580	1465	597
Mass deposition flux (for E=75 kcal/mol), ϕ_d, kg/m^2 s	2.66×10^{-6}	2.52×10^{-6}	2.32×10^{-6}	9×10^{-7}

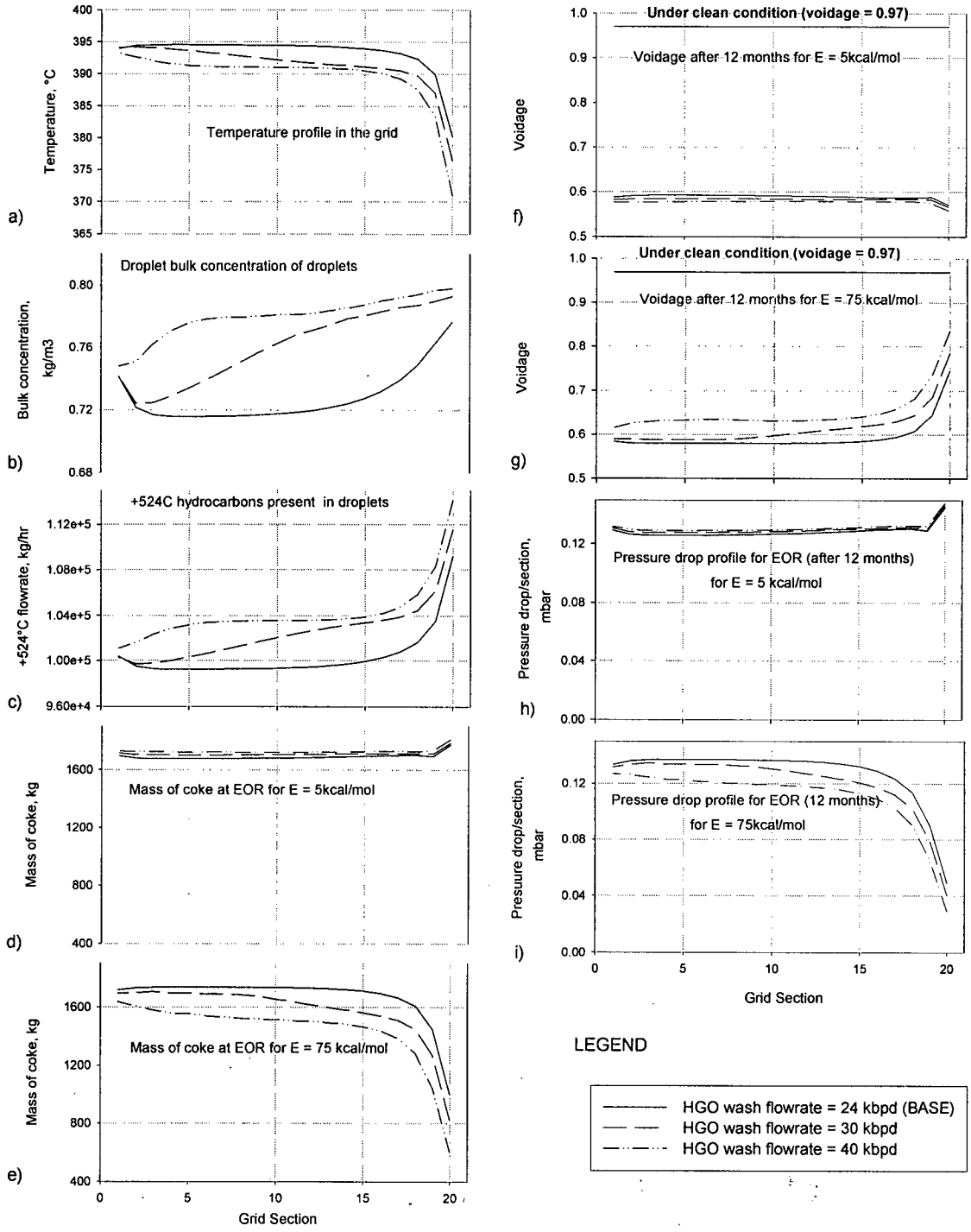

Figure 4. 9 Profiles for grid when wash oil flowrate was changed.

Over the range considered, wash oil flowrate did not affect droplet concentration. When HGO wash oil flowrate is increased from 24 to 30 kbpd, the bulk concentration of the droplets in the vapour, $c_{b,}$ is increased by a negligible factor of 1.001 when compared with the base case (Table

4.7). At the top of the grid (20th section), the increase of c_b when compared with the base case is by a factor of 1.02. When the HGO wash oil flowrate is increased from 24 to 40 kbpd, the increase in bulk concentration of the droplet in the vapour in the grid section is by a factor of 1.01 when compared with the base case and at the top of the grid (20th section), the increase of c_b when compared with the base case is by a factor of 1.03 and can be seen in Fig.4.9(c). Similarly, the mass flowrate of +524°C hydrocarbons in the droplets which are in the vapour space also increases when bulk concentration of the droplet in vapour increases and vice versa. This can be seen in Fig.4.9(d).

For the lower value of E = 5 kcal/mol, when the HGO wash oil flowrate is raised from 24 to 30 kbpd the increase in mass of coke in the grid section is approximately 18 kg (around 1%) when compared with the base case (Table 4.7). When HGO wash oil flowrate is 40 kbpd the increase in mass of the coke in the grid section is approximately 33 kg (around 2.2%) when compared with the base case (Table 4.7).

It was seen that the increase in bulk concentration of the droplets in the vapour for E = 5 kcal/mol, is the controlling factor for droplets deposition. Though there is an extra resistance for droplet deposition (k_a is reduced because of increase in flowrate of wash oil), it is seen that the mass deposition flux for droplets increases and vice versa. So when HGO wash oil flowrate is 30 kbpd, the mass deposition flux for droplets in the grid section is higher than that of base case and also when HGO wash oil flowrate is 40 kbpd the mass deposition flux for droplets, ϕ_d, in the grid section is slightly higher than both base case and when HGO wash oil flowrate is 30 kbpd.

For the higher value of E = 75 kcal/mol (a temperature sensitive adhesion rate), the mass of the coke deposited in the grid is significantly less when the flowrate of the HGO wash oil is increased. When HGO wash oil flowrate is changed from 24 kbpd (base case) to 30kbpd, the decrease in mass of coke in the grid section is approximately 23 kg (around 1.3%) at the bottom and decrease further by 178 kg (around 18%) at the top of the grid when compared with the base case (Table 4.7). When the HGO wash oil flowrate is changed to 40 kbpd, the decrease in mass of the coke in the grid section is 81 kg (around 5%) at the bottom of the gird and decrease further by 401 kg (around 40%) at the top of the grid when compared with the base case (Table 4.7). The mass transfer and transport coefficients of the droplets remain constant for a specific grid

section temperature, but the attachment coefficient, k_a, of the droplet changes for different values of E. Also when the flowrate of wash oil increases the probability of droplet sticking to the surface also decreases. When E is higher, the flowrate of HGO wash oil is higher (above the base case) and temperature is lower than that of the base case, k_a becomes a controlling factor, apart from other transfer coefficients and bulk concentration of droplets in vapour, for the change in total mass deposition flux for droplets at different temperatures. For the HGO wash oil flowrate of 40 kbpd, ϕ_d in the grid is lower than that of the base case and also when the HGO wash flowrate is 30 kbpd, (Table 4.7). For higher flowrates of HGO wash oil, the magnitude of the decrease in the total mass of the coke deposit in the grid at E = 75 kcal/mol is higher by a factor of 3 when compared with that of E = 5 kcal/mol.

As the coke deposit increases on the grid, the voidage of the grid decreases. Fig.4.9(f) and (g) gives the voidage of the grid section for E = 5 and 75 kcal/mol at the EOR condition. Similarly, the pressure drop in the grid section at the EOR is evaluated at both E = 5 and 75 kcal/mol. They are shown in Fig.4.9(h) and (i). The pressure drop profile in the grid is dependent on the mass of the coke deposit in the grid. For E = 5 kcal/mol, when the flowrate of HGO wash oil is increased from 24 to 30 kbpd, the pressure drop across the grid is increased above the base case, 2.5 mbar (1" H_2O), by a factor of 1.05. When the HGO wash oil flowrate is increased from 24 to 40 kbpd, the pressure drop across the grid is increased by a factor of 1.07.

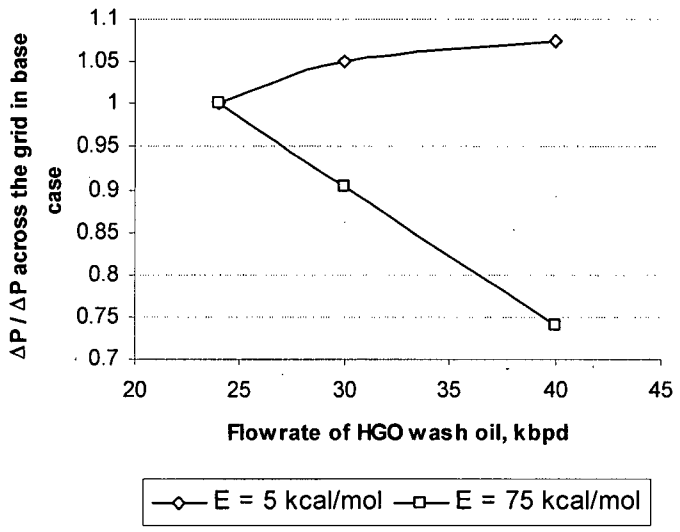

Figure 4.10 Pressure drop across the grid at different flowrates of HGO wash oil compared with base case.

For E = 75 kcal/mol, when the flowrate of HGO wash oil is increased from 24 to 30 kbpd, the pressure drop across the grid is decreased by 10% (from 2.5 mbar to 2.25 mbar). When the HGO wash oil flowrate is increased from 24 to 40kbpd, the pressure drop across the grid decreased by 26% (from 2.5 mbar to 1.8 mbar), and can be seen in Fig.4.10.

Even by changes in flowrate of HGO wash oil of this magnitude, changes to the pressure drop across the grid are still small compared to those due to small changes in the wettability of the grid.

Chapter 5: Conclusions and Recommendations

5.1 Conclusions

A model has been developed to calculate coke build-up and pressure drop with time in a counter-current flow in a scrubber containing a structured packing. The model incorporates HYSYS and sub-models from the literature to describe the transport of droplets, adhesion and coke formation. The pressure drop in a fluid coker scrubber grid increases due to the formation of coke on the grid surface. The complex geometry of the structured packing was calculated with deposit on the surface to follow the voidage and specific surface of heavily coked packings. In industrial operation, the pressure drop across the grid was reported to be around 2.5 mbar (1" H_2O) at the end of a one-year run. At this condition the adjustable parameter *k"* was evaluated for the two extremes of low (E = 5 kcal/mol) and high (E = 75 kcal/mol) temperature sensitive adhesion rate as 2.8×10^{-2} s^2/m and 3.05×10^{-25} s^2/m, respectively. As the vapour enters the grid there is a slight (<1°C) increase in temperature, followed by a near constant temperature over the next 15 sections (remains isothermal) after which it drops by about 15°C. Thus the temperature is higher in the mid-sections of the grid than either the top (20^{th} section) or the bottom (1^{st} section). It was seen that at E = 5 kcal/mol, the mass of coke in the grid was relatively uniform, but for E = 75 kcal/mol, it has a sharper axial profile at the top of the grid. Here for E = 75 kcal/mol, the attachment coefficient was the controlling factor for coke deposit formation whereas for E = 5 kcal/mol, the bulk concentration of droplets in the grid vapour was the dominant factor.

The effects of the wetted surface fraction on the complex geometry and droplet size on coke build-up were investigated. Both parameters strongly influence the coke build-up in the grid. The value assumed for the wetted fraction of the grid surface is extremely important for calculating the deposition rate of droplets and the pressure drop build-up in the grid. When the wetted fraction of the grid was increased from 0.9 (base case) to 1.0, the pressure drop across the grid was decreased by 87.5% (from 2.5 mbar to 0.313 mbar). When it was reduced to 0.8 from 0.9, the pressure drop across the grid was increased by a factor of 6.2.

In the base case, a uniform distribution by weight fraction of eight different sizes of the droplets were considered with 0.1 μm as the smallest and 11 μm as the largest. When the droplets size was considered uniform in the grid vapour, it was seen that the pressure drop across the grid decreased by 2 orders of magnitude (from 33 mbar to 0.33 mbar) when the droplet size increased from 0.1 μm to 5 μm, and beyond 5 μm to 11 μm the pressure drop increased by 2 orders of magnitude. The mass mean diameter of the droplet for the droplet size distribution considered in our study (i.e. the base case) is 3.6 μm. The pressure drop in the grid for the mass mean diameter is 0.35 mbar, which is 14% of the base condition.

The axial temperature profile through the grid due to changes in HGO wash oil temperature and flow strongly affected the coke deposition pattern in the grid for the case of strongly temperature dependent adhesion. When the temperature of HGO wash oil was decreased from 325 (base case) to 300°C, the grid temperature was lowered primarily at the grid top. Due to this there was higher bulk concentration of the droplets and lower coking rates for the temperature sensitive adhesion case. No significant effect was observed for the temperature insensitive adhesion case. When the of HGO wash oil temperature was increased from 325 (base case) to 350°C, the temperature was increased at the top of the grid, and coke build-up increased for the temperature dependent adhesion case. The temperature change of this magnitude had little effect on the pressure drop across the grid, i.e. the change was roughly within ± 5% of the base case condition.

When the flowrate of HGO wash oil was increased from 24 kbpd to 30 and 40 kbpd, the grid temperature was lowered particularly in the top sections. For the temperature-sensitive adhesion case, the pressure drop in the grid decreased by 10% (from 2.5 mbar to 2.25 mbar) and 26% (from 2.5 mbar to 1.8 mbar) for the 30 and 40 kbpd HGO wash oil flows, respectively. For the temperature-insensitive adhesion case, the pressure drop in the grid increased by a factor of 1.05 and 1.07 for the 30 and 40 kbpd HGO wash oil flows. Even by changing the flowrate of HGO wash oil by this magnitude, the pressure drop across the grid was not greatly affected compared to the changes in pressure drop due to small changes in the wettability of the grid, or in the assumed droplet size.

5.2 Recommendations

To improve this model, it is very important to understand the wettability of the HGO wash oil on the packing. Some experiments need to be done to determine the wettability of the HGO wash oil on the grid metal and on the coke covering the grid. Also, the adhesion model should be confirmed experimentally for this system. Furthermore, the vapour, liquid and droplet distribution in the grid need to be studied, perhaps by using CFD software, to give some accuracy to the study. Coke deposition in the grid is dependent on the flowrates of vapour, liquid and droplet distribution and temperature in the grid. For a large diameter grid, radial variations in wash oil flowrates and wettability should be established, as the model suggests a much higher deposit build-up on the dry sections. The predicted axial deposit distributions could be verified from plant data. Extra calculations need to be done, by reducing the transport coefficients by a factor of 2, 5, 10 etc. to see how the constant k'' will change.

References

Bemer, G.G., Kalis, G.A.J., "*A New Method to Predict Hold-up and Pressure Drop in Packed Columns*", Transactions of the Institution of Chemical Engineers, Vol.56, 3, pp.200-204, 1978.

Billet, R., "*Performance of Low Pressure Drop Packings*", Chemical Engineering Communications, Vol.89, 9, pp.362-368, 1987.

Bird, B.R., Stewart, W.E., Lightfoot, E.N., "*Transport Phenomena*", Wiley, New York, 2nd Edition, 2001.

Bravo, J.L., Rocha, J.A., Fair, J.R., "*Pressure Drop in Structured Packing*", Hydrocarbon Processing, Vol.65, 3, pp.45-49, 1986.

Buchanan, J.E., "*Pressure Gradient and Liquid Hold-up in Irrigated Packed Towers*", Industrial & Engineering Chemistry Fundamentals, Vol.8, 3, pp.502-511, 1969.

Cleaver, J.W. and Yates, B.A., "*Sublayer Model for the Deposition of Particles from a Turbulent Flow*", Chemical Engineering Science, Vol.30, 8, pp.983-992, 1975.

Crittenden, B.D., Hout, S.A., Alderman, N.J., "*Model Experiments of Chemical Reaction Fouling*", Chemical Engineering Research and Design, Vol.65, 2, pp.165-170, 1987.

Dean, J.A., "*Lange's Handbook of Chemistry*", McGraw-Hill, New York, 15th Edition, 1998.

Epstein, N., "*Elements of Particle Deposition onto Nonporous Soild Surfaces Parallel to Suspension Flows*", Experimental Thermal and Fluid Science", Vol.14, 4, pp.323-334, 1997.

Fahiminia, F., Watkinson, A.P., Epstein, N., "*Investigation of Initial Fouling Rates of*

Calcium Sulfate Solutions under Non-boiling Conditions", Proceedings Conference on Heat Exchanger Fouling and Cleaning - Fundamentals and Applications, Santa Fe, USA, 32, 2003.

Fair, J.R., Bravo, J.L., "*Distillation Columns containing Structured Packing*", Chemical Engineering Progress, Vol.86, 1, pp.19-29, 1990.

Forney, L.J., Spielman, L.A., "*Deposition of Coarse Aerosols from Turbulent Flow*", Journal of Aerosol Science, Vol.5, 3, pp.257-271, 1974.

Friedlander, S.K., Johnstone, H.F., *"Deposition of Suspended Particles from Turbulent Gas Streams*", Industrial and Engineering Chemistry, Vol.49, pp.1151-1156, 1957.

Gray, M.R., "*Upgrading Petroleum Residues and Heavy Oils*", Marcel Dekker, Inc., New York, 1994.

Hutchinson, P. C., Hewitt, G. F., Dukler, A.E., "*Deposition of Liquid or Solid Dispersions from Turbulent Gas Streams : A Stochastic model*", Chemical Engineering Science, Vol.26, 3, pp.419-439, 1971.

Jankovic, J., "*Simulation of the Scrubber Section of a Fluid Coker*", MASc Thesis, UBC, April, 2005.

Kister, H. Z., "*Distillation Design*", Publisher: New York; Mc Graw-Hill, 1992.

Koch-Glitsch technical brochure, website: http://www.koch-glitsch.com/koch/product brochures/KGSS.pdf, date of access April, 2004.

Leva, M., "*Flow through Irrigated Dumped Packing Pressure Drop, Loading and Flooding*", Chemical Engineering Progress Symposium series, Vol.50, 10, pp.51-59, 1954.

Liu, B.Y.H., Agarwal, J.K., *"Experimental Observation of Aerosol Deposition in Turbulent Flow"*, Journal of Aerosol Science, Vol.5, 4, pp.145-155, 1974.

Meier, W., Stoecker, W.D., Weinstein, B., "*Performance of New High Efficiency Packing*", Chemical Engineering Progress, Vol.73, 11, pp.71-77, 1977.

Papavergos, P.G., Hedley, A.B., *"Particle Deposition Behaviour from Turbulent Flows*", Chemical Engineering Research and Design, Vol.62, 5, pp.275-295 , 1984

Paterson, W.R., Fryer, P.J., "*A Reaction Engineering Approach to the Analysis of Fouling*", Chemical Engineering Science, Vol.43, 7, pp.1714 – 1717, 1988.

Perry's *Chemical Enigneers' Handbook*, Publisher : New York; Mc Graw-Hill, 7th Edition, 1997.

Reynolds, D.B., "*The Economics of Oil Definitions: The Case of Canada's Oil Sands*", Organization of the Petroleum Exporting Countries Review, Vol.29, 3, pp.51-73, 2005

Rose, I.C., Watkinson, A.P., Epstein, N., "*Testing a Mathematical Model for Initial Chemical Reaction Fouling using a Dilute Protein Solution*", Canadian Journal of Chemical Engineering, Vol.78, 1, pp.5-11, 2000.

Schlichting, H., "*Boundary Layer Theory*", Mc Graw-Hill, New York, 6th Edition, 1968.

Sherwood, T. K., Shipley, G. H., Holloway, F. A, L., "*Flooding Velocities in Packed Columns*", Industrial and Engineering Chemistry, Vol.30, 7, pp.765-769, 1938.

Skelland, A.H.P., "*Diffusional Mass Transfer*", Wiley-Interscience, New York, 1st Edition, 1974.

Spiegel, L., Meier,W., "*A Generalized Pressure Drop Model for Structured Packings*", Institution of Chemical Engineers Symposium Series No. 128, B85-94, 1992.

Stichlmair, J. G., Fair, J.R., "*Distillation Principles and Practices*", Wiley-VCH, New York, 1998.

Stichlmair, J., Bravo, J.L., Fair, J.R., "*General Model for Prediction of Pressure Drop and Capacity of Counter-current Gas/Liquid Packed Columns*", Gas Separation and

Purification, Vol.3, 1, pp.19-28, 1984.

Strigle, R. F., "*Packed Tower Design and Applications*", Gulf Publication Co., Houston, 1994.

Vasak, F., Bowen, B.D., Chen, C.Y., Kastanek, F., Epstein, N., "*Particle Deposition in Laminar and Turbulent Flows*", Canadian Journal of Chemical Engineering, Vol.73, pp.785-792, 1995.

Watkinson, A.P., "*Chemical Reaction Fouling of Organic Fluids*", Chemcial Engineering and Technology, Vol.15, 2, pp.82-90, 1992.

Wiehe, I. A., "*A Phase-Separation Kinetic Model for Coke Formation*", Industrial & Engineering Chemistry Research, Vol.32, 11, pp.2447-2454, 1993.

Yue, C., Watkinson, A. P., Lucas, J. P., Chung, K. H., "*Incipient Coke Formation during Heating of Heavy Hydrocarbons*", Fuel, Vol.83, 11-12, pp.1651-1658, 2004.

Appendix I : Calculation of voidage and specific surface area of the cleaned and fouled Koch-Glitsch Flexigrid #2.

Koch-Glitsch Flexigrid #2 is available in a wide variety of materials, (Koch-Glitsch technical brochure, 2004), and in this study SS 304 material of construction is considered. It is constructed in 1524 mm (60") long x 406 mm (16") wide x 70 mm (2.75") tall modules (i.e the section height). The vertical, parallel blades of the packing are held in a fixed position with welded cross members. During installation in the tower, each successive layer of the grid packing is rotated 45 degrees to the previous layer to achieve improved efficiency and enhance bed integrity.

Blades of the Flexigrid packing are bent out an angle from the vertical to induce turbulent contact between the rising vapours and descending liquid. There are no horizontal surfaces on the packing so that the packing can drain freely and liquid and solids do not collect. This minimizes the liquid residence time or liquid holdup which reduces the potential for coking.

Table AI.1 Details of the FlexiGrid #2, Koch-Glitsch technical brochure (2004)

Dimension of an element, mm (inches)	1524 (60") x 406 (16") x 70 (2.75")
Weight of the packing/Volume of the packed bed, kg/m^3	263
Thickness of each blade, mm	1.5
Specific surface area, m^2/m^3	45
Material of construction of the grid	SS 304 (8000 kg/m^3 density)

There are 20 sections of the grid in the scrubber as stated in Chapter 1. Each section has around 93.3 elements of the grid. Fig.1.4 shows an element of the FlexiGrid #2. An element contains 8 blades and each blade has 20 segments. Schematic diagram of top view of an element for the grid is shown in Fig.AI.1.

The horizontal lines are the plates in an element and the vertical lines are the tie rods to support plates in an element:

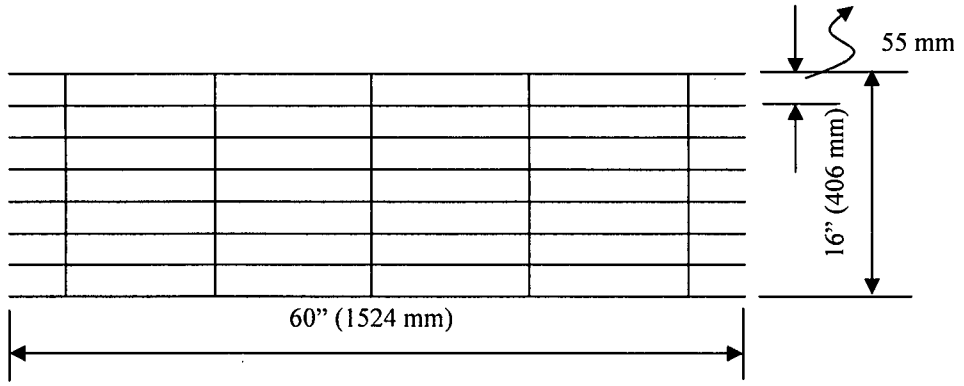

Figure AI.1 Schematic diagram of top view of an element

The voidage of the grid can be found by various ways. Firstly, the voidage can be found from the details of the grid given in the Table AI.1, the voidage of the packing can be estimated as,

$$voidage, \varepsilon = 1 - \frac{Weight\ of\ the\ packing\ /\ Volume\ of\ the\ packed\ bed}{Density\ of\ Grid\ packing\ material}$$

$$\varepsilon = 1 - \frac{263}{8000} = 0.967$$

The voidage of the packing estimated is 0.967.

Secondly, the voidage can be found from the BRF pressure drop model, for the grid. It is seen from the Fig.2.9 that the data points are scattered so we select a data point which has the least absolute error between the pressure drop calculated from the BRF pressure drop model and the pressure drop from Fig.2.5. Among all the data points, the data point for gas F-Factor of 3.79 and liquid loading of $12 m^3/m^2h$ has the least absolute difference of calculated and graphical pressure drop. Fig.AI.3 shows the percentage change of absolute difference of calculated pressure drop (from BRF model) with pressure drop from the graph, Fig.2.5, and voidage as independent variable. The graph shown in Fig.2.5 is for the air/water system and the properties of air/water are taken from Table 2.1. Keeping all the variables fixed in the BRF model and by changing the

variable, voidage, it is can be seen in Fig.AI.2 that the minimum of the curve occurs at voidage of 0.97.

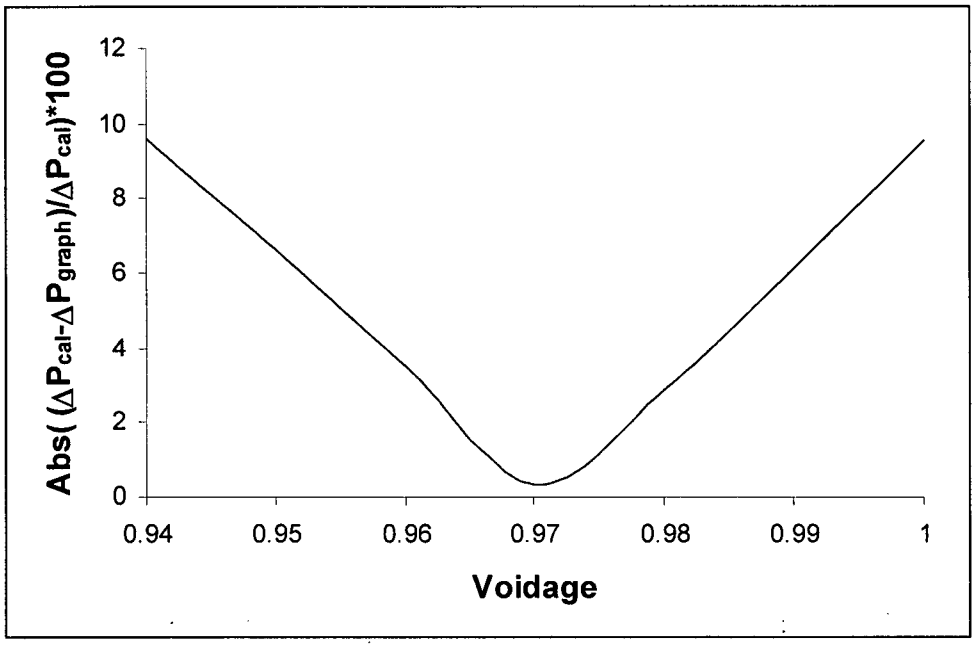

Figure AI.2 Finding voidage of FlexiGrid #2 from BRF model

Finally the voidage of the grid can also be calculated from the dimensions of the segment. The segments of the grid under clean and fouled conditions are shown in Fig.AI.3(a) and (b). Fig.AI.4 shows the dimension of the segment of the grid. When there is deposit of the fouling material on the surface of the packing, the voidage and the specific surface area of the fouled packing change. A method is shown how they can be calculated for a uniform thickness of fouling deposit on the grid packing. A segment of a blade was considered for calculation of change in voidage and specific surface area of the grid for both cleaned and fouled grid. Certain parts of the segment were identified which repeat in the same blade. They are identified in Fig.AI.5. Each of these parts was considered separately for calculation of metal volume of the grid, volume of the foulant collected on the surface of that part, and the specific surface area of cleaned and fouled surface of the grid. In each part, the foulant is shown as grey and the white portion as the metal. The foulant thickness of t mm is considered. For simplicity of the calculation the foulant is not shown on the top of each part, but they are included in the calculation. Initially, we calculate the volume of fouled material and surface area of the fouled parts A, B, C, D, E, F and G. And after that we calculate the total volume and surface area of

fouled material in a grid section. But, we see that at the junction of the certain parts say C - E and C – F the volume and surface area of overlapped foulant need to be removed to give the correct volume and surface area of the foulant in the grid section.

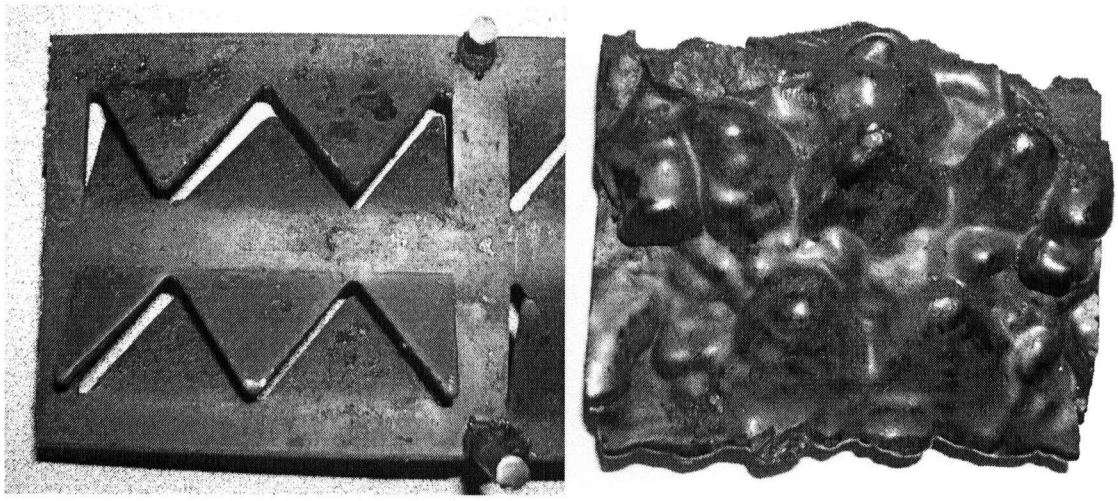

(a) (b)

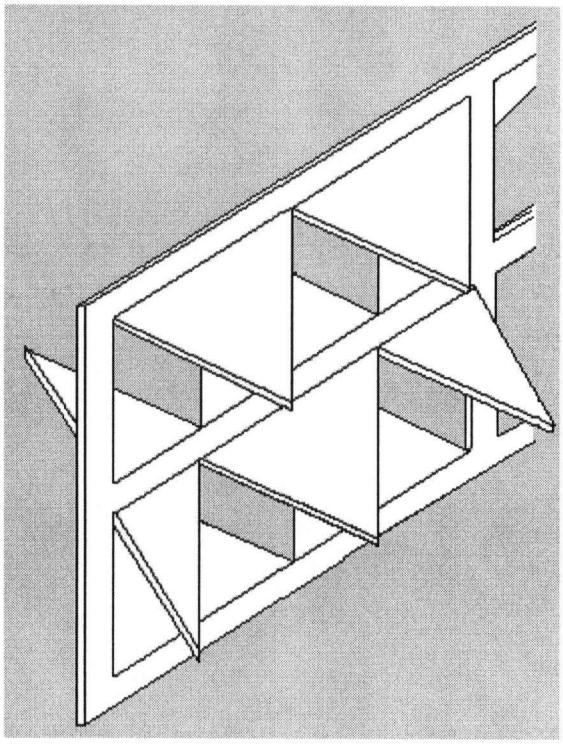

(c)

Figure AI.3 (a) Segment of the blade under clean condition, (b) segment of the blade with coke deposit and (c) Schematic diagram of 3-D View of a segment.

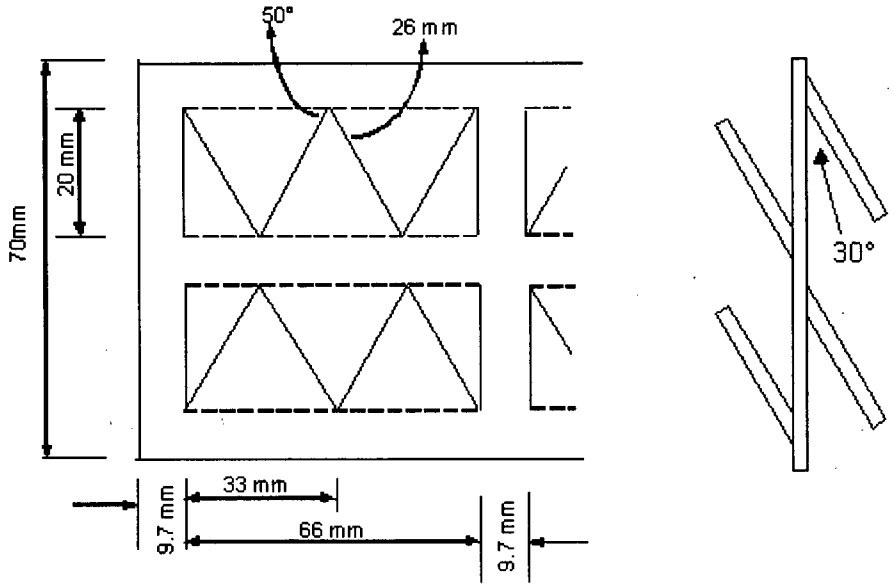

(a) Dimension of a segment (b) Side view of the segment

Figure AI.4 Schematic Diagram of a segment in a blade of an element of FlexiGrid #2

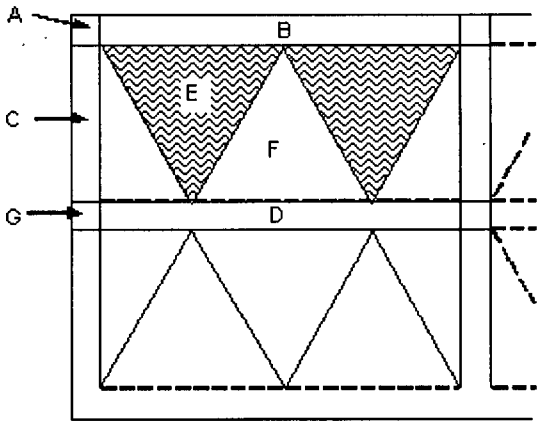

Figure AI.5 Parts identified on the segment were used for calculation of voidage and specific surface area of the grid

We follow this procedure and start with part A.

PART A

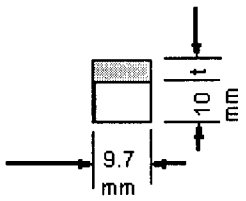

Volume of metal, $V_{MA} = 9.7 * 10 * 2 = 194\ mm^3$

Volume of fouled material , $V_{FA} = 9.7 * (10 + t) * (2 + 2 * t) - V_{MA}$

Surface area of the metal, $S_{MA} = 9.7 * 10 * 2 + 2 * 9.7 = 213.4\ mm^2$

Surface area of the fouled material on Part "A", $S_{FA} = 9.7 * (10 + t) * 2 + (2 + 2 * t) * 9.7$

Number of Part "A" in a blade = 42

Total volume of metal of Part "A" in a single blade, $V_{MAB} = 42 * V_{MA} = 8148\ mm^3$

Total volume of fouled material on Part "A" in a single blade, $V_{FAB} = 42 * V_{FA}$

Total metal surface area of Part "A" in a single blade, $S_{MAB} = 42 * S_{MA} = 8962.8\ mm^2$

Total fouled surface area of Part "A" in a single blade, $S_{FAB} = 42 * S_{FA}$

PART B

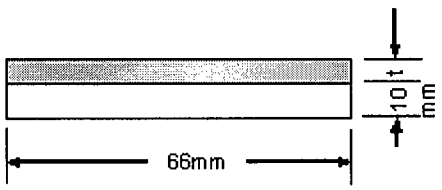

Volume of metal, $V_{MB} = 66 * 10 * 2 = 1320\ mm^3$

Volume of fouled material , $V_{FB} = (66) * (10 + t) * (2 + 2 * t) - V_{MB}$

Surface area of the metal, $S_{MB} = 66 * 10 * 2 + 2 * 66 = 1452\ mm^2$

Surface area of the fouled material on Part "B", $S_{FB} = 66 * (10 + t) * 2 + (2 + 2 * t) * 66$

Number of Part "B" in a blade = 40

Total volume of metal of Part "B" in a single blade, $V_{MBB} = 40 * V_{MB} = 52800\ mm^3$

Total volume of fouled material on Part "B" in a single blade, $V_{FBB} = 40 * V_{FB}$

Total metal surface area of Part "B" in a single blade, $S_{MBB} = 40 * S_{MB} = 58080\ mm^2$

Total fouled surface area of Part "B" in a single blade, $S_{FBB} = 40 * S_{FB}$

PART C

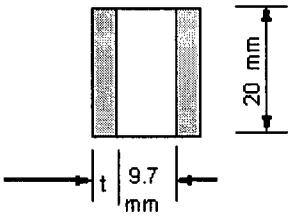

Volume of metal, $V_{MC} = 20 * 9.7 * 2 = 388\ mm^3$

Volume of fouled material , $V_{FC} = 20 * (9.7 + 2 * t) * (2 + 2 * t) - V_{MC}$

Surface area of the metal, $S_{MC} = 9.7 * 20 * 2 + 9.7 * 20 * 2 = 468\ mm^2$

Surface area of the fouled material on Part "C", $S_{FC} = (9.7 + 2 * t) * 20 * 2 + (2 + 2 * t) * 20 * 2$

Number of Part "C" in a blade = 42

Total volume of metal of Part "C" in a single blade, $V_{MCB} = 42 * V_{MC} = 16296\ mm^3$

Total volume of fouled material on Part "C" in a single blade, $V_{FCB} = 42 * V_{FC}$

Total metal surface area of Part "C" in a single blade, $S_{MCB} = 42 * S_{MC} = 19656\ mm^2$

Total fouled surface area of Part "C" in a single blade, $S_{FCB} = 42 * S_{FC}$

PART D

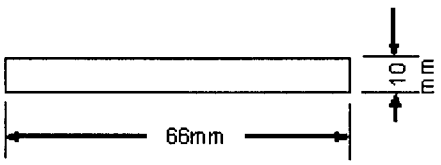

Volume of metal, $V_{MD} = 66 * 10 * 2 = 1320\ mm^3$

Volume of fouled material , $V_{FD} = 66 * (10 + t) * (2 + 2 * t) - V_{MD}$

Surface area of the metal, $S_{MD} = 66 * 10 * 2 = 1320\ mm^2$

Surface area of the fouled material on Part "D", $S_{FD} = 66 * 10 * 2$

Number of Part "D" in a blade = 20

Total volume of metal of Part "D" in a single blade, $V_{MDB} = 20 * V_{MD} = 26400\ mm^3$

Total volume of fouled material on Part "D" in a single blade, $V_{FDB} = 20 * V_{FD}$

Total metal surface area of Part "D" in a single blade, $S_{MDB} = 20 * S_{MD} = 26400\ mm^2$

Total fouled surface area of Part "D" in a single blade, $S_{FDB} = 20 * S_{FD}$

PART E

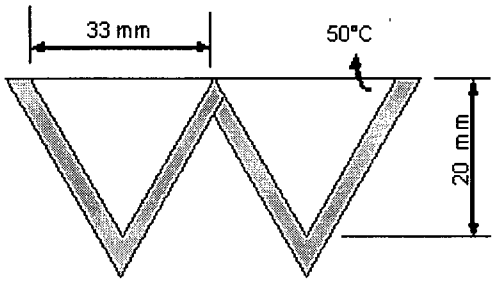

Volume of metal, $V_{ME} = 33 * 20 * 2 = 1320\ mm^3$

Volume of fouled material , $V_{FE} = (4 * 26 * t + 33 * 20 + 0.5 * t * (t / \tan(50°) + t * \tan(50°))) * (2 + 2 * t) - V_{ME}$

Surface area of the metal, $S_{ME} = 33 * 20 * 2 + 2 * 26 * 4 = 1528\ mm^2$

Surface area of the fouled material on Part "E", $S_{FE} = = (33 * 20 + 4 * 26 * t + t * 0.5 * (t / \tan(50°) + t * \tan(50°))) * 2 + (2 + 2 * t) * (26 * 4 + t / \tan(50°) + t * \tan(50°))$

Number of Part "E" in a blade = 40

Total volume of metal of Part "E" in a single blade, $V_{MEB} = 40 * V_{ME} = 52800\ mm^3$

Total volume of fouled material on Part "E" in a single blade, $V_{FEB} = 40 * V_{FE}$

Total metal surface area of Part "E" in a single blade, $S_{MEB} = 40 * S_{ME} = 61120\ mm^2$

Total fouled surface area of Part "E" in a single blade, $S_{FEB} = 40 * S_{FE}$

PART F

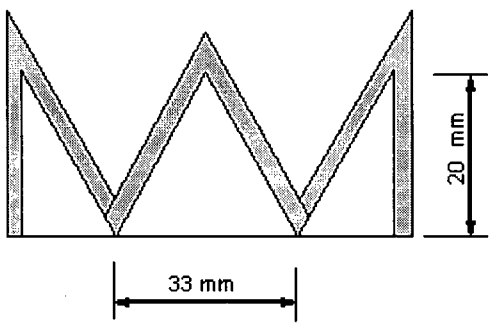

Volume of metal, $V_{MF} = 33 * 20 * 2 = 1320\ mm^3$

Volume of fouled material , $V_{FF} = (4 * 26 * t + 33 * 20 + 2 * 20 * t + 2 * t^2 / \cos(50°) + t^2 * \tan(50°)) * (2 + 2 * t) - V_{MF}$

Surface area of the metal, $S_{MF} = 33 * 20 * 2 + 2 * 20 * 2 + 2 * 26 * 4 = 1608\ mm^2$

Surface area of the fouled material on Part "F", $S_{FF} = 2 * (4 * 26 * t + 33 * 20 + 2 * 20 * t + 2 * t^2 / \cos(50°) + t^2 * \tan(50°)) + 2 * (20 + 2 * t / \cos(50°) + t * \tan(50°) + 26 * 2) * (2 + 2 * t)$

Number of Part "F" in a blade = 40

Total volume of metal of Part "F" in a single blade, $V_{MFB} = 40 * V_{MF} = 52800\ mm^3$

Total volume of fouled material on Part "F" in a single blade, $V_{FFB} = 40 * V_{FF}$

Total metal surface area of Part "F" in a single blade, $S_{MFB} = 40 * S_{MF} = 64320\ mm^2$

Total fouled surface area of Part "F" in a single blade, $S_{FFB} = 40 * S_{FF}$

PART G

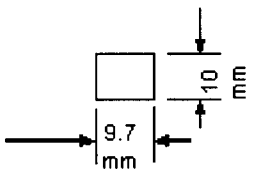

Volume of metal, $V_{MG} = 9.7 * 10 * 2 = 194\ mm^3$

Volume of fouled material , $V_{FG} = 9.7 * 10 * (2 + 2 * t) - V_{MG}$

Surface area of the metal, $S_{MG} = 9.7 * 10 * 2 = 194\ mm^2$

Surface area of the fouled material on Part "G", $S_{FG} = 9.7 * 10 * 2$

Number of Part "G" in a blade = 21

Total volume of metal of Part "G" in a single blade, $V_{MGB} = 21 * V_{MG} = 4074\ mm^3$

Total volume of fouled material on Part "G" in a single blade, $V_{FGB} = 21 * V_{FG}$

Total metal surface area of Part "G" in a single blade, $S_{MGB} = 21 * S_{MG} = 4074\ mm^2$

Total fouled surface area of Part "G" in a single blade, $S_{FGB} = 21 * S_{FG}$

Once the volume of the fouled substance is calculated for all parts, we also need to calculate the volume of the fouled material at the junction of C-E and C-F. At the junction of C-E we can see that the fouled material will overlap when we combine fouled part C and E together. So we need to remove this repeated volume of fouled material which is common to both parts C and E. It can be seen in the top view of part C-E junction, Fig.AI.6(a). In Fig.AI.6(b), shows the side view of junction C-E and it can be seen that the common part of junction C-E is not a triangle. So for the simplicity of calculation we assumed it to be triangle e'd'c'. This common part of junction C-E is part H. Fig.AI.6(c) gives the 3-D view of part H. The volume of fouled material part H is calculated as follows.

Volume of fouled material + metal for part H, V_{CEFM} = a'd' * d'c' * e'd' * (1/3)
Volume of metal in part H, V_{CEM} = area of Δx'd'y' (Fig.AI.6(a)) + area of Δa'x'z' (Fig.AI.6(a))
Volume of fouled material in part H, $V_{CEF} = V_{CEFM} - V_{CEM}$

The surface area needs to be deducted from fouled parts of C and E because of part H.
Surface area that needs to be deducted from fouled parts of C and E, S_{CEA}

= area of Δe'd'c' (Fig.AI.6(a,c)) + area of Δe'a'b' (Fig.AI.6(a,c))
= (1/2) * d'c' * e'd' + (1/2) * a'b' * e'a'

Similarly, the same type of calculation can be done for joined fouled parts of C – F. It can be seen in Fig. AI.7. The common part of junction C-F is part I. The volume of part I can be calculated as follows

Volume of fouled material + metal for part I, V_{CFFM} = (1/2) * e"d" * d"c" * d"a"
Volume of metal in part I, V_{CFM} = x"a" * a"f" (Fig.AI.7(a)) + d"x" * x"y" (Fig.AI.7(a))
Volume of fouled material in part I, $V_{CFF} = V_{CFFM} - V_{CFM}$

And the surface area needs to be deducted from the fouled parts of C and F because of part I.
Surface area that needs to be deducted from part C and F, S_{CFA}

= 2 * area of Δa"f"b" (Fig.AI.8(a,c))
= 2 * (1/2) * a"f" * a"b"

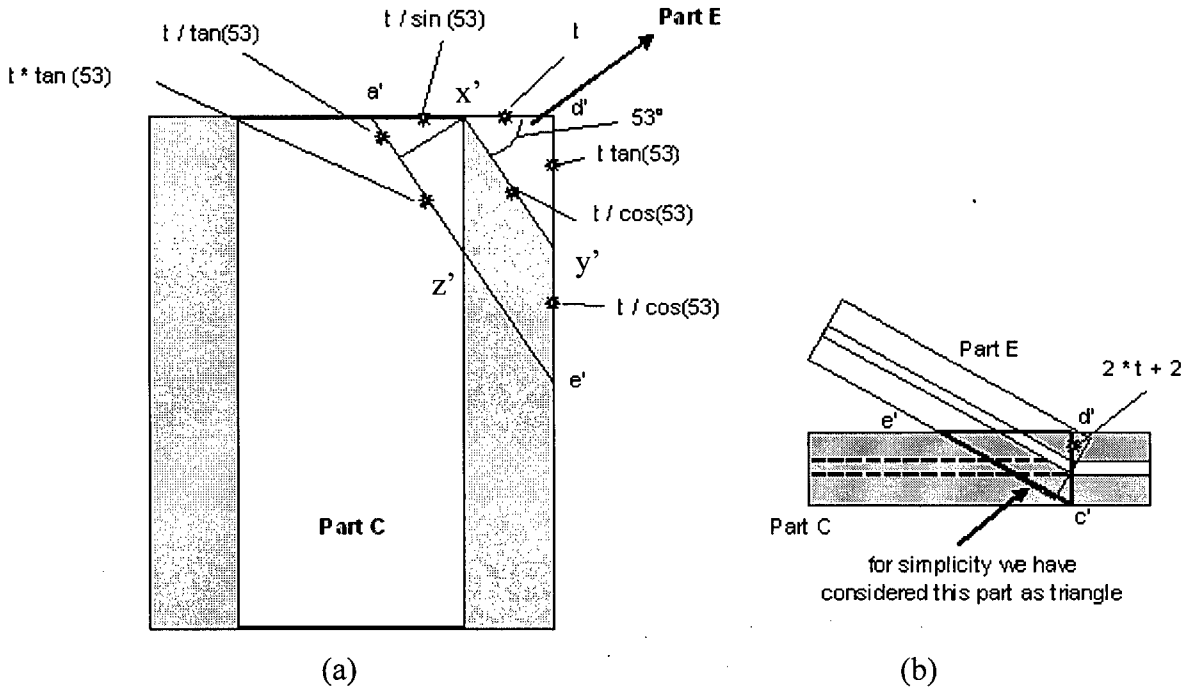

(a) (b)

(a) Top view of junction of fouled part of C – E. (b) Side view of junction of fouled parts of C-E

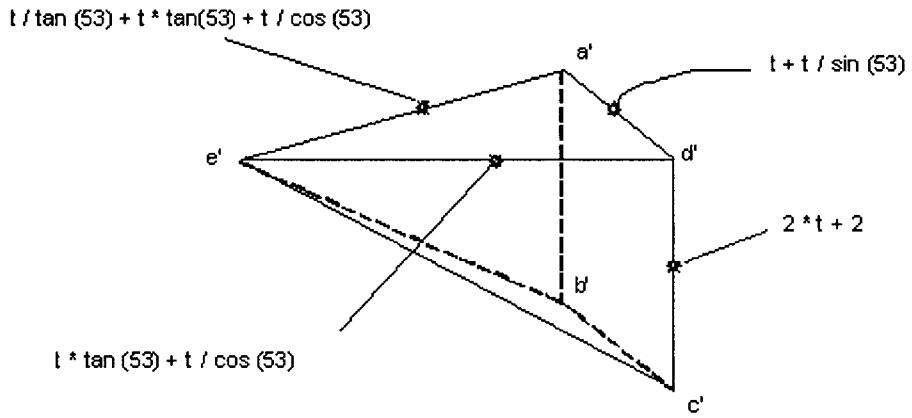

(c) 3-D view of the common fouled parts of C and E when they are joined, Part H.

Figure AI.6 The junction of fouled parts of C - E and part H.

In actual case both the parts E and F are joined to part C. It can be seen in Fig.AI.8. It can be seen that part E is shown as dotted, reason being that part E is protruded inward and part F is protruded outward. There is a possibility that both the parts E and F on part C will come closer when coke thickness increases on the packing surface. When the coke thickness is 4.2 mm the points a' and d" in Fig.AI.8(a) will merge. And when the coke thickness increases beyond 4.2

mm then it can be seen in Fig.AI.8(b). Calculation for change in volume and surface area caused by merging of fouled parts of C, E and F need to be calculated for foul thickness less than 4.2 mm and above 4.2 mm.

First we consider the thickness of fouled material below 4.2 mm.

Volume of fouled material, $V_{CEFF} = V_{CEF} + V_{CFF}$

Surface area that needs to be deducted from parts E, C and F, $S_{CEFA} = S_{CEA} + S_{CFA}$

For thickness of fouled material above 4.2 mm, there is again a common part given by c"a'b'd"vu. It can be seen in Fig. AI.8(c). The volume of this part is calculated as follows.

The dimension of the common part of parts C-E and C-F is shown in Fig.AI.6(c) and Fig.AI.7(c), respectively.

theta 1 = $\tan^{-1}$(e'd' / d'c')

theta 2 = $\tan^{-1}$(e'd' / d'a')

theta 3 = $\tan^{-1}$(a"f " / a"b")

c"a' = b"c" – (2 * 2 + 10 – a'd') ; wx = c"a'

wu = tan(theta 2) * wx ; c"w = wu / tan(theta 3)

Volume of part c"a'xwu in Fig.AI.8(c), V_{CEFFC1} = (1/3) * c"a' * c"w * wu

zv = wu ; yz = wx ; zd" = zv / tan (theta 1)

Volume of part zyb'd"v in Fig.AI.8(c), V_{CEFFC2} = (1/3) * zv * yz * zd"

xy = a"b" – c"w – zd"

Volume of part uwxyvz in Fig.AI.9(c), V_{CEFFC3} = (½) * uw * wx * xy

Total volume, $V_{CEFFC} = V_{CEFFC1} + V_{CEFFC2} + V_{CEFFC3}$

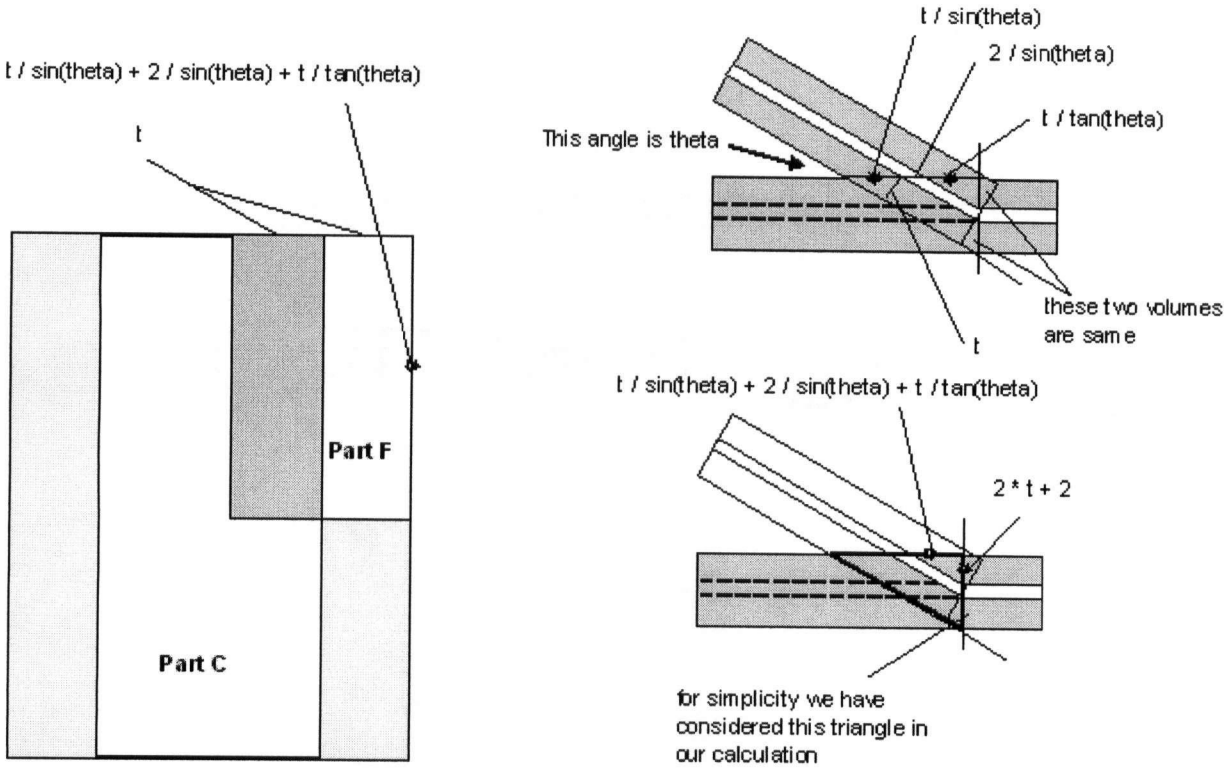

(a) (b)

(a) Top view of junction of part C – F. Part F is protruding outside the screen and can be seen in the side view diagram, (b) Side view of junction of part C-F

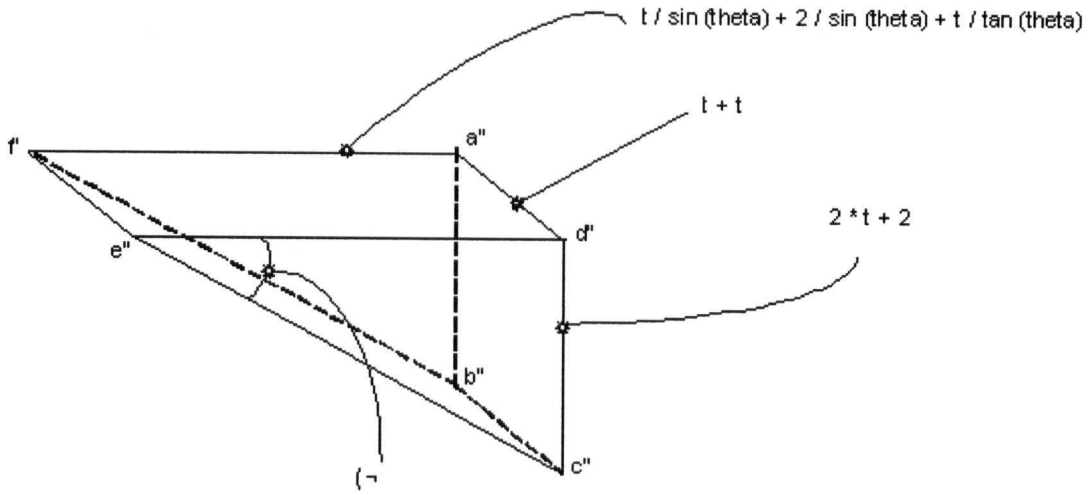

(c) 3-D view of the common part when fouled parts of C and F are joined.

Figure AI.7 The junction of fouled parts of C and F

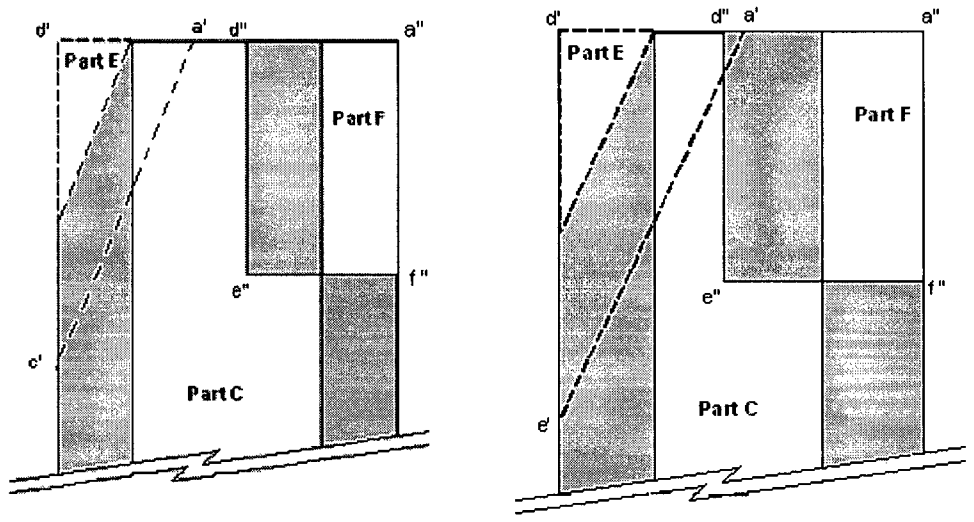

(a) (b)

Top view of the junction of parts E, C and F. Part E is protruding inward and is shown in dotted line and part F is protruding outside. (a) For thickness of fouled material < 4.2 mm and (b) for thickness above 4.2 mm.

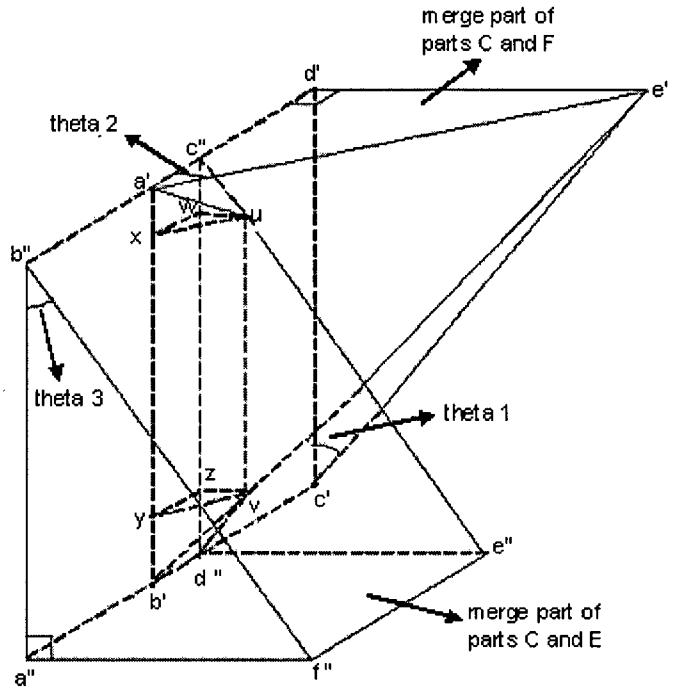

(c) 3-D view of common part when fouled parts of E, C and F are joined.

Figure AI.8 The junction of fouled parts of E, C and F

Volume of fouled material above 4.2 mm, $V_{CEFF} = V_{CEF} + V_{CFF} - V_{CEFFC}$

Surface area also needs to removed when two common parts of C-E and C-F merge. This will only happen when the fouled material thickness is more than 4.2 mm.

Surface area that needs to be deducted from parts E, C and F when the fouled thickness is above 4.2 mm, $S_{CEFA} = S_{CEA} + S_{CFA} - S_{CEFAC}$

S_{CEFAC}, is the surface area that needs to be removed when the two common parts of C-E and C-F merge. It can be calculated as follows.

S_{CEFAC} = area of Δ a'ux + area of uxyv + area of Δ vyb' + area of Δ c"uw + area of uwzv + area of Δ vzd"

= (½) * a'x * wu / sin(theta 2) + wu * sin(theta 2) * xy + (½) * zd" * wu / sin (theta 2) + (½) * c"w * wu + wu * xy + (1/2) * zd" * wu

Finally, volume of these common parts of C-E and C-F in a blade,

$V_{CEFFB} = 2 * 21 * V_{CEFF}$

And, surface area of these common parts of C-E and C-F that needs to be removed in a blade,

$S_{CEFAB} = 2 * 21 * S_{CEFA}$

Now, metal volume of single blade, V_{TMB}

$= V_{MAB} + V_{MBB} + V_{MCB} + V_{MDB} + V_{MEB} + V_{MFB} + V_{MGB}$

$= 213{,}318\ mm^3$

Metal volume of single element, V_{TME}

$= 8 * V_{TMB}$

$= 1{,}706{,}544\ mm^3$

Fouled material volume on single blade, V_{TFB}

$= V_{FAB} + V_{FBB} + V_{FCB} + V_{FDB} + V_{FEB} + V_{FFB} + V_{FGB} - V_{CEFFB}$

Fouled material volume on single element, V_{TFE}

$= 8 * V_{TFB}$

Surface area of single blade, S_{TMB}

$= S_{MAB} + S_{MBB} + S_{MCB} + S_{MDB} + S_{MEB} + S_{MFB} + S_{MGB}$

$= 242{,}612.8 \text{ mm}^2$

Surface area of single element, S_{TME}

$= 8 * S_{TMB}$

$= 1{,}940{,}902 \text{ mm}^2$

Surface area of fouled material on single blade, S_{TFB}

$= S_{FAB} + S_{FBB} + S_{FCB} + S_{FDB} + S_{FEB} + S_{FFB} + S_{FGB} - S_{CEFAB}$

Surface area of fouled material on single element, S_{TFE}

$= 8 * S_{TFB}$

Volume of an element including void space, V_{EV}

$= 1524 * 406 * 70$

$= 43{,}312{,}080 \text{ mm}^3$

Specific surface area of packing under cleaned condition, a_{pc}

$= S_{TME} / V_{EV}$

$= 0.04481 \text{ mm}^2/\text{mm}^3$

$= 44.81 \text{ m}^2/\text{m}^3$

Specific surface area of packing under fouled condition, a_{pf}

$= S_{TFE} / V_{EV}$ in mm^2/mm^3

It can be seen that the specific surface area of the grid calculated was 44.81 m^2/m^3, which is very close to 45 m^2/m^3 given in Table AI.1. The error of 0.4% is acceptable based on the dimension of the grid segments. We can use the above procedure for calculation of change in specific surface area of the grid due to foulant deposit on the surface of the packing. Now we need to calculate

the voidage of a single layer of the grid packing under clean condition and also for fouled condition and the steps are shown below.

The cross sectional area of the packed bed scrubber, A_T

$= 3.141 * 9.144^2 / 4$

$= 65.66\ m^2$

The area occupied by an element, refer Fig. AI.2, A_E

$= 1524 * (406 + 56) * 10^{-6}$

$= 0.7041\ m^2$

Number of elements in a single layer,

$= 65.66 / 0.7041$

$= 93.3$

Volume of metal in a single layer, V_{TML}

$= 93.3 * V_{TME}$

$= 119,517,300\ mm^3$

Volume of fouled material on the packing surface in a single layer, V_{TFL}

$= 93.3 * V_{TFE}$

Volume of single layer of element with void space, V_{LV}

$= 93.3 * V_{EV}$

$= 4,041,017,064\ mm^3$

Voidage of the packing under cleaned condition in a single layer, ε_0

$= 1 - V_{TML} / V_{LV}$

$= 0.97$

Voidage of the packing under fouled condition in a single layer, ε_f

$= 1 - (V_{TML} + V_{TFL}) / V_{LV}$

The voidage of the grid is calculated as 0.97 based on the dimensions of the grid segment. So we consider the voidage as 0.97 in our study. Based on the above procedure the change in specific surface area and voidage of packing due to fouling deposit on the surface of the packing is calculated. They can be seen in Fig.3.6 and 3.7.

Appendix II: ASTM D2887 distillation curve for HGO wash and shed vapour

Table AII.1 ASTM D2887 distillation curve for HGO wash (Syncrude Canada Ltd.)

wt%	NBP [C]	wt%	NBP [C]	wt%	NBP [C]
0	263.5	34	395	68	464.5
1	275	35	397	69	467
2	289.5	36	399.5	70	469
3	298.5	37	401.5	71	471.5
4	305.5	38	403.5	72	473.5
5	310.5	39	405.5	73	476
6	315.5	40	408	74	478.5
7	320	41	410	75	481
8	324.5	42	412	76	483.5
9	328.5	43	414	77	486
10	332	44	416	78	488.5
11	336	45	418	79	491.5
12	339.5	46	419.5	80	494.5
13	342.5	47	421.5	81	497
14	345.5	48	423.5	82	500
15	348.5	49	425.5	83	503
16	351.5	50	427.5	84	506
17	354	51	429.5	85	509.5
18	357	52	431	86	513
19	359.9	53	433	87	517
20	362	54	435	88	520.5
21	364.5	55	437	89	525
22	367	56	439	90	529.5
23	369.5	57	441	91	535
24	372	58	443	92	540.5
25	374.5	59	445	93	547
26	377	60	447	94	555
27	379	61	449	95	564.5
28	381.5	62	451	96	576
29	384	63	453.5	97	591.5
30	386	64	455.5	98	615.5
31	388.5	65	457.5	99	680.5
32	390.5	66	460	100	750
33	393	67	462		

Table AII.2 ASTM D2887 distillation curve for shed vapour (Jankovic, 2005)

wt %	NBP [C]
0	-190.952
1	-170.216
2	-150.412
3.5	-122.967
5	-98.941
7.5	-73.1315
10	-53.7434
12.5	-26.9077
15	-7.20E-02
17.5	127.182
20	274.0067
25	310.1956
30	346.3846
35	378.1825
40	408.3113
45	438.1868
50	467.337
55	468.4255
60	469.4258
65	470.338
70	471.162
75	485.3802
80	501.6444
85	518.8119
90	540.3106
92.5	554.3681
95	568.4256
96.5	599.3716
98	630.3175
99	680.9176
100	752.7427

Appendix III: Wehie series – a phase separation kinetic model for coke formation

As discussed in Chapter 2, the coke formation during thermolysis of pitch involves the liquid – liquid phase separation of reacted asphaltenes from heptane solubles. The coking of asphaltenes and whole pitch in the open reactor using the **series** model of Wiehe, as given by Eq.(2.47) – (2.51).

Heptane solubles and asphaltene undergo reactions Eq.(2.47) and Eq.(2.48). All the reactions are first order reaction. Let initial heptane soluble concentration in wt% be H_o and the initial asphaltene wt% be A_o in the pitch. From initial heptane solubles concentration wt %, H_o, in the pitch, the reactant asphaltene, A^+, is produced by the series reactions of Eq.(2.47) and Eq.(2.48). From Eq.(2.47), heptane solubles produces reactant asphaltenes A^+ and volatiles, V, and from the Eq.(2.48), reactant asphaltene produces asphaltene cores, A^*, non-volatile heptane soluble, H^*, and volatiles, V.

From Eq.(2.47) the rate equations for H^+, A^+ and V can be written as

$$\frac{dH^+}{dt} = -k_H\ H^+ \qquad \text{(AIII.1)}$$

$$\frac{1}{b}\frac{dA^+}{dt} = k_H\ H^+ \qquad \text{(AIII.2)}$$

$$\frac{1}{(1-b)}\frac{dV}{dt} = k_H\ H^+ \qquad \text{(AIII.3)}$$

from Eq.(2.48) the rate equations for A^+, A^*, H^* and V can be written as

$$\frac{dA^+}{dt} = -k_A\ A^+ \qquad \text{(AIII.4)}$$

$$\frac{1}{a}\frac{dA^*}{dt} = k_A\ A^+ \qquad \text{(AIII.5)}$$

$$\frac{1}{d}\frac{dH^*}{dt} = k_A\, A^+ \qquad \text{(AIII.6)}$$

$$\frac{1}{(1-a-d)}\frac{dV}{dt} = k_A\, A^+ \qquad \text{(AIII.7)}$$

The net rate of A^+, V, A^* and H^* from the above equations will be,

$$\frac{dA^+}{dt} = b\,k_H\, H^+ - k_A\, A^+ \qquad \text{(AIII.8)}$$

$$\frac{dV}{dt} = (1-b)k_H\, H^+ + (1-a-d)\,k_A\, A^+ \qquad \text{(AIII.9)}$$

$$\frac{dA^*}{dt} = a\,k_A\, A^+ \qquad \text{(AIII.10)}$$

$$\frac{dH^*}{dt} = d\,k_A\, A^+ \qquad \text{(AIII.11)}$$

From Eq.(AIII.1), heptane solubles yield with respect to time can be found out as follows :

$$\frac{dH^+}{dt} = -\,k_H\, H^+ \qquad \text{(AIII.12)}$$

Integrating with boundary conditions at t = 0, $H^+ = H_o$ we have

$$H^+ = H_o\, e^{-k_H t} \qquad \text{(AIII.13)}$$

From Eq.(AIII.8), asphaltenes yield with respect to time can be found out as follows :

$$\frac{dA^+}{dt} = b\,k_H\, H^+ - k_A\, A^+ \qquad \text{(AIII.14)}$$

$$\Rightarrow \quad \frac{dA^+}{dt} + k_A\, A^+ = b\,k_H\, H^+ \qquad \text{(AIII.15)}$$

$$\Rightarrow \quad \frac{dA^+}{dt} + k_A\, A^+ = b\,k_H\, H_o\, e^{-k_H t} \qquad \text{(AIII.16)}$$

multiplying both sides by integrating factor, $e^{k_A t}$

$$\Rightarrow \quad \frac{d(A^+ e^{k_A t})}{dt} = b\,k_H\,H_o\,e^{-k_H t}\,e^{k_A t} = b\,k_H\,H_o\,e^{(k_A - k_H)t} \qquad \text{(AIII.17)}$$

Integrating with boundary conditions at t = 0, $A^+ = 0$, we have

A^+ can be written as

$$A^+ = \frac{b\,k_H\,H_o}{(k_A - k_H)}\left[e^{-k_H t} - e^{-k_A t}\right] \qquad \text{(AIII.18)}$$

From Eq.(AIII.11), Volatiles yield with respect to time can be found out as shown:

$$\frac{dV}{dt} = (1-b)k_H\,H^+ + (1-a-d)\,k_A\,A^+ \qquad \text{(AIII.19)}$$

Putting H^+ and A^+ Eq.(AIII.14) and Eq.(AIII.18) into Eq.(AIII.19), we have

$$\frac{dV}{dt} = (1-b)k_H\,H_o\,e^{-k_H t} + (1-a-d)\,k_A\,\frac{b\,k_H\,H_o}{(k_A - k_H)}\left[e^{-k_H t} - e^{-k_A t}\right] \qquad \text{(AIII.20)}$$

Integrating with boundary conditions at t = 0, V = 0, we have

Volatile yield as

$$V = (1-b)H_o\left(1 - e^{-k_H t}\right) + \frac{(1-a-d)\,k_A b\,k_H\,H_o}{(k_A - k_H)}\left[\frac{1-e^{-k_H t}}{k_H} - \frac{1-e^{-k_A t}}{k_A}\right] \qquad \text{(AIII.21)}$$

From Eq.(AIII.5) for asphaltene cores yield with respect to time can be found out as follows:

$$\frac{dA^*}{dt} = a\,k_A\,A^+ \qquad \text{(AIII.22)}$$

Putting A^+ from Eq.(AIII.18) into Eq.(AIII.22) we get

$$\frac{dA^*}{dt} = a\,k_A\,\frac{b\,k_H\,H_o}{(k_A - k_H)}\left[e^{-k_H t} - e^{-k_A t}\right] \qquad \text{(AIII.23)}$$

Integrating with boundary condition at t = 0 , A* = 0

The final form of A^* as

$$A^* = \frac{a\,k_A b\,k_H\,H_o}{(k_A - k_H)}\left[\frac{1-e^{-k_H t}}{k_H} - \frac{1-e^{-k_A t}}{k_A}\right] \qquad \text{(AIII.24)}$$

Similarly, from Eq.(AIII.6) for heptane solubles yield with respect to time, can be found out as follows:

$$H^* = \frac{d\,k_A b\,k_H\,H_o}{(k_A - k_H)}\left[\frac{1-e^{-k_H t}}{k_H} - \frac{1-e^{-k_A t}}{k_A}\right] \qquad \text{(AIII.25)}$$

The remaining part of the initial asphaltene concentration in wt%, A_o, present in the pitch will undergo thermal conversion to form asphaltene core , heptane solubles and volatile, that can be seen in Eq.(2.55). From Eqs.(AIII.4), (AIII.5), (AIII.6) and (AIII.7) asphlatene, asphaltene core, volatiles and heptane solubles yield can be found out as :

$$A^+ = A_0\,e^{-k_A t} \qquad \text{(AIII.26)}$$

$$V = (1-a-d)\,A_0\,(1-e^{-k_A t}) \qquad \text{(AIII.27)}$$

$$A^* = a\,A_0\,(1-e^{-k_A t}) \qquad \text{(AIII.28)}$$

$$H^* = d\,A_0\,(1-e^{-k_H t}) \qquad \text{(AIII.29)}$$

The net equation for kinetic model for respective yield can be written as :

$$H^+ = H_o\,e^{-k_H t} \qquad \text{(AIII.30)}$$

$$A^+ = \frac{b\,k_H\,H_o}{(k_A - k_H)}\left[e^{-k_H t} - e^{-k_A t}\right] + A_0\,e^{-k_A t} \qquad \text{(AIII.31)}$$

$$V = (1-b)H_o\left(1-e^{-k_H t}\right) + \frac{(1-a-d)\,k_A b k_H H_o}{(k_A - k_H)}\left[\frac{1-e^{-k_H t}}{k_H} - \frac{1-e^{-k_A t}}{k_A}\right] + (1-a-d)\,A_0\,(1-e^{-k_A t}) \quad \text{(AIII.32)}$$

During coke induction period:

$$A^* = \frac{a\,k_A b k_H H_o}{(k_A - k_H)}\left[\frac{1-e^{-k_H t}}{k_H} - \frac{1-e^{-k_A t}}{k_A}\right] + a\,A_0\,(1-e^{-k_A t}) \quad \text{(AIII.33)}$$

$$H^* = \frac{d\,k_A b k_H H_o}{(k_A - k_H)}\left[\frac{1-e^{-k_H t}}{k_H} - \frac{1-e^{-k_A t}}{k_A}\right] + d\,A_0\,(1-e^{-k_A t}) \quad \text{(AIII.34)}$$

and

$$TI = 0$$

The coke induction period ends when

$$A^*_{\max} = S^0_L\left(H^+ + H^*\right) \quad \text{(AIII.35)}$$

and from the above expressions we have

$$TI = A^*_{ex} = A^* - A^*_{\max} \quad \text{(AIII.36)}$$

$$TI = A^* - S^0_L\left(H^+ + H^*\right) \quad \text{(AIII.37)}$$

For 1st order reaction, k_A and k_H can be calculated for different temperatures by the following expression:

$$\ln\frac{k_A}{k_{A,390C}} = \frac{-E_A}{R}\left[\frac{1}{T} - \frac{1}{(390+273.15)}\right] \quad \text{(AIII.38)}$$

and

$$\ln\frac{k_H}{k_{H,390C}} = \frac{-E_H}{R}\left[\frac{1}{T} - \frac{1}{(390+273.15)}\right] \quad \text{(AIII.39)}$$